ESD-TR-72-187

Semiannual Technical Summary

Seismic Discrimination

30 June 1972

Prepared for the Advanced Research Projects Agency
under Electronic Systems Division Contract F19628-70-C-0230 by

Lincoln Laboratory

MASSACHUSETTS INSTITUTE OF TECHNOLOGY

Lexington, Massachusetts

DISCLAIMER NOTICE

THIS DOCUMENT IS THE BEST QUALITY AVAILABLE.

COPY FURNISHED CONTAINED A SIGNIFICANT NUMBER OF PAGES WHICH DO NOT REPRODUCE LEGIBLY.

DOCUMENT CONTROL DATA – R&D

(Security classification of title, body of abstract and indexing annotation must be entered when the overall report is classified)

1. ORIGINATING ACTIVITY *(Corporate author)*
Lincoln Laboratory, M.I.T.

2a. REPORT SECURITY CLASSIFICATION
Unclassified

2b. GROUP
None

3. REPORT TITLE
Seismic Discrimination

4. DESCRIPTIVE NOTES *(Type of report and inclusive dates)*
Semiannual Technical Summary Report – 1 January through 30 June 1972

5. AUTHOR(S) *(Last name, first name, initial)*
Davies, David

6. REPORT DATE
30 June 1972

7a. TOTAL NO. OF PAGES
96

7b. NO. OF REFS
53

8a. CONTRACT OR GRANT NO. F19628-70-C-0230

b. PROJECT NO. ARPA Order 512

c.

d.

9a. ORIGINATOR'S REPORT NUMBER(S)
Semiannual Technical Summary, 30 June 1972

9b. OTHER REPORT NO(S) *(Any other numbers that may be assigned this report)*
ESD-TR-72-187

10. AVAILABILITY/LIMITATION NOTICES
Approved for public release; distribution unlimited.

11. SUPPLEMENTARY NOTES
None

12. SPONSORING MILITARY ACTIVITY
Advanced Research Projects Agency, Department of Defense

13. ABSTRACT

New results are presented on seismic source parameter determination, and lists of events useful to discrimination studies are presented. Travel times and location anomalies are reconsidered in the light of heterogeneity in the deep mantle. New approaches to structure determination beneath LASA are described. NORSAR short-period data are discussed extensively. Properties of signals and noise at LASA, NORSAR and ALPA are given. Network approaches to improved detection capability on a global basis are outlined.

14. KEY WORDS
seismic array
seismometers
seismology

MASSACHUSETTS INSTITUTE OF TECHNOLOGY

LINCOLN LABORATORY

SEISMIC DISCRIMINATION

SEMIANNUAL TECHNICAL SUMMARY REPORT
TO THE
ADVANCED RESEARCH PROJECTS AGENCY

1 JANUARY – 30 JUNE 1972

ISSUED 15 AUGUST 1972

LEXINGTON MASSACHUSETTS

The work reported in this document was performed at Lincoln Laboratory, a center for research operated by Massachusetts Institute of Technology. This research is a part of Project Vela Uniform, which is sponsored by the Advanced Research Projects Agency of the Department of Defense under Air Force Contract F19628-70-C-0230 (ARPA Order 512).

ABSTRACT

New results are presented on seismic source parameter determination, and lists of events useful to discrimination studies are presented. Travel times and location anomalies are reconsidered in the light of heterogeneity in the deep mantle. New approaches to structure determination beneath LASA are described. NORSAR short-period data are discussed extensively. Properties of signals and noise at LASA, NORSAR and ALPA are given. Network approaches to improved detection capability on a global basis are outlined.

Accepted for the Air Force
Nicholas A. Orsini, Lt. Col., USAF
Chief, Lincoln Laboratory Project Office

CONTENTS

SUMMARY

This is the seventeenth Semiannual Technical Summary of the Seismic Discrimination Group of Lincoln Laboratory. It describes research associated with the theory and practice of detection, location and identification of earthquakes and underground explosions. Particular emphasis is placed on the role that digital data processing and large array techniques play in such work.

A study has been made of some unusual events in Asia which fail, or almost fail, the M_s:m_b discriminant. These constitute a small but not negligible proportion of events in that region. One event has caused particular difficulty, with an apparent depth phase but every other aspect of an explosion. A catalogue of presumed explosions in the Soviet Union away from the regular test sites is presented. A time domain analysis of seismograms from a large Siberian earthquake has been made. This event has special interest, being in a region of only mild seismicity. Certain features in the deconvolved record suggest that rupture dimensions and velocity can be extracted from the suite of records. The question of the cause of discrimination is reopened with a discussion of conclusions that can be drawn from earthquakes of apparently very small dimensions which discriminate with ease. We conclude that the partition of energy between P-waves and Rayleigh waves may be the central cause. A study has been completed of R_g phases from cratering and fully contained explosions in Nevada. We found that explosions that break surface are richer in R_g than fully contained events.

Extensive work has been done at Lincoln on the multipathing of Rayleigh waves, and now a ray-tracing program has been used on a globe with continent/ocean distinctions. The results show striking agreement with observation, and open up the possibility that we can more adequately predict expected surface wave magnitudes from hypothetical sources on a real earth. Travel-time studies up to the present have had to make assumptions about near source heterogeneities which may not be valid. We have therefore conducted a P-wave travel-time study which uses only deep-focus earthquakes. A rather surprising result emerges. Rays which have penetrated the deepest mantle show very systematic deviations from standard travel-time tables of up to ±1 sec. This result is of interest in characterizing regions of the deep mantle and also in attempts to predict the value of seismic observatories at distances beyond 90°. A cognate result has been found from recent array studies of $dT/d\Delta$ and azimuth anomalies. It appears inevitable that there are large- and small-scale lateral variations of significant amplitude throughout the whole mantle, but particularly near the core-mantle boundary.

Work continues on describing the structure beneath LASA, both in terms of a Chernov-type approach in which the amplitude and phase fluctuations observed at individual seismometers are related by a model in which the earth beneath LASA is a randomly varying medium with small variations in refractive index, and also by an analysis of S-waves generated near the surface by interfaces such as the sediment/basement boundary. A routine technique is proposed for quality control of LASA, or any other digital seismic data, by use of pseudo-random input to the calibration coil and spectral analysis of the resulting output tape.

The increasing availability of NORSAR data and the interchange of scientists with the NORSAR data center lead to an increasing amount of research into NORSAR capabilities. Studies of NORSAR signal amplitudes have concentrated on the degree of coherence in short-period data across the array, and contrasts are made with amplitude scatter at LASA. We find that NORSAR body wave

magnitudes of seismic events are generally lower than global averages. A possible reason for this in terms of near-surface high-impedance values is proposed. The false-alarm rate in the NORSAR detection processor is analyzed and some unexpected features in it are considered in terms of spectral characteristics of signals. Noise spectra for LASA and NORSAR short-period data are contrasted and it is asserted that no effort should be made to filter out the NORSAR high-frequency signal in favor of 1-Hz energy.

A detailed study has been completed of long-period nonpropagating noise. This largely has its origin in microbarographic fluctuations. The theory of the effect of these fluctuations on the surface of the earth has needed some care, as previous models have tended to ignore terms in integrals which do not converge. The collocation of ALPA and a long-period seismometer of Pomeroy type at Fairbanks, Alaska has allowed us to start an evaluation of the relative merits of instruments recording in somewhat different frequency bands. A population of overlapping time intervals is being examined.

Results of the pilot study on short-period network capability are presented, and the importance of using LASA's detection log in conjunction with some carefully selected WWSSN stations is emphasized. Early prospects are considered from the International Seismic Month for which Lincoln Laboratory has acted as host. This project has involved the collaboration of several groups around the world with access to large quantities of seismic data. A bulletin based on short-period P-wave readings for a 1-month period in early 1972 will be issued soon and, in the second phase, surface waves will be analyzed. We then hope to reach useful conclusions on the contributions that can be made by individual stations to a seismic monitoring network.

D. Davies

GLOSSARY

ALPA	Alaskan Long-Period Array
CGS	United States Coast and Geodetic Survey
LASA	Large Aperture Seismic Array
NOAA	National Oceanographic and Atmospheric Administration
NORSAR	Norwegian Seismic Array
NOS	National Ocean Survey
PDE	Preliminary Determination of Epicenters
SAAC	Seismic Array Analysis Center
SATS	Semiannual Technical Summary
WWSSN	World-Wide Standard Seismographic Network

SEISMIC DISCRIMINATION

I. THE SEISMIC SOURCE

A. SOME INTERESTING CENTRAL ASIAN EVENTS ON THE M_s:m_b DIAGRAM

Seismic discrimination between earthquakes and explosions is complicated by the observation of occasional events with conflicting discrimination parameters. In particular, the most widely used discriminant, the M_s:m_b diagram, classifies a small number of earthquakes as explosions (for example, possibly a few of the earthquakes occurring in the Lagunа Salada and Nevada-Arizona regions of the United States,[1] and certainly two of the events studied here). Further complications arise when the surface waves from an explosion are masked by the surface waves of a large earthquake, or when the body waves of an explosion are perturbed to resemble short-period earthquake radiation through the detonation of several explosions over a short time span. Here, the existence of some Tibetan and southern Russian events that have anomalously low surface-wave-to-body-wave magnitude ratios are documented. Further, one of the southern Russian events (event KA in Table I-1) is used to illustrate the problems that arise when an interfering event is present and when multiple detonations are considered possible. Marshall and Basham[2] have previously determined the general behavior of M_s:m_b for Central Asia, and their relationship is used for purposes of comparison.

TABLE I-1
EVENTS USED IN THIS STUDY (CGS LOCATIONS)

Event Symbol	Day	Origin Time (GMT)	Latitude (°N)	Longitude (°E)	Depth	m_b	M_s*
KA	5-1-69	04:00:08.7	44.0	77.9	53	4.9	2.4
KB	12-9-69	13:41:09.0	40.1	70.7	N	4.9	3.6
KC	7-1-68	19:14:54.7	44.0	79.3	N	4.8	3.6
KD	7-20-69	04:34:14.9	39.8	77.8	N	4.9	4.2
TA	7-15-68	05:09:05.9	30.3	95.0	22	4.8	2.9
TB	7-14-68	18:12:40.9	30.3	94.8	22	4.9	3.3
TC	7-13-68	05:05:54.2	30.3	94.6	N	5.0	3.4

* Each M_s value is based on the results from at least four individual stations.

The location of the stations and events used in this study are plotted on a map of Eurasia in Fig. I-1. These data are a subset of data being used in a network study of Central Asian seismicity (SATS, 31 December 1971, DDC AD-737092); station data are given in that report. The four events starting with a K are located in the southeastern corner of Kazakh, USSR. They

locate within 10° of each other. The other three events discussed are closely grouped in an area of Tibet about 300 km northeast of the capital, Lhasa. They are prefixed by the letter T. All 7 events have approximately the same body wave magnitude, 4.9 ± 0.1, and are listed as shallow focus earthquakes in the NOS bulletin (that is, they are assigned focal depths between 20 and 70 km in the PDE catalog). Epicentral data determined by NOS are given in Table I-1. The Kazakh events lie on the border of aseismic Central Asia. Plowshare-type explosions have been detonated in this area (see event dated 10-21-66 in Table I-3). The Soviet test site at Semipalatinsk is about 6° to the north. The Tibetan events are part of an isolated cluster of seismic activity.

M_s values were calculated using the scale proposed by Marshall and Basham[2]:

$$M_s = \log_{10}(A) + P(T) + B'(\Delta)$$

where A is the maximum amplitude of the vertical component of the Rayleigh wave at the period T measured at an epicentral distance Δ. P(T) corrects for dispersion; and B'(Δ) corrects for the average effects of scattering, geometrical spreading, lateral refraction and anelastic attenuation of Rayleigh waves. The M_s values for the 7 events are included in Table I-1, and range from 2.4 up to 4.2. Thus, even though m_b varies by only 0.2, M_s varies by 1.8. Based on the regional seismicity of Kirghiz for events with $m_b = 4.9$ (see Ref. 3), the 4 events in that region would represent approximately 10 percent of the total population that would be observed over a comparable period of time. Figure I-2 shows how the events plot on an M_s:m_b diagram. The two lines drawn on the graph denote the trends of earthquake and explosion population for Central Asia.[2] Data used to calculate the trend lines were obtained from the same stations and analyzed in the same manner as the data used here. None of the earthquakes used in that study with an $m_b = 4.9$ scattered to the left of the event KB. Furthermore, the inclusion of our events would not cause the trend lines to be appreciably altered. The events located in Kazakh (denoted by KB and KC), along with the Tibetan events (TB and TC), could not be classified as either artificial or natural on the basis of M_s:m_b alone. The events KA and TA clearly fall into the explosion population. The three Tibetan events are presumably earthquakes. They occur in an unlikely geographic location for explosions, and have the short-period complexity and Lg:P energy ratios characteristic of earthquakes. Moreover, many similar events have occurred historically within a degree or so of their epicenters. The Kazakh events, with the exception of KA, have short-period records typical of earthquakes.

A difference in magnitude of 1.8 corresponds to an amplitude ratio of approximately 60, or 35 dB. Such large amplitude variations for these events, having the same body wave magnitude, are illustrated in Fig. I-3. The records presented in the figure are at gains and epicentral distances that make them directly comparable. As seen in Fig. I-3, the seismograms are typical of first- and second-zone continental Rayleigh waves from shallow sources. The Rayleigh wave for event KA is immersed in a Rayleigh wave from an earthquake in Tonga. Figure I-4 shows the three LP components for this event as recorded at the WWSSN observatory at Kabul. The presence of the Rayleigh wave from the southern Russia event is clearly visible because of its high-frequency nature relative to the low-frequency nature of the interfering event. It is interesting to note that the Kazakh event would not have been extractable if the record had been produced by a LASA type long-period or a Lamont Ogdensburg-type instrument, since 6-sec energy (the

dominant period of the Kazakh event) is down in amplitude by more than an order of magnitude from 40-sec energy (the dominant period of the Tonga event). Fortunately, WWSSN long-period instruments are rather broadband: 6- and 40-sec energy have the same magnification which is only a factor of two less than the peak magnification that occurs near 20 sec (see Ref. 4).

The 7 events listed as earthquakes by NOS have been shown to span the earthquake and explosion populations on the M_s:m_b diagram. The Tibetan events which we take to be earthquakes lie nearer the explosion population. The Kazakh event that lies within 100 km of the city of Alma Ata and which occurred on 1 May 1969 at 0400 GMT would be presumed to be an explosion on the basis of M_s:m_b. However, the event is travel-time constrained to a depth of 53 km in the NOS bulletin.

To examine the behavior of tr- -time residuals as a function of depth, thirteen widespread WWSSN stations where first arrival times for the event KA could be precisely determined were used to recompute a hypocenter. Table I-2 gives various hypocentral characteristics based on these picks. Even though the minimum standard deviation (as determined by our location program) occurs for a depth of 39.1 km at 04:00:06 GMT, the error for a surface focus at 04:00:00 GMT is not significantly different. The epicenters corresponding to the various hypocenters differ by less than 3 km. Thus, it is as likely that the event occurred at the surface on the hour as at 40-km depth at 6 sec after the hour.

TABLE I-2
HYPOCENTRAL TEST CHARACTERISTICS FOR EVENT KA

Latitude (°N)	Longitude (°E)	Depth	GMT Time	Standard Deviation
44.10	77.84	0	04:00:00	0.61
44.09	77.83	20	04:00:03	0.58
44.09	77.82	39.1	04:00:06	0.57
44.09	77.82	40	04:00:06	0.57
44.08	77.80	60	04:00:08	0.59

This event exhibits other short-period characteristics that are more typical of explosions than earthquakes but are not strong evidence either way. It has compressional first arrivals where first motion can be clearly seen. The first cycle of motion has a dominant period of 0.8 sec, and the amplitude ratio of the first dilatational peak to the first compressional peak is about 5 to 1. The seismograms also have explosion-like complexity. One first-zone record showing Lg was available at Kabul. It had an amplitude slightly less than the initial arrival. Such a ratio is not definitive as to either a natural or an artificial source.

Thus far, the sum of the evidence on event KA points to its being an explosion. However, this event's short-period records contain an apparent depth phase. Figure I-5 presents the short-period records from LASA and the arrays Yellowknife (YKA) and Warramunga (WRA). The arrival at 7.5 sec after P appears to be pP; it seems to be inverted and to have the same wave shape. The arrival at LASA at about 13 sec after P may be sP. pP-P time puts the focus at

20 to 25 km; sP-pP time puts the focus at 35 to 45 km. With the exception of this phase, event KA should be classified as an explosion. If the event were an explosion, a possible explanation of the second arrival would be a second event. Multiple-explosion experiments have been conducted in the Russian Plowshare program.[5] It seems possible that the second arrival could have been produced in such a manner. If the event is an earthquake, it most likely belongs in the high stress drop – small source dimension class of events which occasionally occur in western North America[1] and possibly in Tibet. In either case, the problem of discrimination for Central Asia is made more difficult by the existence of such events.

I would like to express gratitude to Peter Marshall for a prepublication copy of the paper[2] he co-authored.

T. Landers

B. SOME PRESUMED EXPLOSIONS IN THE SOVIET UNION

Table I-3 lists events which may prove helpful in discrimination studies. All events on this list are believed to be genuine, although down at the very low magnitude end only LASA has contributed. Care has been taken to eliminate PP phases. Several of the events are indicated by the $M_s:m_b$ discriminant to be explosions, and certain events can be associated with experiments described in the literature.[5,6] Others are simply events in aseismic regions. The list should not be regarded either as exclusively containing explosions nor as a comprehensive listing of explosions away from the two regular test sites – Semipalatinsk and Novaya Zemlya.

D. Davies

C. DECONVOLUTION AND THE SOURCE OF A SIBERIAN EARTHQUAKE

The interpretation of seismograms in order to infer the nature of the seismic source is made more confidently if the effects of wave propagation and the recording instrument are considered. Current trends in source studies apply corrections for these effects in the frequency domain, and the subsequent interpretation is based on the resulting spectrum. Although in some respects the spectral approach is preferred, the details of the time history of the source are lost upon transformation, e.g., the earthquake could either begin or end with high-frequency motion and yield the same amplitude spectrum in either case. Propagation and recording effects can be removed by well-established time-domain techniques, and in what follows we describe an attempt to apply these techniques to a specific Asian earthquake.

If P(t) represents the ground motion at a station due to an incident compressional (P) wave, the seismogram S(t) can be represented symbolically as a convolution

$$P(t) * I(t) = S(t) \qquad (I-1)$$

where I(t) is the displacement impulse response of the recording instrument. The method of deconvolution, or inverting Eq. (I-1) in order to gain P(t), is well known.[7] An alternate method may be used to save time if many seismograms recorded on similar instruments are to be deconvolved. If the inverse of I(t), $I^{-1}(t)$, is computed such that

$$I^{-1}(t) * I(t) = \delta(t) \qquad (I-2)$$

where $\delta(t)$ is the delta function, then P(t) may be computed by the convolution

$$P(t) = I^{-1}(t) * S(t) \quad . \qquad (I-3)$$

The advantage of the second method is obvious – only one inversion is required, and S(t) from like instruments may be deconvolved through a convolution with $I^{-1}(t)$.

These techniques are demonstrated in Figs. I-6 and I-7. Figure I-6(a) shows the impulse response of a long-period seismometer used in the WWSSN – this would be I(t). Figure I-6(b) shows the function $I^{-1}(t)$ computed by inverting Eq. (I-2), and Fig. I-6(c) shows the result of a convolution of the functions I(t) and $I^{-1}(t)$. If the inversion process were exact, Fig. I-6(c) would be a delta function, and it is seen that this is not strictly the case. Although Fig. I-6(c) is sharply peaked, the net area under this curve is probably closer to 0 than 1 because Fig. I-6(b) is essentially a differentiator; it enhances high-frequency motion lost through the instrument but, because of its short length, is not as effective in correcting the long-period motion. Figure I-7(a) is the trace of a P-wave recorded on a WWSSN long-period instrument – this would be S(t). Figure I-7(b) shows the result of computing P(t) using Eq. (I-3), i.e., a convolution of Fig. I-6(b) with I-7(a). In this case, the filter $I^{-1}(t)$ was 25 points long and S(t) consisted of 135 samples. Figure I-7(c) shows the function P(t) gained by inverting Eq. (I-1) directly. It is clear that although Figs. I-7(b) and (c) are similar in detail, the latter has retained relatively more long-period motion.

At present, we are using these techniques to deconvolve P-waves recorded on long-period instruments of the WWSSN in an attempt to gain some insight into active faulting processes. We magnify the 70-mm films of the original WWSSN records by successively using a viewer-printer and a copying machine charged with transparent sheets. The transparent sheets are then inserted into the viewer-printer and, finally, the phase of interest is digitized. The entire process before digitization yields a gain of about 30 from the original paper records. A digitization rate of 6 samples/sec is realizable; however, half that rate is found adequate for routine use. Suitable instrument constants are gained by matching the Heaviside acceleration response given by the calibration pulses found on the original records.

Figure I-8 shows the location and fault plane solution of a large earthquake that occurred in eastern Siberia on 18 May 1971. The Earthquake Data Report gives the following parameters for this event:

Origin time	22:44:43.8
Latitude	63.95° N
Longitude	146.11° E
Depth	Normal
Magnitudes (stations)	m_b = 5.8(26), M_s = 6.6(9)

In Fig. I-8, the base map and "main deep faults" are due to Yanshin.[8] The fault plane solution, based on long-period first-motion polarities, is consistent with a left-lateral, vertical strike slip fault striking at an azimuth of 325°. Although this azimuth is roughly parallel to the fault traces given on the map, the latter shows relative motion on nearby faults as right-lateral. In spite of this discrepancy, we take the northwest-southeast plane to represent the faulting surface.

In Fig. I-9, we show the deconvolved vertical long-period P records, P(t), computed using the second method [Eqs. (I-2) and (I-3)] described above. The traces from 28 stations are arranged at the appropriate azimuth relative to the fault plane. These traces represent ground motion at the station with no corrections being made for path propagation. However, differences in station gains have been accounted for so that the relative amplitudes are correct. The reader

TABLE I-3

EVENTS IN ASEISMIC REGIONS AND PRESUMED EXPLOSIONS IN SEISMIC REGIONS OF THE USSR, OTHER THAN PRESUMED EXPLOSIONS IN EASTERN KAZAKH AND NOVAYA ZEMLYA 1966-1971

Date	Time (GMT)	Location	Depth (km)	Magnitude (m_b)	Source of Information	Comments
22 April 1966	02:58:03	47.9°N 47.7°E	33	4.9	CGS	North of Caspian Sea
30 September 1966	05:59:52	38.9°N 64.5°E	33	5.1	ISC	M_s:m_b indicates an explosion. See 21 May 1968.
21 October 1966	04:59:59	43.2°N 77.1°E	0	5.1	See Ref. 6	Two shots in the Medeo region near Alma-Ata. Yields 1.7 and 3.6 kT. Earth-moving purposes.
6 October 1967	07:00:02	57.7°N 65.3°E	33	4.7	CGS	M_s:m_b indicates an explosion. Near Tyumen, east of Urals.
29 March 1968	06:48:30	38°N 68°E	0	4.0	LASA & WWSSN film chips	Baypaza Gorge, near Dushanbe on the Vaksh River. 2 kT of chemical explosive. Earth-moving purposes.
21 May 1968	03:59:11	38.9°N 65.2°E	13	5.4	CGS	M_s:m_b indicates an explosion. See 20 September 1966.
14 June 1968	06:01:18	45°N 55°E	0	4.3	LASA	See 6 December 1969, 12 December 1970 and 23 December 1970. East of the Caspian Sea, in desert.
1 July 1968	04:02:02	47.9°N 48.0°E	33	5.5	CGS	M_s:m_b indicates an explosion. North of Caspian Sea. See 22 April 1966.
2 September 1969	04:59:57	57.4°N 54.9°E	0G	4.9	CGS	M_s:m_b indicates an explosion. Near to Perm in the Western Urals. See 8 September 1969.
8 September 1969	04:59:56	57.4°N 55.1°E	0G	4.9	CGS	M_s:m_b indicates an explosion. Approximately the same location as 2 September 1969.
26 September 1969	06:59:56	45.9°N 42.5°E	0G	5.6	CGS	M_s:m_b indicates an explosion. 300 km west of Cospian, 100 km north of Stavropol.
6 December 1969	07:02:57	43.8°N 54.8°E	0G	5.8	CGS	M_s:m_b indicates an explosion. 200 km east of Caspian in the desert. Same location as 14 June 1968, 12 December 1970 and 23 December 1970.
21 February 1970	07:09:19.6	59.6°N 59.2°E	1	4.3	CGS	50 km from Karpinsk in the Urals. Near a 3.1-kT chemical explosion of 25 March 1968.

TABLE I-3 (Continued)

Date	Time (GMT)	Location	Depth (km)	Magnitude (m_b)	Source of Information	Comments
25 June 1970	04:59:52.4	52.2°N 55.7°E	0G	4.9	CGS	M_s:m_b indicates an explosion. 30 km from Orenburg. See 21 July 1971 and 22 October 1971.
29 November 1970	09:59:01	53°N 68°E	0	3.6	LASA	300 km south of Petropavlovsk.
12 December 1970	07:00:57	43.9°N 54.8°E	0G	6.1	CGS	M_s:m_b indicates an explosion. 200 km east of Caspian, in desert. See 14 June 1968, 6 December 1969 and 23 December 1970.
23 December 1970	07:00:57	43.8°N 54.8°E	0G	6.1	CGS	M_s:m_b indicates an explosion. See 14 June 1968, 6 December 1969 and 12 December 1970.
31 December 1970	05:21:17	52.4°N 74.5°E	0	4.0	LASA	300 km south of Omsk. Possibly at same location as 29 November 1970.
23 March 1971	06:59:56	61.3°N 56.5°E	0G	5.6	CGS	M_s:m_b indicates an explosion. Ural Mountains, 50 km north of Nyrob. Between Pechora and Kama Rivers.
2 July 1971	16:59:53	67°N 69°E	0	4.4	LASA and NORSAR	Near the mouth of the River Ob.
10 July 1971	16:59:59	64.2°N 55.2°E	0G	5.3	CGS	M_s:m_b indicates an explosion. Near Irayel in Ural Mountain region.
21 July 1971	15:49:22	52°N 54°E	0	3.8	LASA	Near site of 25 June 1970 and 22 October 1971.
19 September 1971	11:00:07	57.8°N 41.1°E	N	4.5	CGS	Near Kostroma on the Volga, Western Russia.
4 October 1971	10:00:02	61.6°N 47.1°E	13	5.1	CGS	Near Kotlas, Western Russia.
22 October 1971	05:00:00	51.6°N 54.5°E	6	5.3	CGS	Fairly close to locations of 25 June 1970 and 21 July 1971.
20 December 1971	06:01:54	50°N 45°E	0	3.5	LASA	Southwest Russia.
22 December 1971	06:59:59	48°N 48°E	0	6.5	LASA and NORSAR	North of Caspian Sea. See 22 April 1966 and 1 July 1968.

must remember that since epicentral distances here are in the teleseismic range ($28° < \Delta < 89°$), we are actually sampling the compressional motion from a rather restricted solid angle of the lower focal hemisphere. In spite of these restrictions, there are two features of interest evident in Fig. I-9. The first is that the initial motion is usually emergent, of low amplitude and long period relative to a sharp, high-frequency motion arriving later. It is not clear to us yet whether this high-amplitude motion represents a stopping phase of the fault rupture or a breakout phase generated when the faulting reaches the earth's surface. The second feature of interest is also related to this high-amplitude motion. It may clearly be seen in the right-hand column of traces in Fig. I-9 that the position of this phase changes as a monotonic function of azimuth. Although this feature is not as clear on the traces on the left, we take it as an indication that the source of this earthquake propagated from the southeast to the northwest. In Fig. I-10, we compare the deconvolved trace at BRK with a similar trace (inverted) at ATU. The precise estimation of the elongation of the trace at BKS with respect to ATU is difficult, but is taken to be about 2 to 3 sec. If Θ is the azimuth to a station measured clockwise from the direction of fault propagation, then $\Theta_{ATU} = 349°$ and $\Theta_{BKS} = 105°$. Using these values of Θ, a P-phase velocity of 16 km/sec, and the assumption that the late-arriving high-amplitude phase represents a stopping phase occurring at the end of fault propagation, we would estimate the fault length to be between 30 to 50 km. This result is also based on the assumption of horizontal propagation of rupture on a vertical fault. Estimating the velocity of rupture depends entirely on an accurate determination of the duration of motion at any given station. If, from Fig. I-10, we take the major motion to endure for 8 to 10 sec at BRK, a rupture velocity of 4 to 5 km/sec is implied. This value is higher than the Rayleigh-wave velocity, the maximum rupture velocity predicted by various crack propagation theories. Longer estimates of the duration of motion will yield lower rupture velocities.

J. Filson
C. Frasier

D. WHAT CAUSES DISCRIMINATION?

It has been known for several years that it is possible to discriminate between explosions and shallow focus earthquakes at least at levels where signal-to-noise ratio causes no problems. The $M_s : m_b$ discriminant has been by far the most reliable technique – in essence, explosions generate at least an order-of-magnitude-smaller Rayleigh waves (at 20-sec period) than do earthquakes of the same body wave magnitude (at 1-sec period). The reason why is important, as it may be possible to predict the behavior of the discriminant to low magnitudes. Yet the cause of discrimination is poorly understood. Several explanations have been advanced and these may be divided into two categories: those that attempt to explain discrimination by spectral differences between sources at 1 and 20 sec, and those that attempt to explain discrimination by differences in partitioning of energy between body waves and Rayleigh waves for different sources. There has been extensive discussion of source spectra – the energy partitioning problem has received less attention, probably because it is rather difficult to describe an earthquake mathematically. I propose to present some evidence which, I believe, makes invalid any argument that source dimensions or a source-time function alone are the cause of discrimination.

In several previous SATS, I have remarked that core reflections such as PcP and PKiKP offer an important view of the seismic source. There appear to be several reasons for this. The

core boundary seems to be a clean reflector of seismic energy. Seismic rays do not have to bottom in a vertically or laterally heterogeneous region. Regions of multiple P-wave arrivals are avoided. Plates and other near-source structure are left rapidly by near-vertical rays. S-to-P conversion near source by transmission through (on average) horizontal layering is slight. For a good view of core phases, the directional capability of an array is highly desirable, but it is possible that PKP may also prove valuable in some epicentral ranges.

The striking thing to be noticed about the use of core phases is how often they sharpen up the short-period view of the source when all these effects mentioned in the last paragraph are minimized. Figure I-11 shows such a case. The duration of radiation of short-period energy, apparently many seconds for P, reduces drastically for PcP. In fact, PcP from Longshot, with a comparable body wave magnitude, and from a relatively nearby region lasts as long as, if not longer than, PcP from this earthquake. It may be argued[9] that, with certain provisos, the fault zone for this earthquake has a maximum half-dimension of 1.5 km. We make the assumption that the start and stop of the earthquake are all included within the initial P-wave and the source's radiation is described by Savage's[10] model. If this is so, and since the event discriminates (M_s = 5.5, M_s for Longshot = 4.0), we cannot invoke either source dimensions or an elongated source-time function as leading to discrimination. We could, of course, have a radically different source-time function between the two events, such as a step for an earthquake and an impulse for an explosion, but nowhere in the literature is there any good evidence that explosions are dominantly impulsive in displacement. Indeed, it appears that when many explosions have been studied as a suite,[11] it has been impossible to make a clear-cut statement about source-time functions, as some appear to have small impulsive terms while others appear to be simple steps. (Filson and Lande reached a similar conclusion in the SATS dated 31 December 1970, DDC AD-718971.) All discriminate easily, however. I conclude, therefore, that it would be difficult to sustain an argument that source-time functions or source dimensions control discrimination.

D. Davies

E. THE R_g PHASE FROM EXPLOSIONS AT NEAR DISTANCES

An observational study of the R_g phase has been made using two stations within 300 km of explosive sources at the Nevada Test Site. R_g is taken to represent a high-frequency Rayleigh-type motion which propagates in crustal wave guides. The chief purpose of the experiment was to determine if R_g could be used to discriminate between contained underground explosions and those used for excavation purposes. The maximum amplitude of this phase was measured on short-period vertical instruments at Mina, Nevada (MN-NV, Δ = 240 km) and Kanab, Utah (KN-UT, Δ = 290 km) from explosions detonated under various conditions. This maximum amplitude is usually recorded 35 to 50 sec following the initial P-wave arrival at these distances, and is not a well-defined phase but consists of a series of high-frequency excursions of larger amplitude than the preceding motion. The amplitudes (peak to trough) of the initial (first full cycle) P arrival (P_n) and the long-period fundamental mode Rayleigh-wave motion (L_R) were also measured for comparison with the R_g measurements. The amplitude measurements were corrected for instrument response and the average using the two stations computed directly. Only explosions with source conditions listed by Springer and Kinnaman[12] were used in this study.

In Fig. I-12, the average surface wave amplitudes $\overline{L}_R$ are plotted against $\overline{P}_n$ for some 24 explosions; various symbols are used to denote the source medium and location. The explosions termed "Plowshare excavation" by Springer and Kinnaman[12] are circled; the explosion described as a "Plowshare experiment" is enclosed in a square. Given the scatter of the data in Fig. I-12, there is nothing remarkable to define the excavations except that their surface wave amplitudes may be larger, relative to $\overline{P}_n$, than some of the contained explosions. In Fig. I-13, we have plotted $\overline{R}_g$ vs $\overline{L}_R$. Here, $\overline{R}_g$ for at least one of the excavations (named Sedan, detonated in alluvium at Yucca Flat) is significantly lower relative to $\overline{L}_R$; however, the same is true for the explosions named Palanquin and Scroll, not specifically described as excavations. $\overline{R}_g$ for the other excavation event Schooner is low but not greatly so. The most interesting aspect of Fig. I-13 is the apparent difference in dependence of $\overline{R}_g$ upon $\overline{L}_R$ when compared with Fig. I-12 where the data may be roughly approximated by a line with a slope of 0.7 while a less steep line would represent the data of Fig. I-13. If we take $\overline{L}_R$ to be a measurement of relative yield, we must conclude that explosions of larger yield do not generate as much $\overline{R}_g$ relative to P as do smaller ones, due either to their size or their greater depth.

In Fig. I-14, we test the latter hypothesis by plotting the ratio $\overline{\gamma}$ (where $\overline{\gamma} = \overline{L}_R/\overline{R}_g$) vs source depth. It is clear from this figure that $\overline{\gamma}$ increases with depth, the deeper events being relatively more efficient in coupling energy into L_R than into R_g. Additionally, the excavation explosions are now clearly separated from the contained explosions at the same depth; however, Palanquin and Scroll have $\overline{\gamma}$ values nearer the excavation explosions than to the contained events. We cannot assume Palanquin was an excavation device, being described only as a "Plowshare experiment" in the source list. The source medium of Scroll is described as "tuff (volcanic ash)," which may account for its high value of $\overline{\gamma}$.

Of course, in a relevant application of these empirical results, the depth of the explosion will be unknown. In Fig. I-15 we have plotted $\overline{\gamma}$ vs $\overline{P}_n$, both quantities which are measureable from a seismogram. Here Schooner, the Pahute Mesa excavation in tuff, plots only slightly higher than explosions contained in tuff at Yucca Flat; however, the value of $\overline{\gamma}$ for Sedan is about an order-of-magnitude greater than a contained alluvium explosion with the same P_n value. Again, $\overline{\gamma}$ for Scroll is high and in this case that of Palanquin is not anomalous.

To summarize and conclude briefly, we have measured the amplitudes of P_n, R_g, and L_R at two stations within 300 km of 24 explosions. The ratio L_R/R_g appears to increase with depth, and excavation explosions show a value of this ratio greater than those of contained explosions at a similar depth. This ratio, relative to P_n amplitude, is markedly higher for an excavation explosion in alluvium compared with contained explosions at the same site. The excavation explosion in tuff does not show this feature to such an extent; however, no data for a contained tuff event of the same P_n amplitude have been considered thus far.

J. Filson
L. Lande

REFERENCES

1. M. Wyss and J.N. Brune, "Seismic Moment, Stress, and Source Dimensions for Earthquakes in the California-Nevada Region," J. Geophys. Res. 73, 4681-4694 (1968).
2. P.D. Marshall and P.W. Basham, "Discrimination Between Earthquakes and Underground Explosions Employing an Improved M_s Scale," Geophys. J. R. Astr. Soc. (in press).
3. J.F. Evernden, "Study of Regional Seismicity and Associated Problems," Bull. Seismol. Soc. Am. 60, 393-446 (1970).
4. T. Powell and D. Fries, "Handbook: World Wide Standard Seismograph Network," University of Michigan (1964).
5. O.L. Kedrovskiy, "Prospective Applications of Underground Nuclear Explosions in the National Economy of the USSR," International Atomic Energy Agency Report, Vienna (1970).
6. F.F. Aptikayev, et al., "Results of Scientific Observations During the Blast in Medeo," Vestnik Akademii Nauk. Kazakhokay SSR 23, 30-40 (1967).
7. N. Levinson, Appendix B to Time Series by Norbert Wiener (M.I.T. Press, Cambridge, 1949).
8. A.L. Yanshin, editor, 1966 Tectonic Map of Eurasia (Geological Institute of the Academy of Sciences, USSR, Moscow, 1966).
9. D. Davies and A.M. Ziolkowski, "Short-Period P-Wave Observations and Inferences About the Seismic Source," Geophys. J. (in press).
10. J.C. Savage, "Radiation from a Realistic Model of Faulting," Bull. Seismol. Soc. Am. 56, 577-592 (1966).
11. G.C. Werth and R.F. Herbst, "Comparison of Amplitudes of Seismic Waves from Nuclear Explosions in Four Mediums," J. Geophys. Res. 68, 1463-1475 (1963).
12. D.L. Springer and R.L. Kinnaman, "Seismic Source Summary for U.S. Underground Explosions, 1961-1970," Bull. Seismol. Soc. Am. 61, 1073-1098 (1971).

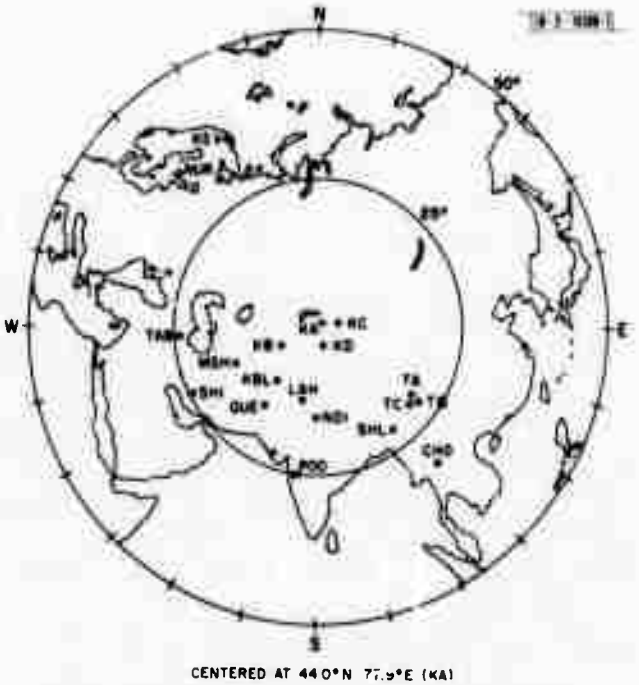

Fig. I-1. Map of Eurasia showing locations of 12 WWSSN stations (squares) employed to analyze 7 events (crosses) studied in this SATS. Refer ta Table I-1 for event data. Great circle paths between events and stations are approximately straight lines.

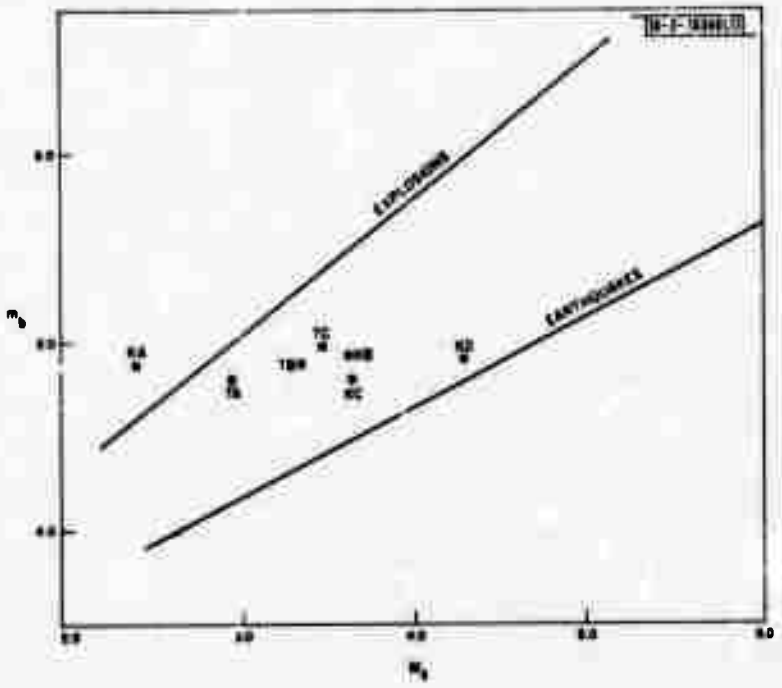

Fig. I-2. M_s:m_b relationship for all events. m_b values are those computed by NOS. M_s values were computed using scheme proposed by Marshall and Basham.[2] Trend lines represent least-square linear behavior of Eurasian explosions and earthquakes as determined in aforementioned paper. All events studied here were listed as shallow focus earthquakes in NOS bulletin.

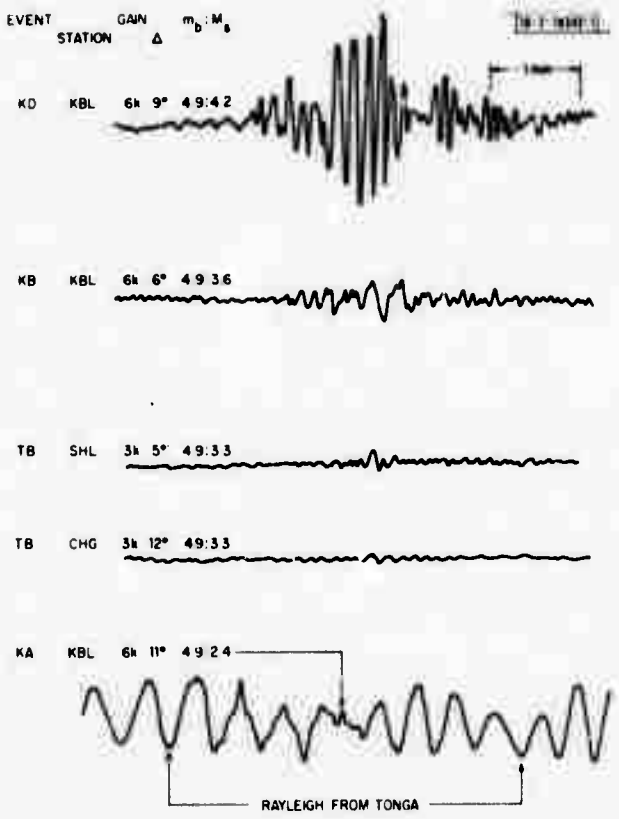

Fig. I-3 Vertical components of Rayleigh waves from events KA, TB, KB, and KD at comparable distances and gains. KD's seismogram has amplitudes that are slightly smaller than average continental Eurasian earthquake with same m_b. High-frequency Rayleigh wave from event KA rides atop interfering low-frequency Rayleigh wave from event in Tonga (m_b = 6.0).

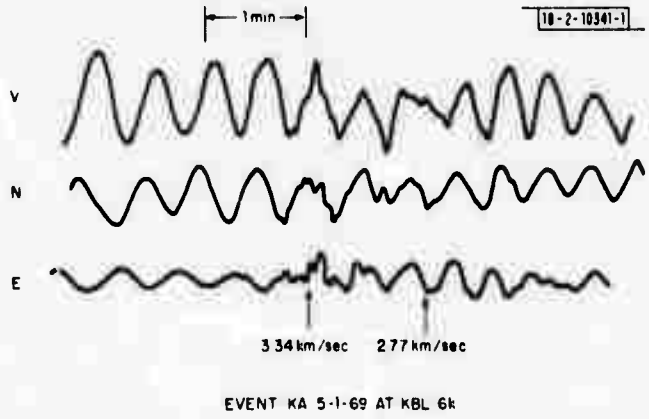

Fig. I-4. Three components of surface waves generated by event KA as recorded by Kabul. Energy arriving with group velocity of 3.34 km/sec may be either Love or higher-mode Rayleigh waves.

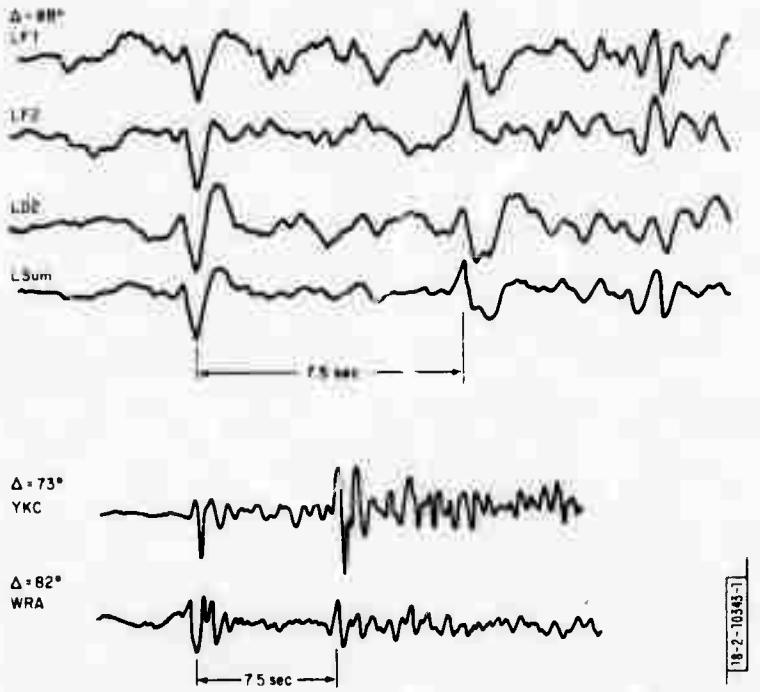

Fig. I-5. Short-period signals from event KA as recorded by arrays at LASA, Yellowknife, and Warramunga, showing apparent depth phase and waveform simplicity.

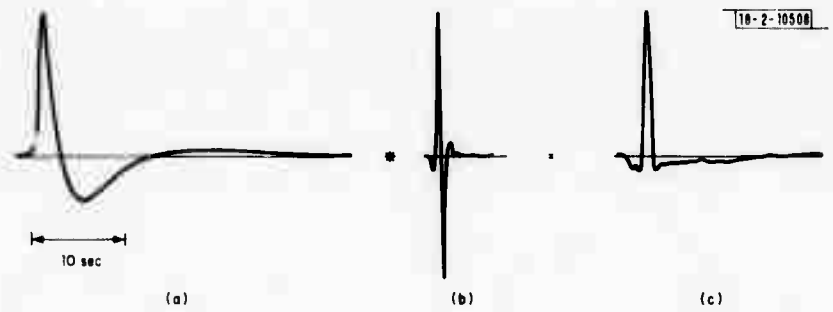

Fig. I-6. (a) I(t), the impulse response of long-period seismometer. (b) $I^{-1}(t)$, the inverse impulse response computed using Eq. (I-2). (c) Result of $I^{-1}(t) * I(t)$. If computation of $I^{-1}(t)$ were exact, this should be a delta function.

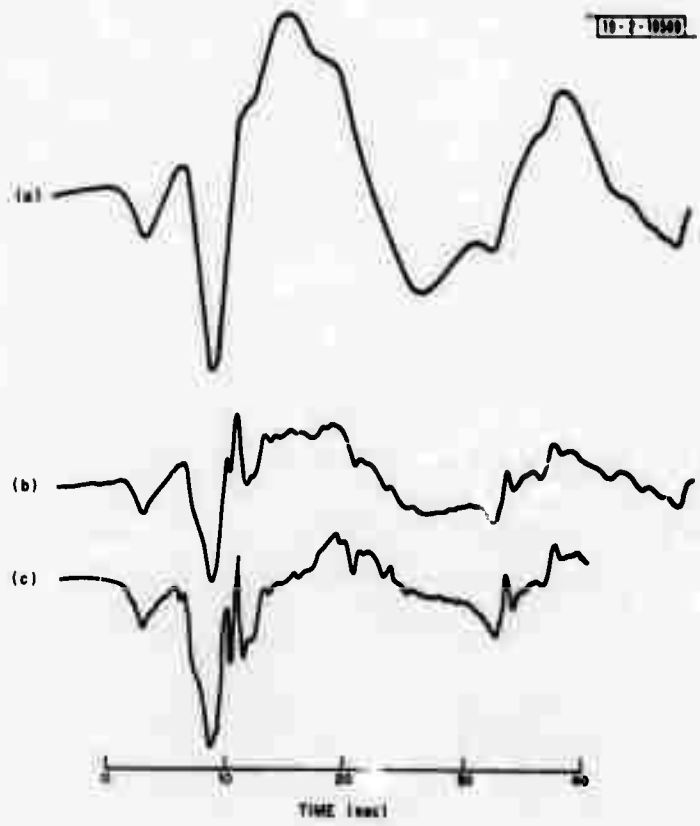

Fig. I-7. (a) A long-period P-wove os recorded, S(t). (b) Ground motion P(t) computed using Eq.(I-3), i.e., $I^{-1}(t) * S(t)$. (c) Ground motion P(t) computed by direct inversion of Eq.(I-1).

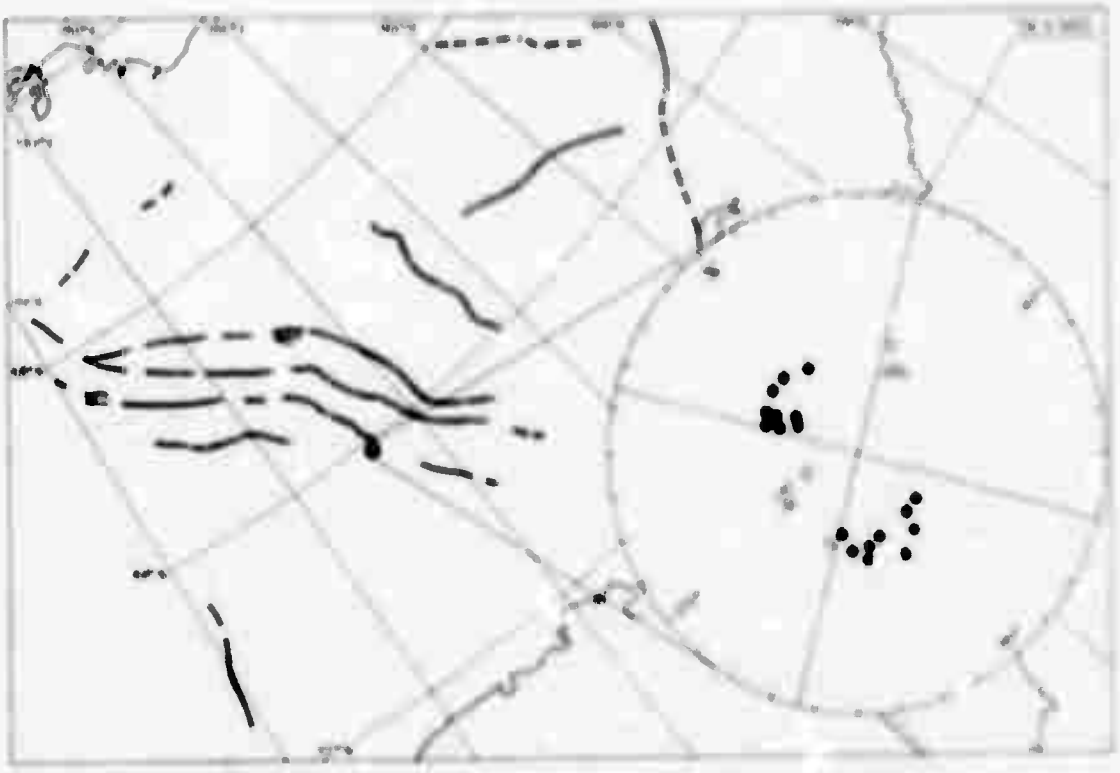

Fig. II-2. Source region map and fault plane solution of Sikaiana earthquake of 28 May 1971. Base map and "major deep faults" (outlined lines) are due to Wyss[8].

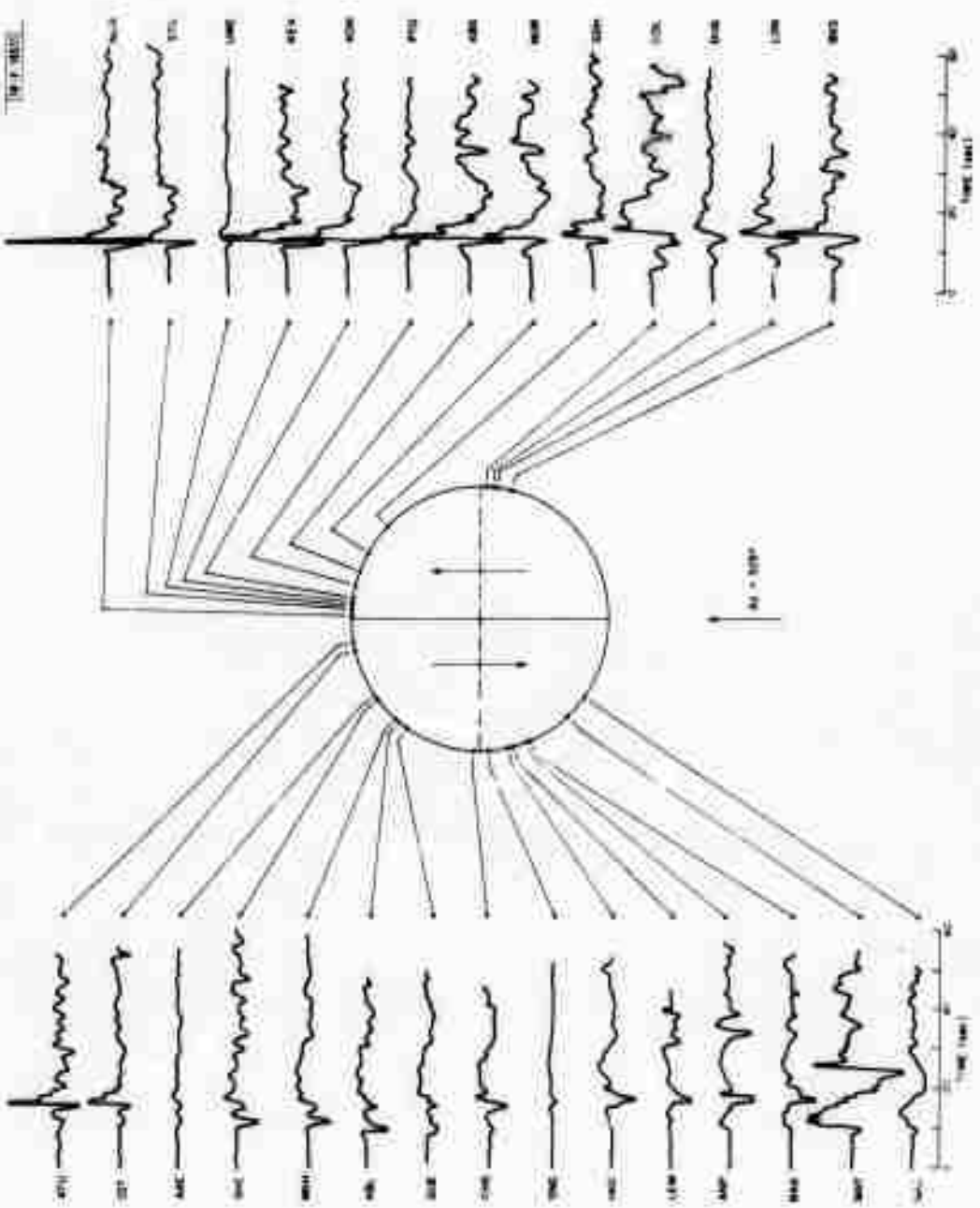

Fig. I-9. Azimuthal variation of deconvolved, vertical long-period P-waves with respect to fault plane.

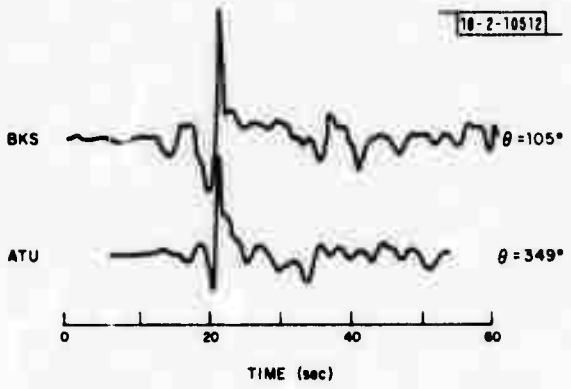

Fig. I-10. Deconvolved P-waves at ATU and BKS showing elongation at BKS taken to be result of fault propagation.

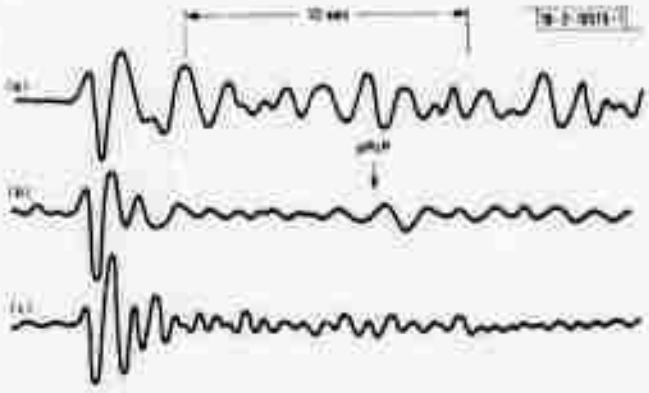

Fig. I-11. Short-period LASA P-wave signals from seismic events in Aleutians; (a) and (b) traces are P and PcP from Komandorsky event of 20 January 1969, and (c) trace is PcP from Longshot.

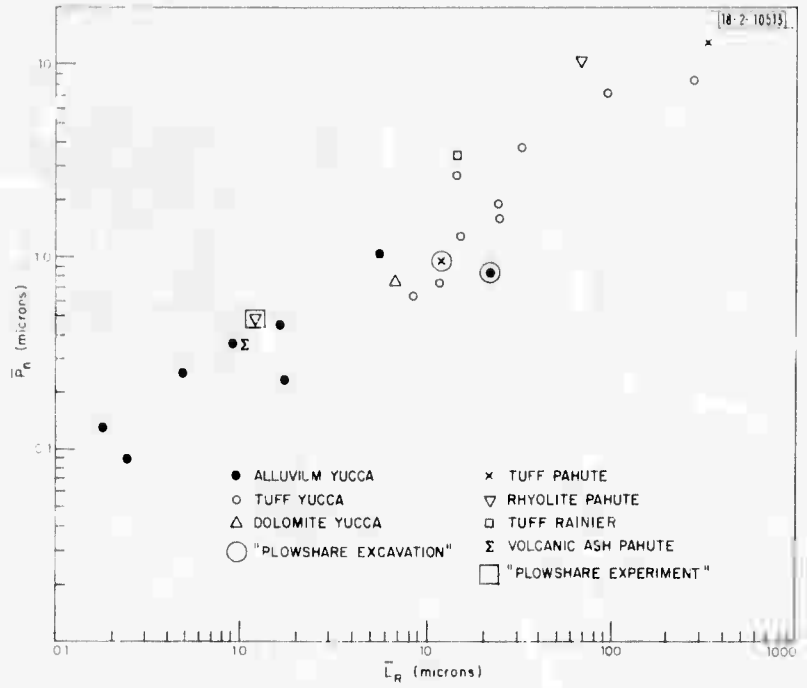

Fig. I-12. Average of $\bar{P}_n$ amplitude at MN-NV and KN-UT plotted vs average $\bar{L}_R$ amplitude.

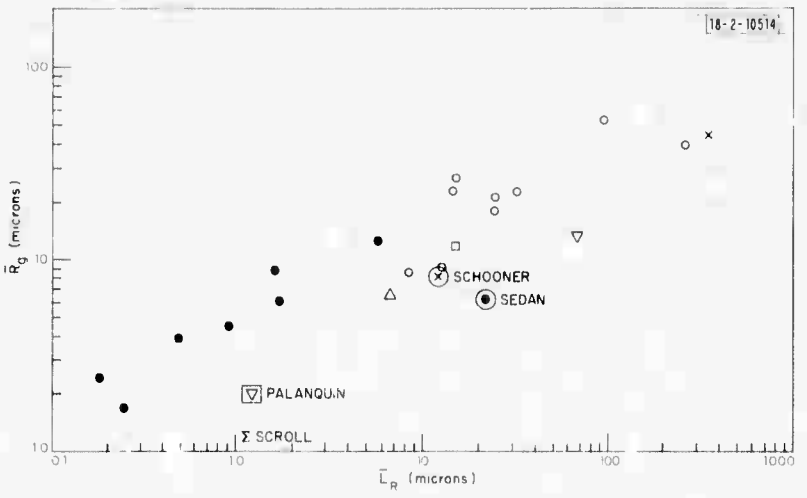

Fig. I-13. Average maximum $\bar{R}_g$ amplitude plotted vs average $\bar{L}_R$ amplitude.

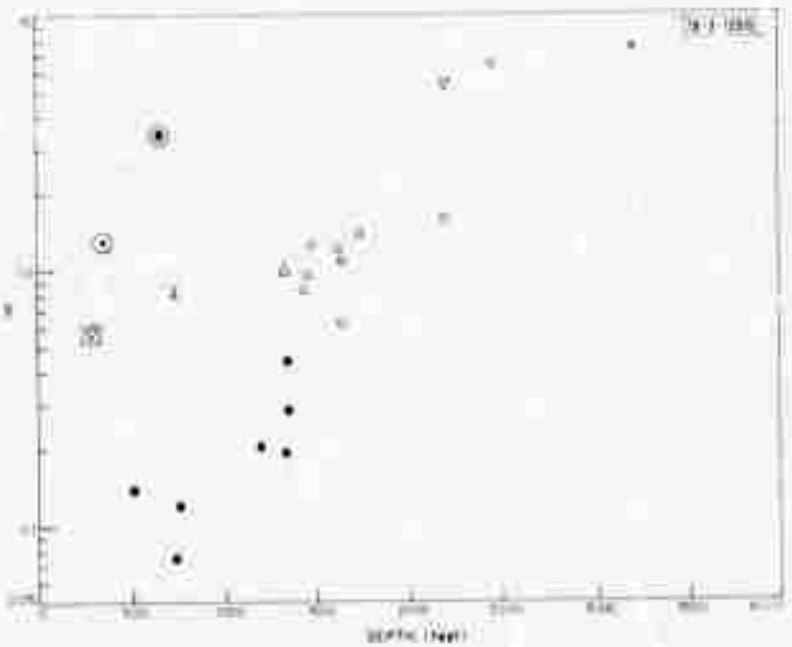

Fig. I-14. Average value of $\overline{\gamma}$, where $\overline{\gamma} = \overline{L}_R/\overline{R}_g$, plotted vs depth of explosion.

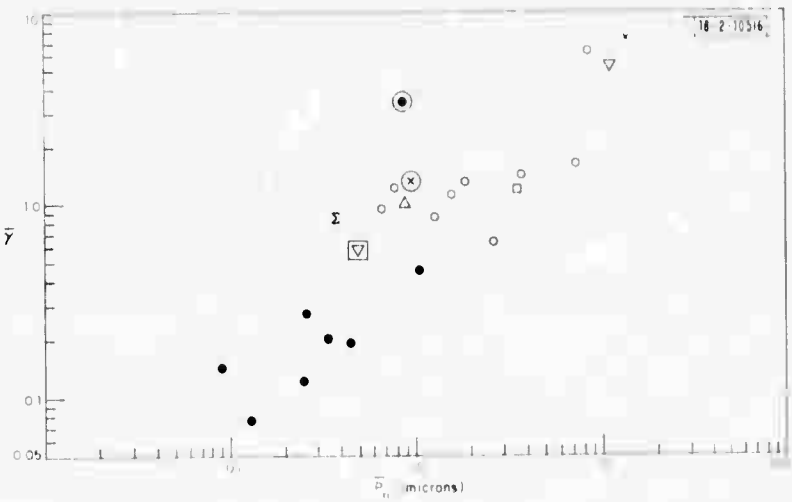

Fig. I-15. $\overline{\gamma}$ plotted vs $\overline{P}_n$.

II. PROPAGATION

A. THE EFFECT OF LATERAL HETEROGENEITY UPON SURFACE WAVE PROPAGATION

In several recent SATS, the problem of body wave propagation in laterally heterogeneous earth models has been considered, with a view to predicting how variations in the earth may distort seismic observations and complicate the discrimination problem. We found that pronounced focusing and defocusing (or shadowing) of energy can occur and will introduce systematic errors into measurements of body wave magnitude. Our knowledge of the earth's internal structure is, however, not yet good enough to enable us to make quantitative predictions of these effects in general, although we can probably predict shadow locations for sources in island arcs with reasonable accuracy.

For surface waves, similar propagation effects occur, and they are more amenable to numerical calculation and prediction, since surface wave velocities are functions of two spatial coordinates, rather than three, and are correlated with known geologic and tectonic features. Furthermore, our seismic discrimination capability is currently limited by the surface wave detection threshold, so reliable path corrections would be of great value. The ability to reliably calculate propagation effects might, in fact, lower the surface wave detection threshold by facilitating the design of matched filters.

To analyze surface wave propagation, we have used geometrical ray theory – much as is commonly done for body waves. For surface waves, however, some additional complications arise because of dispersion. In particular, in a heterogeneous dispersive medium the group and phase velocities do not generally have the same direction. By considering the interference of two plane waves with slightly different frequencies ω and wavenumber vectors $\bar{k}$, it can be seen that the group slowness is given by

$$\bar{S}_G = \frac{\partial \bar{k}}{\partial \omega} \quad .$$

Since $\bar{k}$ is a function of the initial parameters of a ray and ω, as well as the observation point, the calculation of either the magnitude or the direction of the group slowness is not easy. However, since for any given source

$$\bar{k}(\bar{r}, \omega) = k(\bar{r}, \omega)\, \bar{n}(\bar{r}, \omega)$$

where $\bar{n}$ is a unit vector normal to the phase wavefronts, and $\bar{r}$ is the position vector, we have

$$\frac{\partial \bar{k}}{\partial \omega} = \frac{\partial k}{\partial \omega} \bar{n} + k \frac{\partial \bar{n}}{\partial \omega} \quad .$$

Since $\bar{n}$ is a unit vector $(\partial \bar{n}/\partial \omega) \cdot \bar{n} = 0$ and

$$\frac{\partial \bar{k}}{\partial \omega} \cdot \bar{n} = \frac{\partial k}{\partial \omega} \quad .$$

This result says that although the actual group slowness vector is difficult to calculate, its component in the ray direction is the conventional (and easily calculable) group slowness for a homogeneous medium. The group delay could be obtained by integrating the group slowness along any path, but for the phase ray path, this task is greatly simplified.

One of the most striking pieces of evidence that lateral heterogeneity significantly affects surface wave propagation is the discovery by Capon[1] that Rayleigh waves observed at LASA often travel in directions greatly different from the great circle azimuth to the event that generated them. Figure II-1, for example, shows the paths inferred by Capon to have been followed by the Rayleigh waves from an earthquake in the Kuril Islands. Capon felt that most of the observations he made could be explained by refraction and/or reflection at continental margins. In order to check this assertion, a regionalized earth model consisting only of continents and oceans was constructed and used for ray-tracing calculations. The phase velocities for oceans and continents were assumed to be 3.50 and 3.98 km/sec at 20-sec periods, and the model was specified in terms of numerical values on a 5° × 5° latitude-longitude grid. The resulting ray paths, shown in Fig. II-2, look remarkably similar to those inferred by Capon, and strikingly confirm the importance of continental margins which, in this case, have deflected the rays by total internal reflection. Currently, work is being done to increase the amount of detail in the model, to see how well propagation effects can be predicted quantitatively.

B. R. Julian

B. TRAVEL-TIME STUDY USING DEEP EARTHQUAKES AND LATERAL HETEROGENEITIES IN THE DEEP MANTLE

An attempt has been made to refine the travel-time curve for teleseismic P-waves using data from deep-focus earthquakes. This approach was used in order to minimize the bias introduced into travel times by lateral heterogeneities in the upper mantle, which are particularly severe near island arcs, where seismic activity is concentrated. The raw data used (nearly 4000 arrival times from 59 earthquakes) were taken from bulletins of the International Seismological Centre and the National Ocean Survey (NOS), and were winnowed to eliminate gross errors by comparing data for several earthquakes in each source region. An iterative procedure of relocating the events, modifying the travel-time curve and station corrections, relocating the events, etc. was then used to determine finally the average travel-time curve and a set of station corrections. The method will be described in detail in a paper now being prepared.

Figure II-3 shows the travel-time curve derived for a focal depth of 550 km. An ambiguity still remains with regard to the absolute values of the times, since the origin times of the earthquakes cannot be determined independently. We have used data from Nevada Test Site explosions, where the structure of the upper mantle is fairly well known, to estimate this "D.C. component," and found that 1.49 sec should be subtracted from the values in Fig. II-3. This is the value which would apply to a deep-focus earthquake in Nevada.

The general shape of our curve is similar to those found by other workers (e.g., Herrin, et al.[2]) although our absolute times are about 1 to 1.5 sec later than Herrin's. Beyond 85°, however, the trend of our curve is decidedly different from most others and, moreover, is subject to large regional variations. The increased scatter of the data beyond 85° is evident in Fig. II-3. We suggest that this effect is caused by regional variations in the structure of the deep mantle. Statistical tests establish clearly that the variations are systematic, not random, and the only systematic error which might be strongly distance dependent is one caused by variations near the bottoming points of the rays. Figure II-4 shows regions believed to have high and low velocities in the deep mantle. Similar analysis was performed for other depths and very few significant variations could be found. Work is currently being carried out to refine these measurements,

to obtain coverage of more of the earth, and to include other properties such as shear velocity and attenuation.

B. R. Julian
M. K. Sen Gupta

C. THE ARRAY LOCATION PROBLEM

The standard technique for locating with an array such as LASA is to fit a least-squares plane wave to the arrival times at many sensors and hence to determine $dT/d\Delta$ and azimuth for the incoming wave. We soon realized that this approach was unsatisfactory in that the signal arrival times often did not lie close to the plane predicted for earthquakes from known locations. Two separate components may be identified for this misfit. An incoming plane wave is unlikely to traverse the crust beneath LASA without some degree of corrugation being acquired from small-scale geological heterogeneities. On the other hand, the best-fitting least-squares plane wave, in which we attempt to average out these corrugations, may also have a dip (or $dT/d\Delta$) and azimuth different from that predicted by standard travel-time tables. It is this effect which we consider here. Of course, routine operation of the array for bulletin production purposes circumvents the scientific problem, since empirical corrections may be applied. However, when an event in a new area has to be examined, it may be impossible to interpolate corrections adequately. Thus, we need to have a good understanding of the cause of array mislocation.

Three causes may be considered:

(1) If there is broad-scale structure beneath LASA, such as a dip of the Moho, there will be a smooth bias in the mislocation. This has been extensively studied, notably by Greenfield and Sheppard[3] and by Engdahl and Felix.[4]

(2) If the reference $dT/d\Delta$ tables (Jeffreys-Bullen) were incorrect at some distances, the dip (but not the azimuth) of the planes would be affected for all events at these distances.

(3) If there is lateral heterogeneity in the earth, rays will not necessarily trace great circle paths, and $dT/d\Delta$ and azimuth anomalies will be equally likely. The scale of these anomalies may be inferred from LASA data. Near-source structure falls within this category.

In order to attempt to isolate these three effects, we show in Fig. II-5 an "array diagram." The radial coordinate is $dT/d\Delta$, the azimuthal coordinate is azimuth. Each event studied is represented by an arrow, the head of which indicates the expected position on the diagram if the NOS location were correct, if the J-B tables for $dT/d\Delta$ were accurate, if there were no lateral heterogeneity, and if there were no varying structure under the array. The tail of each arrow represents the measured $dT/d\Delta$ and azimuth (hoping that corrugations on the wave front will introduce no unusual bias). Thus, the arrow length and direction indicate the extent to which the conditional clauses above are satisfied.

The array diagram (thinned somewhat) is for a large population of events recorded at LASA from 1967 through 1969. We emphasize that no prior corrections have been made in the $dT/d\Delta$ and azimuth measurements – these are raw data. The problem is to isolate the different causes for arrows not to be of zero length. We shall assume at the outset that the NOS location is correct – which is probably an acceptable assumption at the precision to which we are working. The three remaining sources of bias then affect the array diagram in somewhat different ways.

A smooth distribution of arrows, all approximately of equal length and all pointing in the same direction would characterize bias introduced beneath the array. A distribution of arrows in which radial terms dominated and were of equal magnitude at all azimuths would characterize bias arising from use of an incorrect (globally) $dT/d\Delta$ curve. A distribution of greater complexity would point to near-source or propagation path bias, including equally azimuthal and $dT/d\Delta$ anomalies.

It is clear from Fig. II-5 that the situation is immensely complex. Can we extract even a simple structure beneath the array from this? We show in Fig. II-6 the distribution of arrow lengths and directions, and to the extent that this is a random sampling we may conclude that there is a mean bias to the north of 0.25 sec/deg. We tentatively associate this bias with the smooth effects that would be introduced by structure beneath the array and which would move the tail of each arrow 0.25 unit south.

The arguments for the relative merits of heterogeneity near source and along propagation path are complicated and will be listed at length in a forthcoming publication. The array structure bias is smooth and we are discussing rapid fluctuations in the array diagram. Thus, we are confident that our assertions are truly about the source and propagation path. We see no compelling evidence that there is a global $dT/d\Delta$ anomaly shown by the array. As a result of detailed analysis of Fig. II-5, we conclude:

(1) There is lateral heterogeneity in the earth's mantle with good indications that near the core mantle boundary there may be horizontal structures of 100-km extent or less.

(2) The amplitude of these anomalies suggests velocity fluctuations of perhaps 5 percent, but a full interpretation will be very difficult with a data set restricted by seismicity.

(3) Regions of marked lateral variation near the core boundary include areas beneath Hawaii, the Galapagos and the mid-Atlantic Ridge north of Iceland. This result may be of use in examining Morgan's[5] hot-spot hypothesis.

(4) Lateral heterogeneity is by no means confined to the deepest mantle. There is some evidence that sub-continent and sub-ocean structural differences may be detectable.

(5) Many anomalies remain to be understood, particularly in the north-west quadrant as Chinnery[6] has described.

(6) In any study using arrays to examine the velocity structure of the earth, it is imperative to see both $dT/d\Delta$ and azimuth of incoming signals, as azimuth deviations can be as great as 10° and bear as much useful information as $dT/d\Delta$ anomalies – indeed, the two cannot be separated in a heterogeneous earth.

From an operational point of view, we remark that the location of an event in a new and aseismic area will present problems not necessarily alleviated by extrapolation of existing results. We are now starting to examine NORSAR in a similar way.

D. Davies
R. M. Sheppard

REFERENCES

1. J. Capon, "Analysis of Rayleigh-Wave Multipath Propagation at LASA," Bull. Seismol. Soc. Am. 60, 1701-1731 (1970), DDC AD-716084.
2. E. Herrin, E.W. Tucker, J.N. Taggart, D.W. Gordon and J.L. Lobdell, "Estimation of Surface Focus P Travel Times," Bull. Seismol. Soc. Am. 58, 1273-1291 (1968).
3. R.J. Greenfield and R.M. Sheppard, "The Moho Depth Variations under the LASA and Their Effect on dT/dΔ Measurements," Bull. Seismol. Soc. Am. 59, 409-420 (1969).
4. E.R. Engdahl and C.P. Felix, "Nature of Travel-Time Anomalies at LASA," J. Geophys. Res. 76, 2706-2715 (1971).
5. W.J. Morgan, "Convection Plumes in the Lower Mantle," Nature 230, 42-43 (1971).
6. M.A. Chinnery, "Investigations of P-Wave Arrivals at LASA," Final Technical Report, Department of Geological Sciences, Brown University (August 1971).

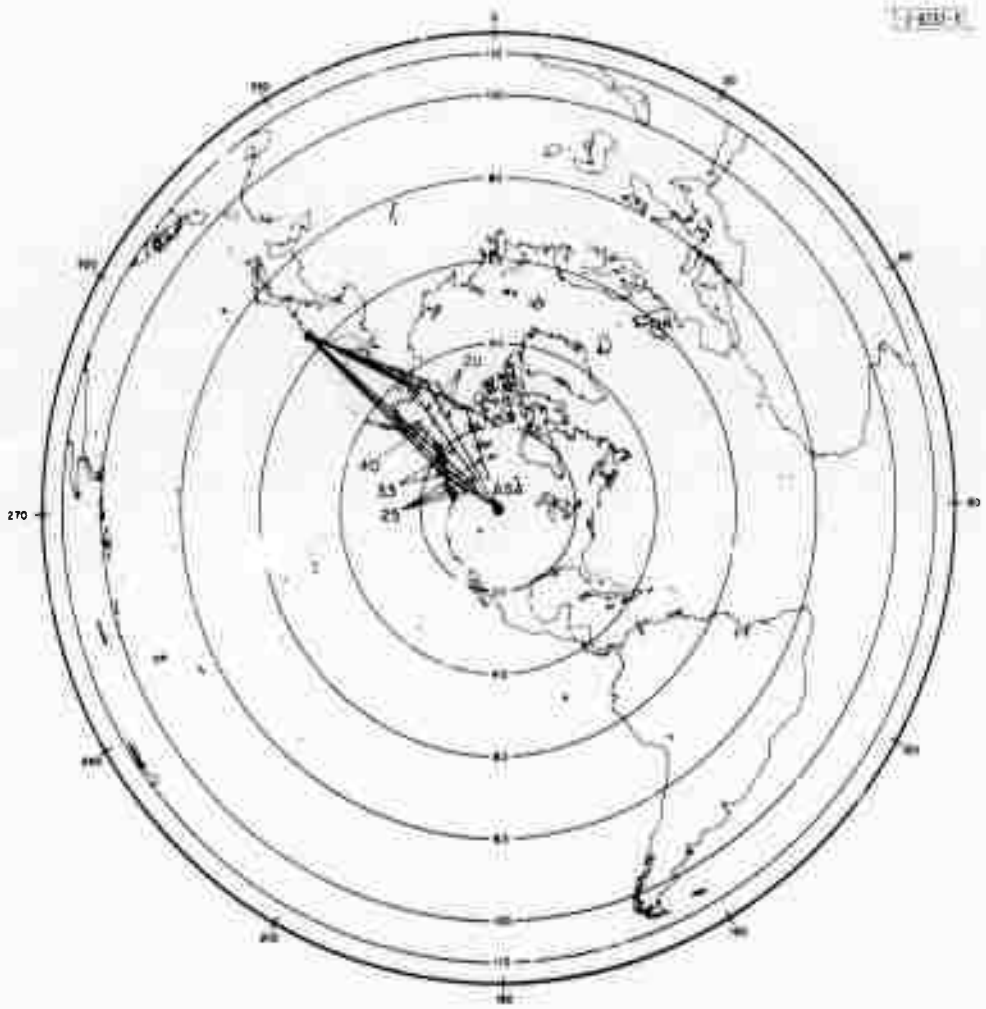

Fig. II-1. Rayleigh-wave propagation paths for earthquakes in Kuril Islands inferred by Capon[1] from observations made using LASA.

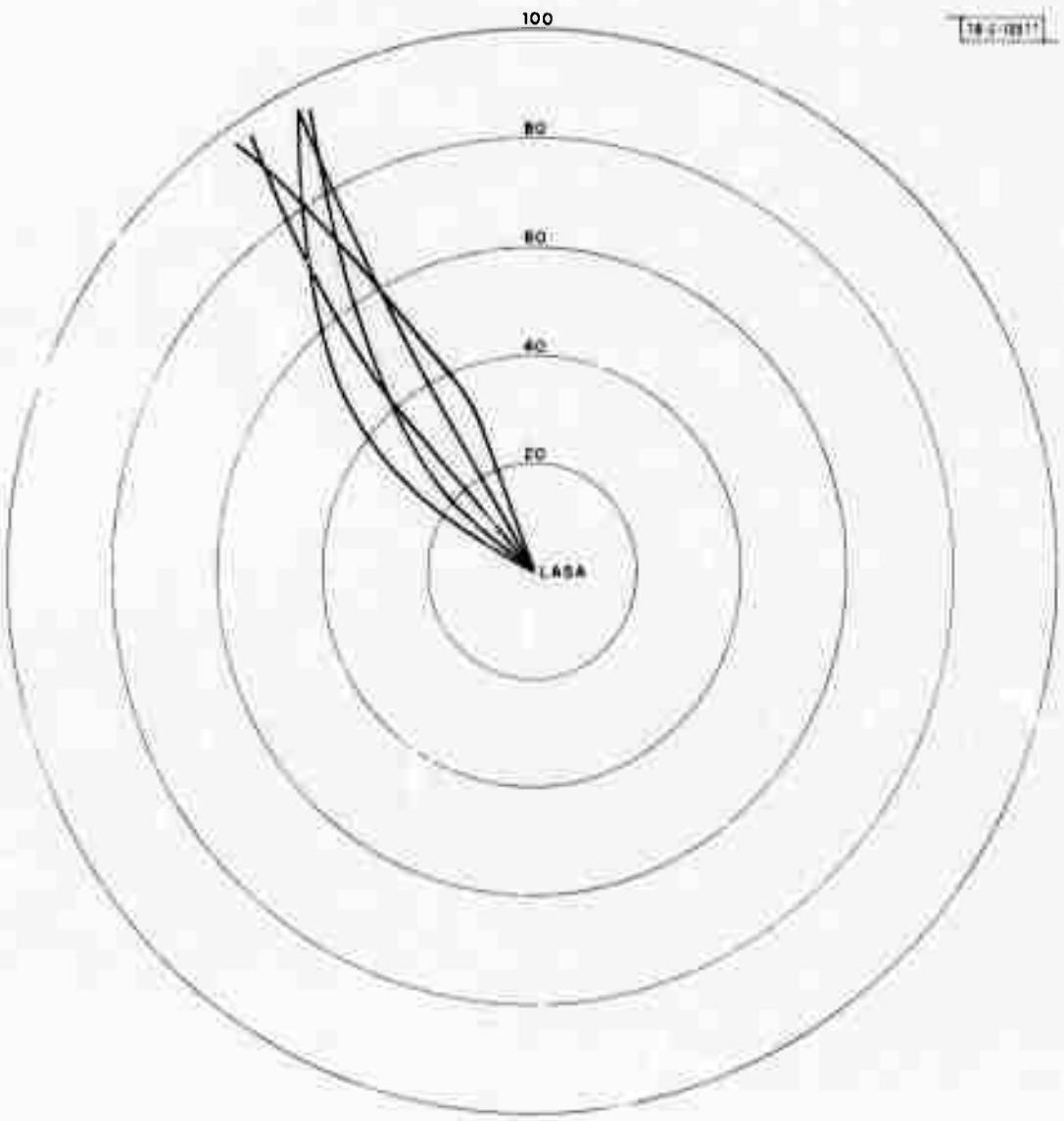

Fig. II-2. 20-sec Rayleigh-wave paths to LASA calculated from simple regionalized model containing only oceans and continents.

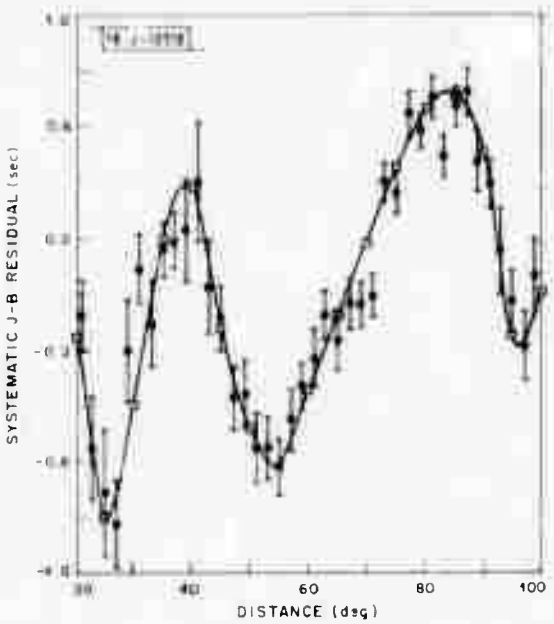

Fig. II-3 P-wave travel-time curve derived in this study, expressed in terms of systematic deviation from values in Jeffreys-Bullen tables (focal depth = 550 km). Mean values and standard errors of mean (vertical bars) in 2° intervals are shown, as are smoothed values at 5° intervals (squares).

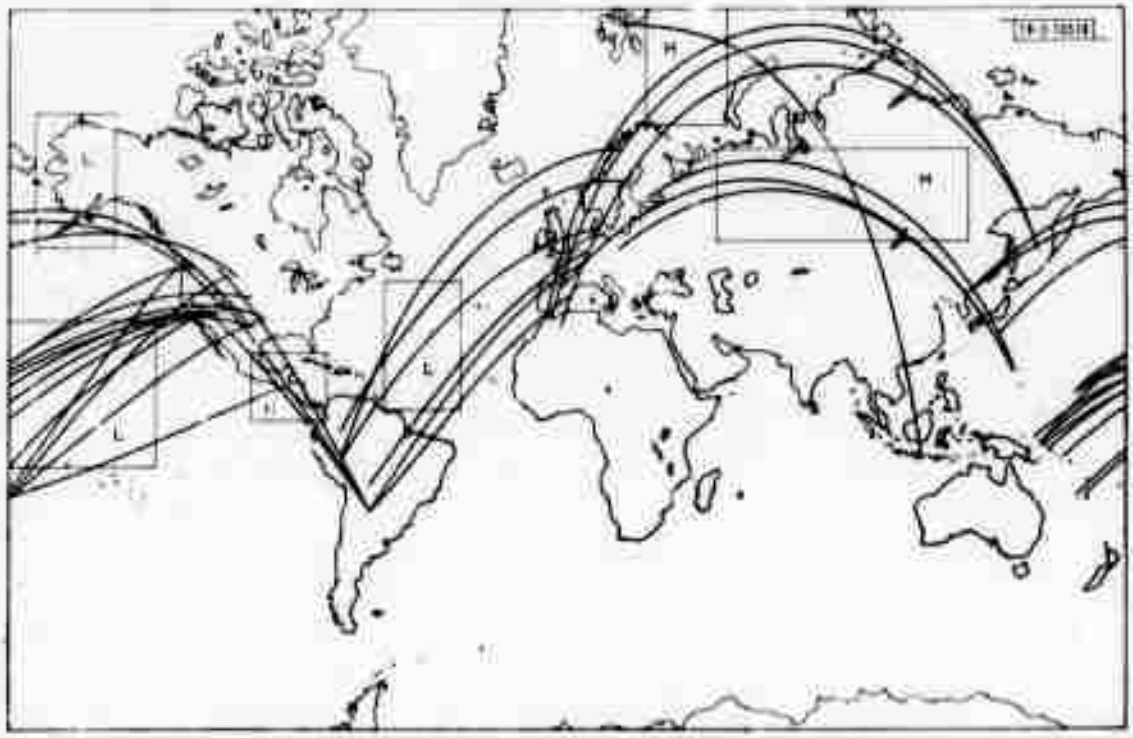

Fig. II-4. Suggested regions of low (L) and high (H) compressional velocities in deep mantle (2600 km < depth < 2900 km). Ray paths used (thinned) are shown.

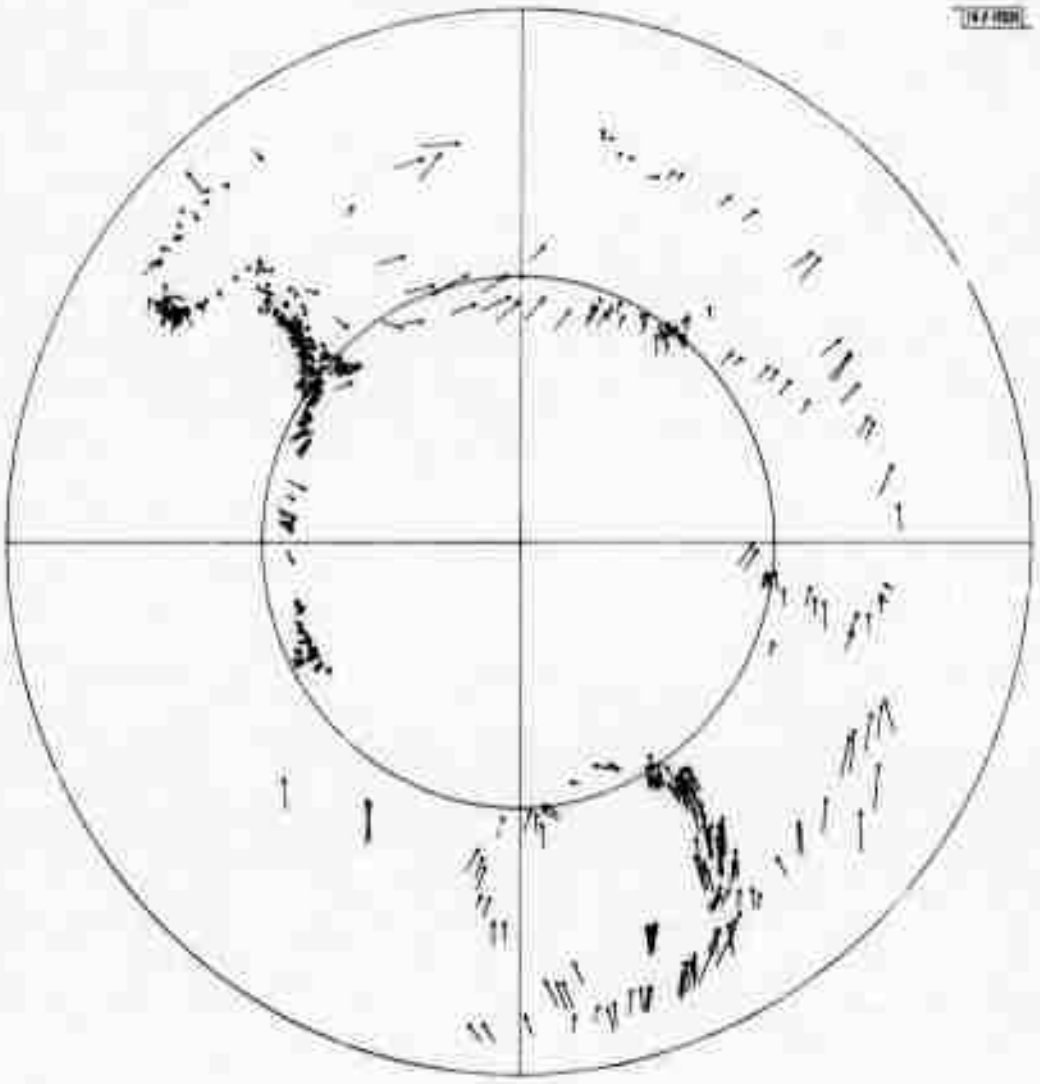

Fig. II-5. Array diagram for LASA. Outer ring has radius of 10 sec/deg. Core data are not considered in this study.

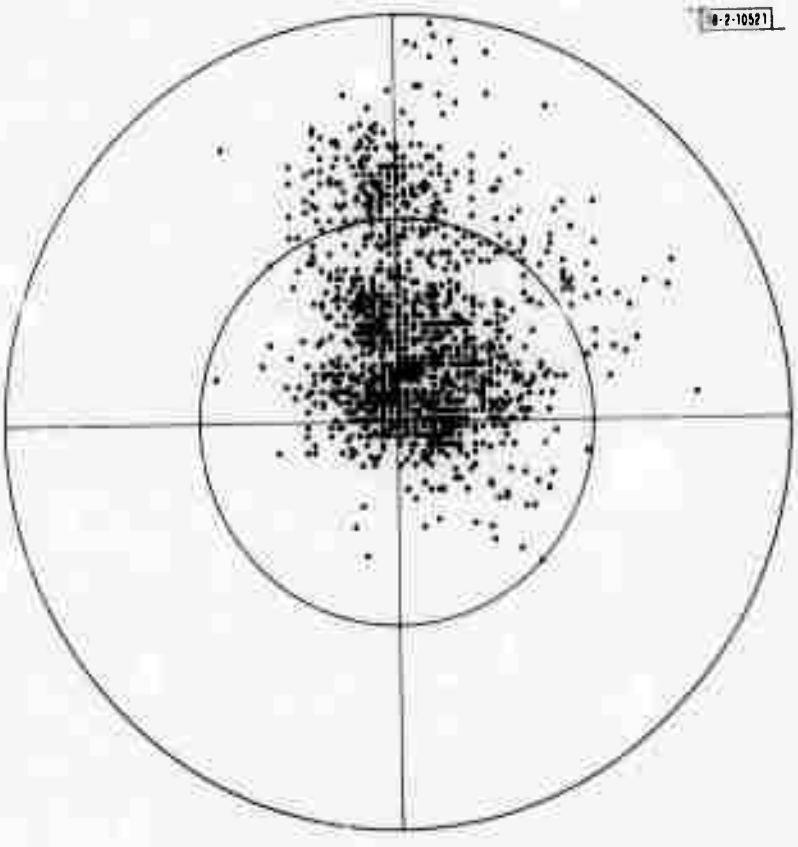

Fig. II-6. Distribution of vectors in Fig. II-5, with meon equivalent to southerly shift of tail of 0.25 sec/deg. Radius of circle is equivalent to 1 sec/deg for purely rodiol anomaly.

III. LASA

A. ANALYSIS OF P-WAVE AZIMUTH AND SLOWNESS ANOMALIES WITHIN SUBARRAYS AT LASA

It is well known that the P-wave signals at LASA, observed during the first 5 sec after the onset time, are subject to severe amplitude and phase fluctuations.[1,2] These fluctuations occur between the various subarrays at LASA, while the variations within a given subarray at LASA are relatively minor. Recent results from NORSAR indicate that these fluctuations are even more severe at that array than at LASA. As yet, there appears to be no adequate explanation concerning a possible structure within the earth which would cause these anomalies. In an attempt to obtain data that would lead to such an explanation, the P-wave azimuth and slowness anomalies were measured within subarrays at LASA. These measurements will now be described.

The high-resolution (HR) wavenumber analysis technique[3] was used to obtain the azimuth and slowness anomalies of the P-waves of 24 events. In addition, the PcP phases of 2 of these events, as well as PKP phases from 5 other events, were included in the analysis. Thus, a total of 31 sets of measurements were made. Each set consisted of 9 measurements made within the subarrays contained in the A-, B-, and C-rings at LASA. Hence, a final total of 279 observations were taken. The data were observed on the short-period vertical seismometers at LASA. The frequency used in the measurement was 0.8 Hz, so that the wavelength of the P-wave is about 10 km, assuming an average compressional velocity of about 8 km/sec.

The results obtained from the HR wavenumber analysis of an event which occurred on 26 February 1967 in Eastern Kazakh are depicted in Figs. III-1(a) through (d) for subarrays B1, B2, B3, and B4, respectively. There were, of course, 8 other measurements made for this event at subarrays A0, C1, C2, C3, and C4, but, for simplicity, only the results for the B-ring are presented. The display of the results in Figs. III-1(a-d) is similar to that given previously.[4] The contours of constant power are displayed, in decibels relative to peak power, and in increments of 2 dB from 0 to 6 dB. Thus, the location of the point labeled 6 dB will provide the horizontal phase velocity and the angle of arrival of the P-wave within the corresponding subarray. As an example, let us consider Fig. III-1(a). The radial line in this figure is drawn at an azimuth of 357° corresponding to the approximate azimuth of the epicenter for this event. The circle in this figure is the locus of wavenumbers corresponding to a velocity of 22 km/sec, which is the nominal horizontal phase velocity that would be expected for the P-wave of this event, as obtained from a set of standard tables for an epicenter-to-LASA distance of about 64°. The wavenumber k (in cycle/km) is related to the velocity v (in km/sec) by the equation $k = f/v$, where f is the frequency and is equal to 0.8 Hz. Thus, if there were no anomaly, the point labeled 6 dB in Fig. III-1(a) would lie at the intersection of the circle and the radial line. However, there is an anomaly and we see that the azimuth of arrival is about 341° and the horizontal phase velocity is about 19 km/sec. Thus, in this case, the P-wave is arriving from a more westerly direction, and with a lower velocity, than expected. On the other hand, the results in Fig. III-1(b) show the P-wave arriving from a more easterly direction, and with a higher velocity, than expected. The results in Figs. III-1(c-d) are truly dramatic when we consider that the aperture of the B-ring at LASA is only 20 km. We should also mention that these results are new and were obtained due to the availability of the LASA data and the HR wavenumber analysis program.

We now wish to define the basic quantities, derived from the HR analysis, which are important in the interpretation of the P-wave anomaly data. These quantities are the azimuth deviation (AZDEV), the slowness correction (SLOCOR), and the relative power expressed in decibels (PDBR). The definition for AZDEV is

$$\text{AZDEV} = \text{MEASURED AZIMUTH} - \text{TRUE AZIMUTH}$$

The true azimuth is assumed to be that obtained from the CGS location for the epicenter of the event. The definition for SLOCOR is taken to be consistent with that given by Niazi.[5] The definition for SLOCOR is

$$\text{SLOCOR} = \frac{\text{SLOWNESS IN MANTLE}}{\text{SLOWNESS AT SURFACE}}$$

where the slowness at the surface is the reciprocal of the horizontal phase velocity obtained as discussed previously from the HR analysis, and

$$\text{SLOWNESS IN MANTLE} = \sin(I_M)/8.2$$

where 8.2 km/sec is the assumed compressional velocity in the mantle, and I_M is the angle of incidence of the P-wave in the mantle. The angle I_M is obtained from Appendix V of Richter,[6] using the appropriate epicenter-to-LASA distance for the event and noting that a crust-to-mantle conversion must be made of the angles tabulated by Richter.

The definition for PDBR is

$$\text{PDBR} = 10 \log_{10} (\text{PMAX}/\text{POWER})$$

where POWER is the power (in $m\mu^2$/Hz) measured using the HR method, and PMAX is the maximum power measured (in $m\mu^2$/Hz) among the 9 subarrays, for each event. It should be stressed that there will be 279 independent measurements for AZDEV, SLOCOR, and PDBR. That is, there are 31 events for which these quantities have been measured within the 9 subarrays comprising the A-, B-, C-rings at LASA.

A graphic illustration of the data for AZDEV and SLOCOR is given in Fig. III-2 for the 26 February 1967 Eastern Kazakh event. In this figure, the diameters and locations of the circles represent the apertures and locations of the various subarrays, and the diameters of the circles are drawn along the true azimuth of the event. The arrows point in the direction of propagation of the wave, and the length of the arrow is proportional to SLOCOR, at the various subarrays. The strikingly large changes in AZDEV and SLOCOR between subarrays which are located within about one wavelength of the P-wave from each other should be noted. This fact is extremely important in the interpretation of the data in terms of a possible structure within the earth which could produce such anomalies.

It is instructive to plot the data for AZDEV, SLOCOR, and PDBR as a function of the true azimuth of the epicenter of the event, as depicted in Figs. III-3(a) through (c), respectively. In these figures, an average curve is drawn which represents the average of the data, for the 9 subarrays, at each azimuth or, equivalently, for each event. It should be noted that SLOCOR and PDBR have been limited to be less than 3.0 and 15.0 dB, respectively. The relatively large values for AZDEV and SLOCOR that occur in Figs. III-3(a) and (b), respectively, are for the core phases which were used in the analysis. This is to be expected, since the angle of incidence

for these phases is small, so that the AZDEV and SLOCOR for them should be large, cf. Niazi.[5] An interesting observation to make at this point is that the average curves for AZDEV and SLOCOR in Figs. III-3(a) and (b), respectively, appear to vary about zero and unity, respectively, with a certain amount of regularity. For example, in Fig. III-3(a) the average curve for AZDEV appears to be negative for azimuths between 150° and 330° and positive otherwise; that is, the average curve in the figure makes a transition between negative and positive values at an azimuth of 330°. In addition, the average curve for SLOCOR in Fig. III-3(b) appears to be less than unity for azimuths between 60° and 240° and is greater than unity otherwise. According to the results of Niazi,[5] this type of behavior is highly suggestive of the effect introduced by a plane-dipping interface across which there is a change in compressional velocity.

We attempted to find the dip and direction of strike of a plane-dipping interface that would provide a best least-squares fit to the AZDEV and SLOCOR data. A velocity ratio of 0.75 was assumed and the procedure given by Niazi[5] was employed to compute the AZDEV and SLOCOR, for an assumed plane interface, for each event. We found that the dip angle of such an interface was 11° and that the azimuth of the strike direction was 60°. This agrees quite well with the average dip angle and direction of strike of the corrugated surface proposed by Greenfield and Sheppard[7] to explain the P-wave time anomaly data at LASA. Additional work has been done to determine a structure within the earth to explain the P-wave anomaly data, and the results will be presented in a forthcoming publication.[8] A brief discussion of some of these results will now be presented.

A model has been proposed to explain the cause of the P-wave anomaly data, in which the crust and upper mantle structure under LASA can be characterized as a random, or Chernov-type, medium.[9] A statistical analysis of the data for the phase and amplitude fluctuations of the P-wave has been made which, along with some theoretical results due to Chernov,[9] was used to determine the properties of the random medium. We found that the correlation distance of the random medium is 12 km and that the standard deviation of the index of refraction is 1.9 percent. These random inhomogeneities exist in the crust and upper mantle of the earth down to a depth of about 136 km.

It is important to point out that a single, or multiple, corrugated interface cannot be used to explain the source of the P-wave anomalies because such a structure would lead, according to Chernov's theory, to a high correlation between the amplitude and phase fluctuations, and to a value of amplitude-relative-to-phase fluctuation power ratio close to zero. These conditions are not found to be true in the statistical analysis of the data. Hence, a model involving a single, or multiple, corrugated interface is inadequate to explain the observations. It should be mentioned that a similar approach to this problem has been considered recently by Aki.[10]

J. Capon

B. CRUSTAL SCATTERED S-WAVES UNDER LASA

The nature of the laterally heterogeneous structure of the crust and upper mantle beneath LASA that causes the first-order time, amplitude, and waveform anomalies associated with short-period teleseismic P-waves is being investigated by observing the scattered S-waves from emerging P-waves. Such a study is presently confined to data obtained from the 3-component, short-period, digitally recorded seismograph at subarray D2 (see Ref. 11). [The data are recorded on all standard high-rate format LASA tapes in record words 19 (Vertical), 40 (North), and 61 (East) after 26 June 1968.]

Previous investigators[12-14] have used only the short-period P-wave motion recorded on the vertical instruments. To obtain a model based on such data, one must know the first-order P-wave velocity structure beneath the array. Observing the total motion has several distinct advantages. The S-velocity as a function of depth is not as well known as the P-velocity function; however, the location of a source of S will be more accurate when determined by the first-order S-P time measurement than when derived by travel-time residuals alone. Further, since S and P are essentially normally polarized, a simple coordinate rotation separates them. The relative amplitude and frequency content of the two waves provide information on the impedance contrast and sharpness of any boundary acting as an apparent source. The same functions determined over various distances and azimuths determine the strike and dip of the converting boundary. Moreover, the shape of a converted S-wave will essentially be the same as that of the exciting P-wave, thus the observed differences between the S- and P-waveforms are constrained to be the result of a process occurring between the apparent source and the receiver. Consequently, that part of the seismogram due to crustal reverberation should be separable from the source component.

Data from a typical event are shown in Fig. III-4. The raw data in the first three traces show P and pP from an event located in the North Atlantic at a distance of 68° and an azimuth of 62°. The bottom two traces show the rotated components containing SV and SH motion. The P-component is approximately the same as the V-component. At a lag of 1 to 2 sec behind P and pP is an S-wave arrival. Such an offset constrains the apparent source of S to lie at a depth of about 3 km, the boundary between the sediments and basement at LASA.[15] The fact that the S-wave from pP has not been completely polarized at the same angle as the S-wave from P indicates that P and pP are emerging from different azimuths. Relative particle motion on the SV and SH components of the S-wave due to pP determine that the apparent azimuth of pP is about 20°N of the apparent azimuth of P. The frequency content and amplitude of the S-waves (0.35 of the P-wave amplitude) are consistent with a tectonic–sedimentary boundary that is planar, sharp, and has a high impedance contrast (refraction studies[5] show a velocity contrast of about 2 for this boundary; however, no conclusion on the sharpness or uniformity of the boundary can be obtained from refraction data). The strike and dip of this boundary can be determined by observing the S-waves it scatters for different azimuths and incidence angles. Figure III-5 shows records for 6 events that cover all azimuths. The S-waves from the sedimentary basement vanish for the event coming from an azimuth of 314° and a distance of 89°, indicating normal incidence of the P-wave at the boundary. An 89° distant event emerges at about 15° from the normal in a 6-km/sec medium; thus, the boundary dips to the southeast beneath subarray D2. Other events with approximately the same distance and azimuths show the same extinction of the S-wave, leading to the same boundary configuration. Such a geometry is in agreement with the general trend determined by a recent refraction survey.[16]

Several other interesting observations can be made from these data. Figure III-6 shows the event from Az = 150° and Δ = 58° with the SV-component shifted 1.5 sec to the left so that the S-wave scattered from the sedimentary boundary lies directly beneath the exciting P-wave. P, pP, and sP all clearly show a corresponding scattered S. The LASA bulletin, based on just vertical recordings at the array, listed the sP as pP. (WWSSN data agree with the 3-component data.) The pP phase was chosen on the basis of (1) a consistent sP time, and (2) a corresponding

scattered S-wave for both pP and sP with appropriate amplitude ratios (the S from pP should have the same amplitude ratio to pP as the S-to-P amplitude ratio, while the S from sP should have a somewhat larger ratio since sP is incident at a larger angle). P_r marks the arrival whose time and corresponding lack of a basement S-wave indicate that it is probably a crustal reverberation rather than a part of the incoming source waveform. $_pS_M$ marks the S-wave that was scattered at the Moho. It comes in about 8 sec after P. The same arrival can be confirmed on the various traces in Fig. III-5 by examining the S-motion near 8 sec after P (or PcP, or any primary P motion). Such a time delay indicates a depth between 60 and 70 km for the Moho beneath D2. Similar consistent effects can be seen from the other events in Fig. III-6.

In summary, a brief analysis of 3-component seismic motion has shown promise in helping to delineate local structure and in separating the effects of the structure from the incoming source waveform. As the structure probably varies considerably over the array, knowledge of horizontal motion at the other subarrays would prove extremely valuable in tuning the array so as to achieve its maximum gain. As only a single station experiment, knowledge of the S-waves scattered at major discontinuities enhances the azimuth determination and phase identification capabilities of the array.

T. Landers

C. LASA SHORT-PERIOD INSTRUMENT RESPONSES

To determine time-domain source characteristics from a seismogram, it is often necessary to remove the effect of the seismometer and examine the motion of the ground at the seismometer site. For example, Frasier[17] was able to show that pP phases from a number of NTS explosions were observable at NORSAR by removing the theoretical impulse response from the data. In this SATS, Filson and Frasier have been able to remove the responses from a number of WWSSN records and determine the direction of propagation of rupture of a central Asian earthquake.

At LASA, differences in signal characteristics are always observed from site to site, even within a subarray. Some of these differences are probably caused by scattering of the incoming seismic signal, while the remainder are caused by convolution of the signal with different displacement impulse responses of the instruments. To be able to separate these two effects and obtain a more truthful picture of the incoming signal, it is obviously necessary to be able to remove the individual responses from the data. Since the response of each instrument will probably change slightly with time, an up-to-date measurement of each response will be required whenever the data need to be deconvolved.

In 1966,[18] we developed a broadband calibration system for the short-period instruments which has never been used to obtain the response of a single instrument to an impulse in displacement. As shown here, this is done easily and can be done at any time to obtain the present impulse responses of all the short-period seismometers.

The calibration consists of applying a known pseudo-random sequence of voltage steps to the calibration coil of the seismometer and measuring the simultaneous seismometer output. If the rise time for the development of the magnetic field produced by the calibration coil is short compared with 0.05 sec (the sampling rate of the data), a step in voltage applied to the coil is equivalent to a step in acceleration applied to the seismometer. In other words, if the known input voltage to the calibration coil is V(t), and the measured output of the seismometer is S(t), the

relationship between S(t) and V(t) is

$$S(t) = \int_{-\infty}^{\infty} V(\tau)\, F(t-\tau)\, d\tau \qquad \text{(III-1)}$$

where F(t) is the response of the seismometer to an impulse in ground acceleration. The first derivative of F – dF/dt – is the seismometer response to an impulse in ground velocity, while the second derivative of F – d^2F/dt^2 – is the seismometer response to an impulse in ground displacement. Therefore, to obtain d^2F/dt^2 knowing V(t) and S(t), it is only necessary to solve Eq. (III-1) for F(t) and to differentiate it twice.

A calibration of subarray B3 was made on 24 January 1972. The pseudo-random voltage input was applied simultaneously to all the B3 short-period instruments for about 5 minutes beginning at 21:07:00, the input voltage and seismometer outputs being recorded on tape. Figure III-7(a-c) is a sample of the voltage input and output recorded by seismometer 1. A least-squares approximation to F(t) was obtained for each of the 16 instruments and the subarray sum using Levinson's method[19] and solving the equations

$$\sum_{n=0}^{M} F_n \varphi_{VV}(n-\tau) = \varphi_{SV}(\tau) \quad \text{for } \tau = 0, 1, \ldots, M \qquad \text{(III-2)}$$

where

$$\varphi_{VV}(\tau) = \frac{\sum_{0}^{N-\tau} V_{t+\tau} V_t}{N-\tau}$$

$$\varphi_{SV}(\tau) = \frac{\sum_{0}^{N-\tau} S_{t+\tau} V_t}{N-\tau}$$

$$N = 511$$

$$M = 49 \quad .$$

Some of the impulse responses F(t) are shown in Fig. III-8, while the result of convolving the F(t) obtained for seismometer 1 with the input voltage is shown in Fig. III-7(a-c). In no case was the normalized rms difference between the measured output and the result of convolving the computed response with the input greater than 0.97.

Differentiation of each of the 17 acceleration impulse responses was carried out in the frequency domain using the following relations:

$$f(\omega) = \int_{-\infty}^{\infty} F(t)\, e^{-j\omega t}\, dt$$

$$F(t) = \frac{1}{2\pi} \int_{-\infty}^{\infty} f(\omega)\, e^{j\omega t}\, d\omega$$

$$\frac{d[F(t)]}{dt} = \frac{1}{2\pi} \int_{-\infty}^{\infty} j\omega f(\omega)\, e^{j\omega t}\, d\omega \quad . \qquad \text{(III-3)}$$

The velocity and displacement impulse responses of some of these instruments are shown in Fig. III-8. For seismometer 1, the amplitude and phase spectra for all three impulse responses are shown in Fig. III-9(a-d).

From Fig. III-8, it can be seen easily that the responses of the different seismometers are more similar at high than at low frequencies: the differences in the acceleration impulse responses are more obvious than those in displacement impulse responses. The major differences appear to be in gain: all these responses have been drawn to be the same size; the true relative amplitudes are written by the side of each response. The amplifier at the output of each seismometer is most sensitive to low-frequency changes. It would seem, therefore, that the easiest way to check the adjustment of amplifier gain and seismometer damping would be to obtain $F(t)$, the acceleration impulse response, by solving Eq. (III-21) for each calibration.

Since it is now possible to perform a similar calibration of the long-period instruments,[20] I recommend that a full calibration be made of all the seismometers at LASA once a month and that the results be available on tape for anyone requiring to know the responses for that month.

A. Ziolkowski

REFERENCES

1. J. Capon, R. J. Greenfield, R. J. Kolker and R. T. Lacoss, "Short-Period Signal Processing Results for the Large Aperture Seismic Array," Geophysics 33, 452-472 (1968), DDC AD-674830.

2. H. Mack, "Nature of Short-Period P-Wave Signal Variations at LASA," J. Geophys. Res. 74, 3161-3170 (1969).

3. J. Capon, "High-Resolution Frequency-Wavenumber Spectrum Analysis," Proc. IEEE 57, 1408-1418 (1969), DDC AD-696880.

4. _____, "Analysis of Rayleigh-Wave Multipath Propagation at LASA," Bull. Seismol. Soc. Am. 60, 1701-1731 (1970), DDC AD-716084.

5. M. Niazi, "Corrections to Apparent Azimuths and Travel-Time Gradients for a Dipping Mohorovicic Discontinuity," Bull. Seismol. Soc. Am. 56, 491-509 (1966).

6. C. F. Richter, Elementary Seismology (W. H. Freeman and Co., San Francisco, 1958).

7. R. J. Greenfield and R. M. Sheppard, "The Moho Depth Variations under the LASA and Their Effect on dT/dΔ Measurements," Bull. Seismol. Soc. Am. 59, 409-420 (1969).

8. J. Capon, "Characterization of Crust and Upper Mantle Structure Under LASA as a Random Medium," in preparation.

9. L. A. Chernov, Wave Propagation in a Random Medium (McGraw-Hill, New York, 1960).

10. K. Aki, "Scattering of P-Waves Under the Montana LASA," to be published.

11. Montana LASA 4th Quarterly Report, IBM (May 1969), pp. 5-11, DDC AD-855745.

12. R. J. Greenfield and R. M. Sheppard, "The Moho Depth Variations under the LASA and Their Effect on dT/dΔ Measurements," Bull. Seismol. Soc. Am. 59, 409-420 (1969).

13. K. L. Larner, "Near Receiver Scattering of Teleseismic Body Waves in Layered Crust-Mantle Models Having Irregular Interfaces," Ph. D. Thesis, Department of Earth and Planetary Sciences, M.I.T. (February 1970).

14. H. M. Iyer, A. R. Jackson, J. H. Healy and T. E. Landers, "LASA Anomalies and Their Relations to Crust and Upper-Mantle Structure," U.S. Geological Survey Open File Report (1969).

15. C. A. Borchert and J. C. Roller, "Preliminary Interpretation of a Seismic-Refraction Profile Across the Large Aperture Seismic Array, Montana," Technical Letter No. 2, U.S. Geological Survey, NCER, Menlo Park, California (1967).

16. J. F. Gibbs, "A Model for the Crust of the Earth Under LASA from Crossed Seismic Refraction Profiles," U.S. Geological Survey, NCER, Menlo Park, California (1971).

17. Seismic Discrimination SATS, Lincoln Laboratory, M.I.T. (31 December 1971), pp. 1-3, DDC AD-737092.

18. Ibid. (30 June 1966), pp. 21-24, DDC AD-637308.

19. N. Levinson, "The Wiener R.M.S. Error Criterion in Filter Design and Prediction," Appendix B of N. Wiener, Extrapolation, Interpolation and Smoothing of Stationary Time Series (Wiley, New York, 1949).

20. R. E. Watkins, "Seismograph Calibrations Using Pseudo-Random Binary Sequences," Philco-Ford Report No. T/R 2056-72-19 to the Advanced Research Projects Agency (19 April 1972).

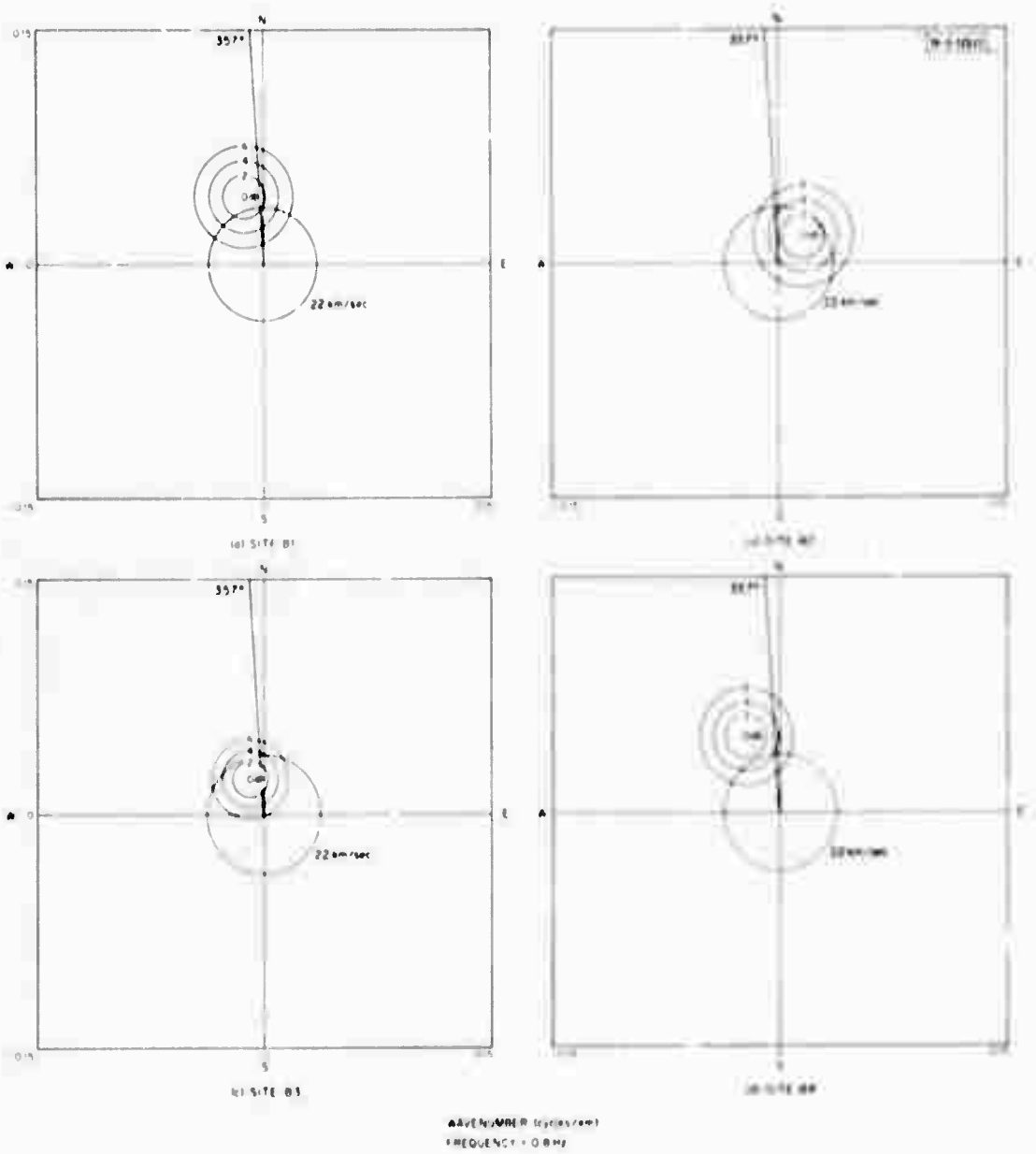

Fig. III-1(a-d). Analysis of P-wave azimuth and slowness anomalies within B-ring at LASA for 26 February 1967 Eastern Kazakh event.

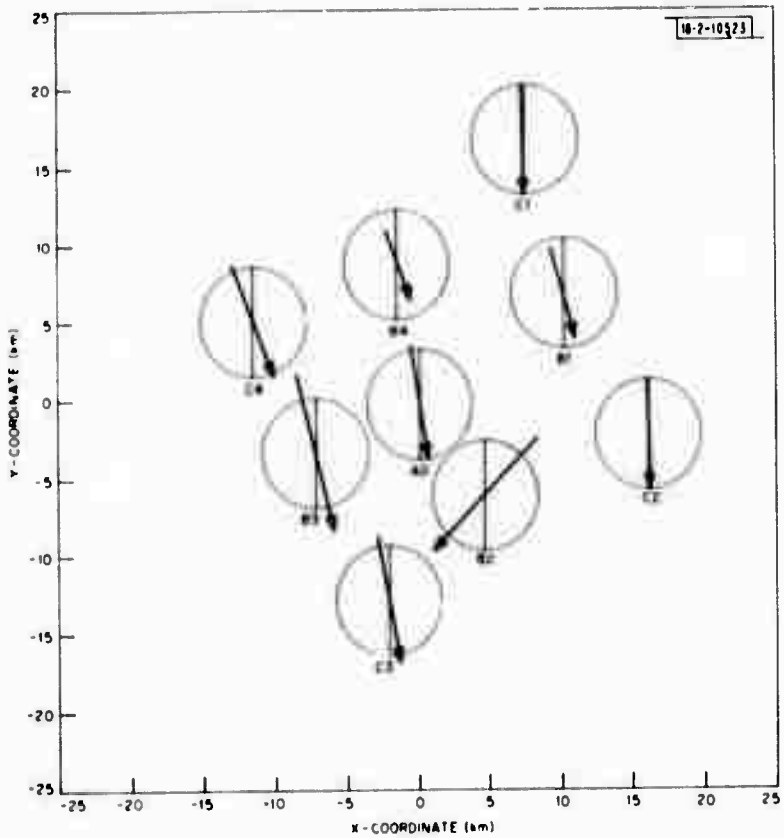

Fig. III-2. Graphic display of P-wave azimuth deviations and slowness corrections within C-ring at LASA for 26 February 1967 Eastern Kazakh event.

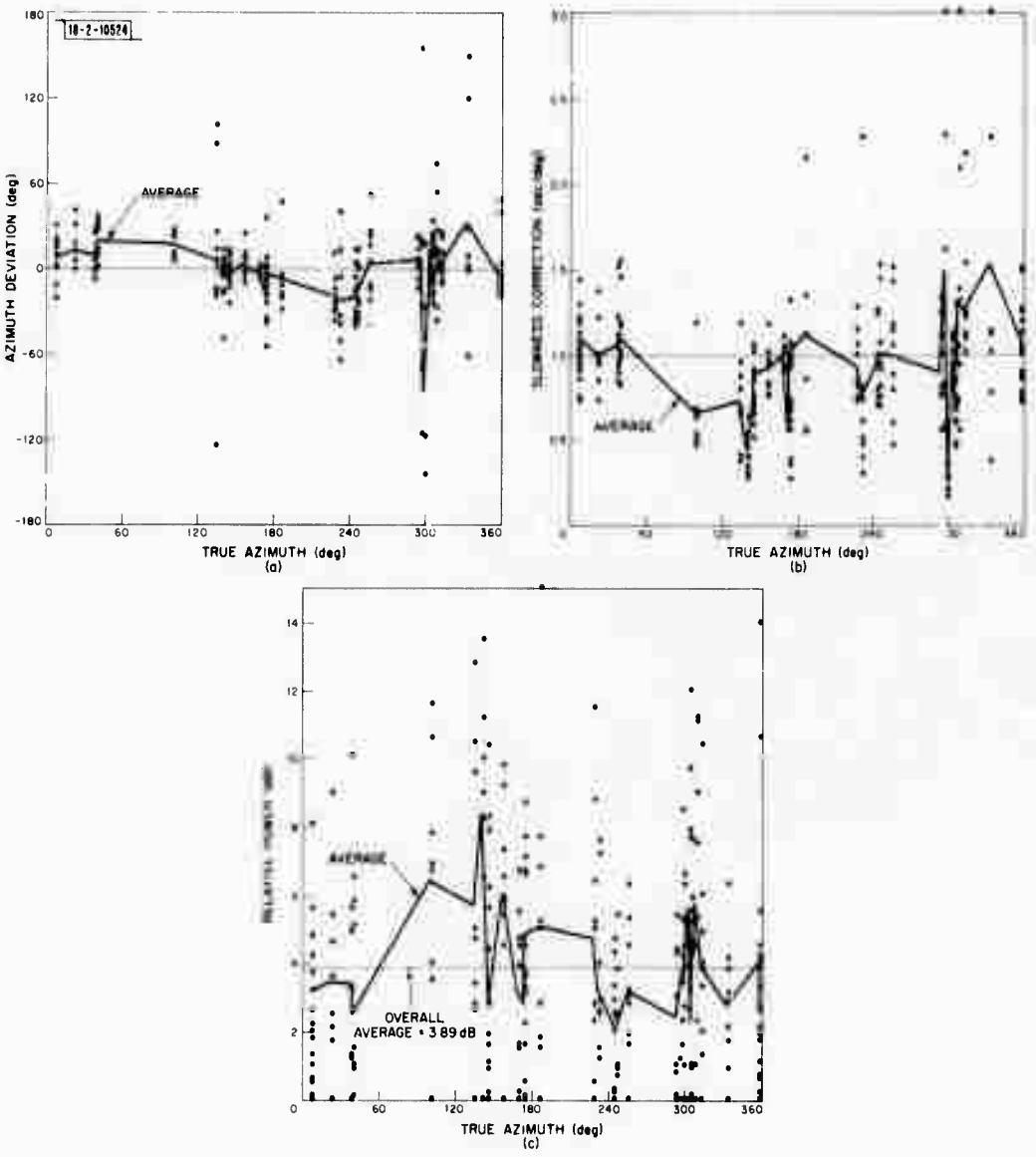

Fig. III-3(a-c). Azimuth deviation, slowness correction and relative power vs true azimuth for P-wave signals of 31 events measured within C-ring at LASA.

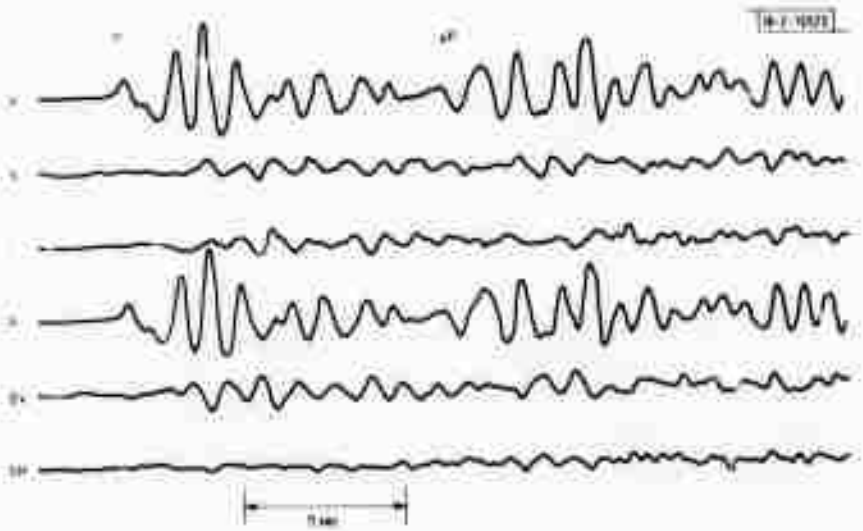

Fig. III-4. (V'ertical, (N)arth, and (E)ast, and rotated SV and SH short-period seismograms re:orded at subarray D2 showing P and PcP phases and corresponding crustal scatter:d S-waves from North Atlantic earthquake.

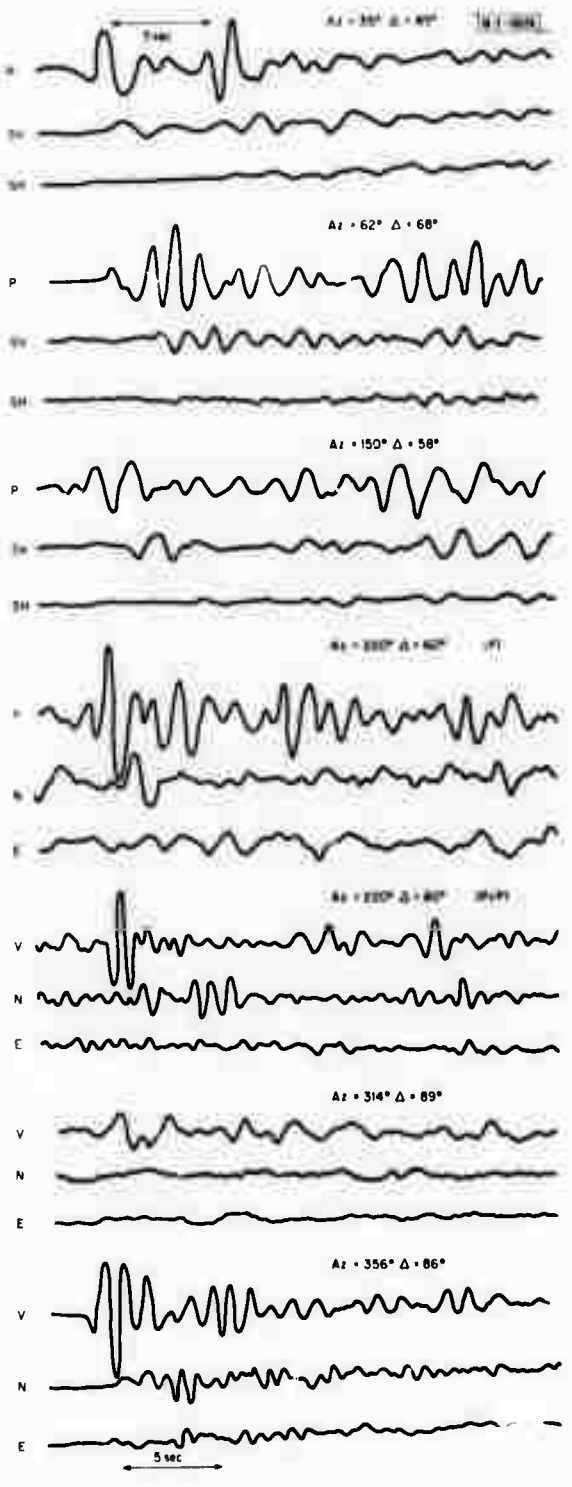

Fig. III-5. 3-component dota from six events from vorious ozimuths and distonces. Note extinction of S-wove scottered from sedimentory section – tectonic bosement boundory for event from Az = 314° and Δ = 89°.

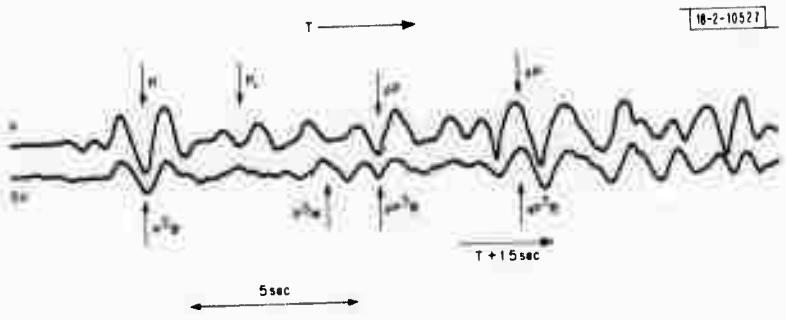

Fig. III-6. P-motion ond shifted S-motion from event from Az = 150° ond Δ = 58° showing arrivols of P, pP, ond sP, and their corresponding basement boundary scattered S-waves. P_r is crustol reverberation, pS_M is P scattered S-wave from Moho.

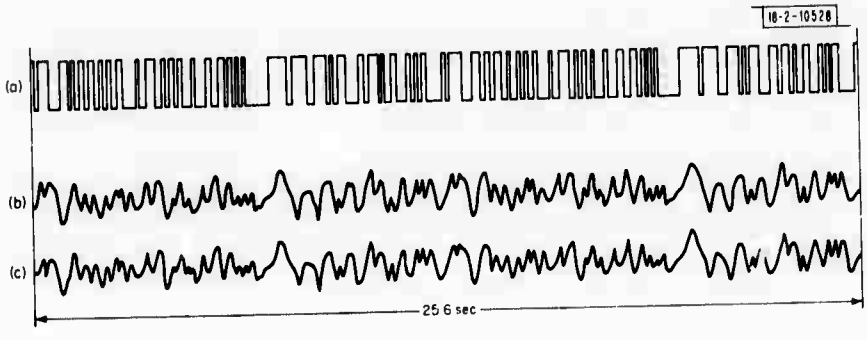

Fig. III-7. (o) Pseudo-rondom voltage applied to colibration coil V(t); (b) observed output ot seismometer 1; and (c) computed output, convolution of F(t) with V(t).

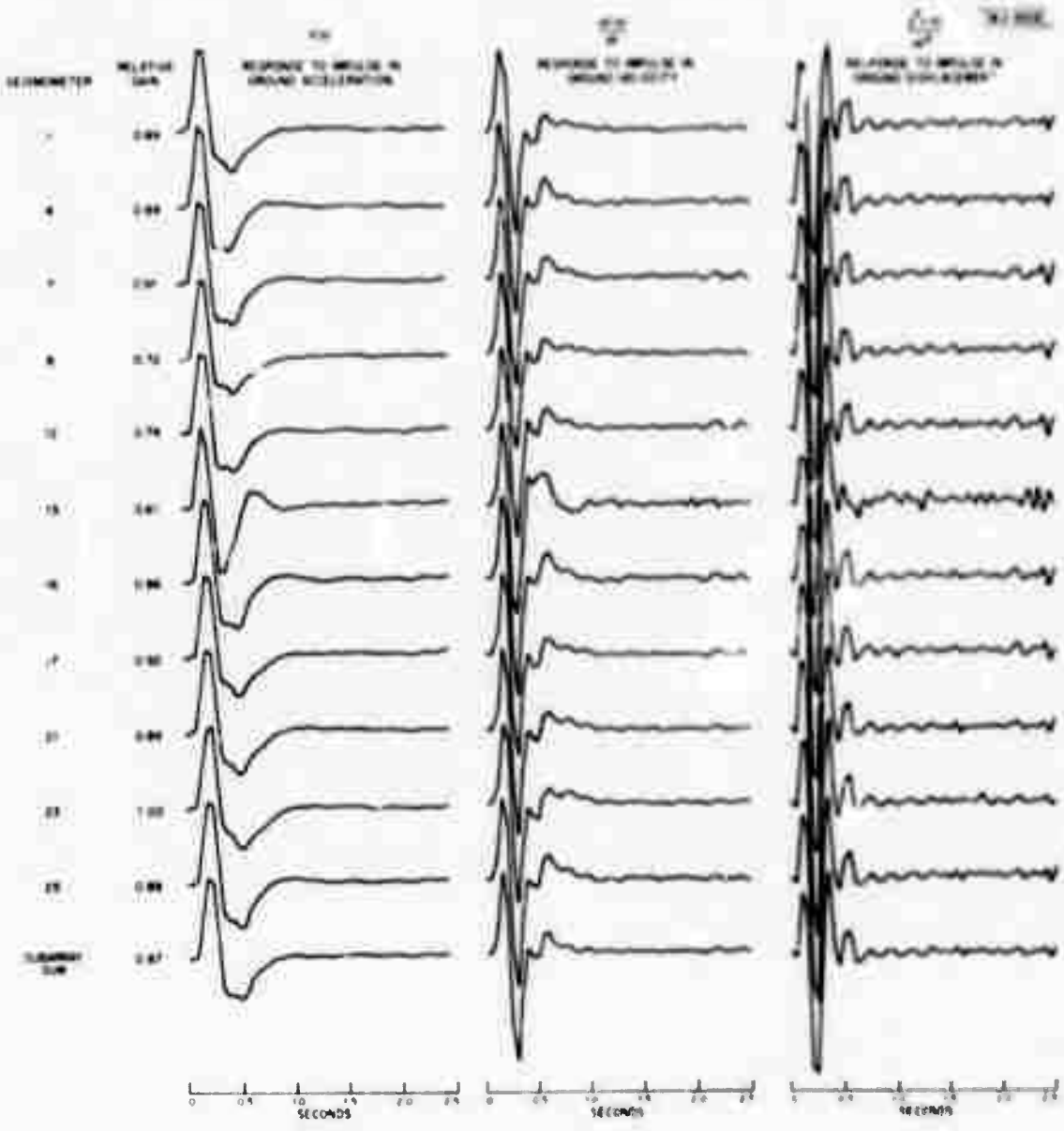

Fig. III-8. Impulse responses of some short-period seismometers at B3 on 24 January 1972.

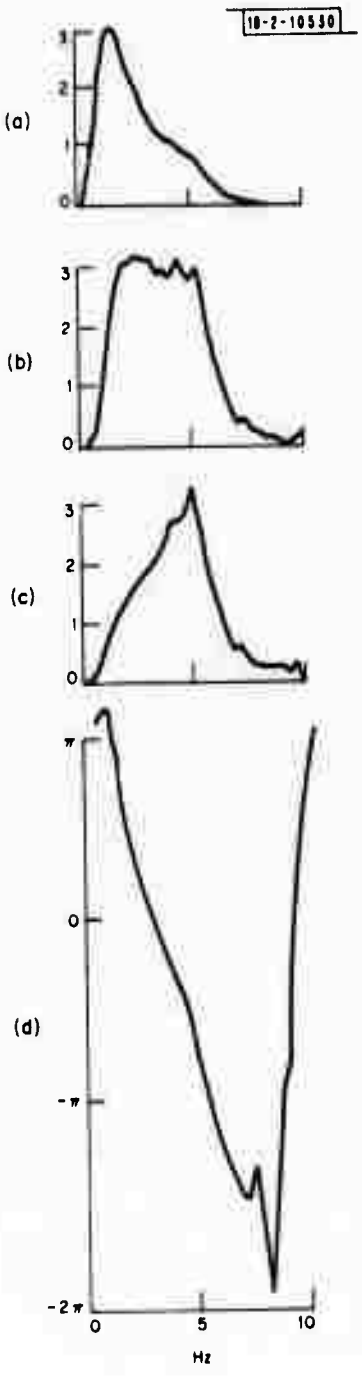

Fig. III-9. Amplitude and phase spectra for B3 seismometer 1 (horizontal scale is frequency in Heriz). (a) Amplitude spectrum of F(t), acceleration impulse response; (b) amplitude spectrum of $d[F(t)]/dt$, velocity impulse response; (c) amplitude spectrum of $d^2[F(t)]/dt^2$, displacement impulse response; and (d) phase spectrum of displacement impulse response. Phase spectra for velocity and acceleration responses have same shape but differ by $-\pi/2$ and $-\pi$, respectively. All vertical and horizontal scales are linear.

IV. EVALUATION OF NORSAR

A. SHORT-PERIOD AMPLITUDE VARIATIONS AND COHERENCY AT NORSAR

The amplitudes of steered short-period NORSAR subarrays have been measured for 58 events distributed over 16 small regions. Figure IV-1 shows the location of the regions in inverse velocity space relative to NORSAR. The amplitudes measured were maximum peak-to-peak excursions of 0.9- to 3.0-Hz filtered subarray beams generated by the Event Processor at NORSAR. Only events with large signal-to-noise ratios (SNR) were used in order to avoid errors introduced by background noise. The amplitude of each event was normalized by the geometric mean of the amplitudes of all the subarrays, and the average within each region was calculated. The number of events within each region ranged from 2 to 6. The standard deviation of the anomalies within each region was also calculated for each subarray. The same calculations were done for all 58 events together and for the 16 average normalized amplitudes from the different regions. The results for four regions and for the global data are shown in Table IV-1.

Table IV-1 is only part of the data, but it is representative and several observations can be made. For a fixed region, the amplitude variations are large and generally quite repeatable for different events. However, the amplitude at a subarray depends strongly upon the region – an amplitude good for one region can be quite poor for another. This is verified by the global results which display less variation of average gain between subarrays and show larger standard deviations relative to the average gain.

The amplitude measurements were made after new NORSAR station corrections were introduced in early February 1972. It is worth noting that the observed beam amplitude, filtered 0.9 to 3.0 Hz, was on average equal to the average subarray amplitude, which is about as good as could be expected. An unfiltered beam was an average 3 to 4 dB larger than the filtered beam, but the SNR was worst for the unfiltered data. Also, one would expect the signal loss from filtering to be less for smaller events as their higher frequency content is more centrally in the passband of the filter.

The short-period amplitude scatter at NORSAR is larger than that at LASA, but this does not mean that LASA is relatively free of scatter and that NORSAR has an order-of-magnitude more scatter. The true situation is indicated by the data on Figs. IV-2(a) and (b). For each subarray at NORSAR, the minimum, maximum, and median normalized gain over all 16 regions was obtained and is plotted in Fig. IV-2(a); 13 of these regions are third zone to LASA. The LASA normalized gains for a single instrument in each subarray were available for these regions.[1] Minimum, maximum, and medians were calculated and are shown in Fig. IV-2(b). This comparison of LASA and NORSAR scatter is somewhat qualitative and is between single instruments and subarrays, but the larger scatter at NORSAR is quite evident.

It is worth noting that even subarrays which show somewhat low amplitudes on average can be quite significant in particular cases. Note NORSAR subarrays 4B and 6C in particular. On average, they tend to have somewhat low amplitudes. However, the maximum gains of 1.9 and 2.8 shown on Fig. IV-2(a) are for presumed explosions at the Eastern Kazakh test site. For those events, site 6C is the best site in NORSAR, and 4B is one of the better sites.

TABLE IV-1

AMPLITUDE VARIATIONS ACROSS NORSAR

Subarray	Taiwan (3 events)		Kuriles (5 events)		Off Coast of Mexico (3 events)		Greece (5 events)		Global (58 events)		Global Regions (16 regions)	
	Gain	Std. Dev.	Gain	Std. Dev.	Gain	Std. Dev.	Gain	Std. Dev.	Gain	Std. Dev.	Gain	Std. Dev.
1C	1.72	0.28	1.65	0.29	0.63	0.11	0.63	0.10	1.45	0.78	1.27	0.63
2C	1.08	0.15	1.20	0.24	0.63	0.19	0.85	0.12	1.24	0.52	1.14	0.44
1B	0.58	0.03	0.70	0.07	1.58	0.06	1.41	0.49	1.10	0.40	1.10	0.35
5B	0.50	0.09	0.64	0.03	1.22	0.19	1.03	0.48	0.80	0.33	0.80	0.26
8C	0.78	0.15	0.87	0.13	0.84	0.04	0.95	0.38	0.91	0.30	0.90	0.21
9C	0.70	0.03	1.41	0.21	0.78	0.07	1.05	0.32	0.94	0.51	0.91	0.46
12C	0.70	0.15	0.71	0.08	1.27	0.18	1.16	0.34	1.00	0.40	0.99	0.38
6B	0.93	0.21	1.39	0.30	1.54	0.12	1.10	0.47	1.07	0.47	1.08	0.45
1A	0.90	0.12	1.00	0.18	1.84	0.16	2.13	0.16	1.24	0.45	1.19	0.41
3B	0.75	0.02	1.61	0.11	0.92	0.09	3.08	1.20	1.25	0.82	1.23	0.62
5C	2.38	0.28	2.54	0.56	1.51	0.03	0.81	0.10	1.66	0.68	1.63	0.55
3C	1.65	0.15	1.54	0.33	0.88	0.18	0.52	0.11	1.53	0.70	1.53	0.66
4C	2.28	0.29	1.23	0.87	1.29	0.05	0.86	0.09	1.51	0.55	1.50	0.42
2B	1.45	0.06	2.50	0.27	1.46	0.22	1.32	0.24	1.39	0.59	1.35	0.52
11C	1.41	0.06	0.61	0.10	0.72	0.20	0.74	0.10	0.94	0.43	0.91	0.36
10C	0.60	0.17	1.35	0.29	0.64	0.11	0.93	0.23	0.94	0.38	0.92	0.26
13C	2.38	0.27	0.64	0.19	0.77	0.06	0.68	0.02	1.21	0.69	1.17	0.59
14C	0.64	0.06	0.54	0.05	0.86	0.05	0.62	0.11	0.70	0.22	0.73	0.21
7B	1.10	0.05	0.61	0.12	0.78	0.06	2.02	0.50	1.19	0.53	1.10	0.44
4B	0.69	0.06	0.95	0.25	1.43	0.18	1.05	0.27	0.87	0.31	0.87	0.34
6C	0.71	0.16	0.85	0.25	1.66	0.06	1.12	0.53	0.89	0.52	0.97	0.57
7C	1.11	0.11	1.00	0.11	0.54	0.06	1.17	0.37	0.90	0.30	0.90	0.20

In addition to the amplitude study discussed above, we have investigated the variation in waveform between individual NORSAR subarrays by comparing the coherency of individual subarray beams with respect to the full array beam. Two approaches were taken within the coherency study: a small-population study, where zero-lag coherencies were computed by aligning the subarray beams and the full array beam by eye using the analysis console; and a large-population study, where coherencies computed by the NORSAR Event Processor were used.

In the small-population study, the zero-lag coherency ρ_j was computed using the short-period P-wave data from 13 events at teleseismic distances. Once the j^{th} subarray beam x_{ij} and the full array beam y_i have been aligned by eye, ρ_j is defined as

$$\rho_j = \frac{\sum_{i=0}^{l} x_{ij} y_i}{\left(\sum_{i=0}^{l} x_{ij}^2 \sum_{i=0}^{l} y_i^2 \right)^{1/2}}$$

where l is equivalent to 5 sec of data. The average ρ_j at the j^{th} subarray was computed over the 13 events and the results are plotted as a solid line in Fig. IV-3 where it is seen that the average value of ρ_j is fairly stable, fluctuating between 0.75 and 0.85. Thus, in spite of the fact that certain subarray beams of certain events may demonstrate a remarkably low coherence ($\rho < 0.3$) with respect to the full array beam, based on this data set, the subarray beams are about equally coherent on the average.

In the large-population study, use was made of the NORSAR event tape covering the period 15 February to 15 March 1971. Among other parameters automatically measured from the short-period waveforms by the Event Processor are the coherencies between subarray beams and a full array beam. These are maximum coherencies on which the delays used in machine locations are based. Although they are not directly comparable to the ρ_j of the previous experiment, they do represent a large body of data concerning the coherency of short-period waveforms on the subarray beams. To elaborate, many of the events on the event tape are small with small SNRs; thus, we should expect a lower average coherency at a given subarray if the average is based on a large, comprehensive population. We see that this is the case in Fig. IV-3 where plotted as a dashed line are the average coherencies of the individual subarray beams with respect to the full array beam, the average being taken over 406 processed "events" occurring during the 1-month time period. Again we must conclude, with one exception, that on the average the subarray coherencies are quite stable. The one exception is so remarkably low compared with its neighbors, we might suspect it was deleted from the coherency measurements for some extraneous reason during this period. It does not appear as anomalous in the small-population study.

No geographic restriction was placed on the 406 events used above. When we restricted the events of the large population to 0° to 120° azimuth from NORSAR, the average coherency results remained essentially unchanged. Thus, to summarize the main point, although certain subarrays may be poorly correlated with the beams for a given event, they all appear to yield roughly equivalent correlation values on the average.

R. T. Lacoss
J. Filson

TABLE IV-2

EVENTS USED IN NORSAR STUDY

Date	Time (GMT)	Latitude (°N)	Longitude (°E)	Depth (km)	Distance to NORSAR (deg)	Period (sec)	Magnitude m_b	
							NORSAR	NOAA
3 January 1970	06:54:49	41.8	43.2	68	27.4	0.8	4.7	5.1
3 January 1970	16:35:48	32.6	48.8	32	37.4	0.4	4.6	5.0
8 January 1970	07:31:33	37.9	72.5	108	44.5	0.5	4.3	4.9
10 January 1970	04:50:29	38.1	73.7	146	44.9	0.7	4.6	5.0
19 January 1970	00:31:53	41.1	69.3	43	40.5	0.9	4.6	5.0
29 January 1970	07:02:58	49.8	78.2	0	38.7	0.6	5.0	5.6
23 February 1970	22:37:37	36.0	70.4	137	45.0	0.7	4.5	5.0
24 February 1970	02:07:37	30.6	103.0	33	65.4	0.8	5.5	5.9
12 March 1970	18:09:54	24.2	102.8	33	70.7	1.0	4.6	5.2
15 March 1970	18:34:09	36.4	70.9	220	44.9	0.6	4.1	4.9
3 April 1970	20:53:55	37.1	54.6	43	36.4	1.2	4.9	5.2
21 July 1970	01:18:05	36.5	70.5	210	44.6	1.0	5.1	5.2
21 July 1970	03:02:57	50.0	77.8	0	38.4	0.6	4.9	5.4
21 July 1970	08:59:52	38.6	73.4	120	44.5	1.0	4.2	4.6
24 July 1970	03:56:57	49.8	78.2	0	38.7	0.4	4.7	5.3
28 July 1970	06:33:35	36.0	68.3	60	43.9	1.0	4.5	5.0
30 July 1970	00:52:20	37.8	55.9	19	36.4	0.6	5.3	5.7
8 August 1970	11:46:31	44.3	81.2	33	44.0	0.8	4.0	4.7
25 May 1971	04:02:58	49.8	78.2	0	38.7	0.4	5.0	5.2

B. EVALUATION OF SHORT-PERIOD NORSAR DATA

Body wave magnitudes of available central Asian events in 1970, recorded by the interim NORSAR array, have been studied as part of the NORSAR evaluation program. The interim array consisted of single sensors from most of the NORSAR subarrays, and the data were digitized at 10 Hz. A single presumed explosion in May 1971 is also included. This event was recorded by the full NORSAR of 132 seismometers, with a sampling rate of 20 Hz. These full-array data are now becoming available and will provide a more complete, better quality data base for the evaluation of NORSAR.

A list of the events is given in Table IV-2, and the event locations are displayed in the map of Fig. IV-4. Four of the events are presumed Soviet explosions from the Soviet test site near Semipalatinsk in Eastern Kazakh.

Array beams were formed for each event by aligning the first motions by eye. The observed peak-to-peak digital amplitude of each beam was corrected for the NORSAR recording system and converted to magnitude. Both the computed and NOAA magnitudes for each event are given in Table IV-2.

In Fig. IV-5, the difference between NOAA and NORSAR magnitudes is shown as a function of epicentral distance from NORSAR. Figure IV-6 contains the same magnitude differences plotted vs the period of P-wave beam. Although the data base is too small for statistical analysis, the impression is that NORSAR magnitudes are about 0.5 unit lower than NOAA magnitudes, independent of the period and distance of the central Asian event. This seems to be verified by event detections from all azimuths published in the weekly NORSAR Seismic Event Summary.

On the other hand, Lacoss[2] has shown that LASA body wave magnitudes are equal or slightly larger than NOAA magnitudes, on the average. Such NORSAR and LASA magnitude differences can be partially accounted for by station corrections. A P-wave arriving at the surface has an energy density flux which is proportional to $\rho\alpha\dot{u}^2(t)$, where ρ and α are the density and compressional velocity, respectively, of the surface rock, and $\dot{u}(t)$ is the ground velocity recorded by the seismometer. For a P-wave of given energy (i.e., magnitude), the velocity is proportional to $(\rho\alpha)^{-1/2}$ at the station site. Thus, hard rock sites, such as NORSAR, should measure lower amplitudes (hence magnitudes) than sites such as LASA, which is situated on low velocity, sedimentary rock. Using typical values of ρ and α at NORSAR and LASA, we find that LASA amplitudes should be about 1.7 times larger than NORSAR amplitudes. This would cause LASA magnitudes to be at least 0.2 unit larger than NORSAR magnitudes. Such an effect is observed in the limited data shown.

C. Frasier

C. VARIATIONS OF FALSE-ALARM RATES AT NORSAR

The basic detection algorithm is the same at LASA and NORSAR. The steps are: (1) linear predetection filtering to isolate a band with good SNR; (2) full wave rectification; (3) calculation of a short-term average (STA) and long-term average (LTA) by averaging rectified outputs for short (typically 1.5 sec) and long (typically 30 sec) periods of time; and, finally, (4) declare a detection if STA/LTA exceeds a preselected threshold. The process can be applied at sensor, subarray, or array beam levels. It is clear that the detection capability of such a system must decrease if the noise level increases. Also, if the noise level increases with no change of spectrum, the false-alarm rate will be unchanged as long as the detection threshold for STA/LTA is unchanged.

In fact, the false-alarm rate at NORSAR does vary considerably with background noise level, which is seen quite clearly in Figs. IV-7(a) and (b). The LTA is quite stable and representative of noise level at the output of the prerectification filter. The variation in LTA over two time periods with slightly different prerectification filters is shown. Intervals contaminated by obvious events have been removed. Also shown is the number of detections per day, the number of events on the NORSAR bulletin, and the difference of these two. In general, the latter should be a reasonable estimate of false alarms per day, although some real events which were never studied by an analyst might be included. The detection threshold for both time intervals was the same, but note that the false-alarm rate is significantly less for the higher-frequency prerectification filter. Its worst conditions correspond roughly to the best conditions of the lower-frequency filter.

An idealized conceptual model has been formulated to help understand these false-alarm fluctuations and to predict certain trade-offs. First, it is assumed that the output of the prerectification filter has a bandpass spectrum characterized by a bandwidth, center frequency, and mean square noise level. It is also assumed that the short-term fluctuations of STA/LTA are due to those of the STA, and that the LTA can be assumed equal to the average STA value. The calculation of the STA from the rectifier output is conceived of as a simple linear filtering operation. It has been impossible to obtain the probability distribution of the STA, but its stability can be characterized by the ratio of the square of its mean to its variance. For a given threshold, it is reasonable to expect that the false-alarm rate will be a monotone increasing function of this ratio. Thus, by noting the changes in this ratio for different prerectification spectra and postrectification filters, it is possible to predict if false-alarm rates will increase or decrease. Finally, idealized spectra of seismic noise and gain functions of prerectification filters have been used to get the bandwidth and center frequency of the rectifier input under various noise conditions, and to predict combinations of seismic noise level and prerectification filter low-frequency cutoff which will result in equivalent false-alarm rates.

At least for short periods of time, the bandpass input to the rectifier can be thought of as an amplitude-modulated sine wave $A(t) \sin(2\pi f_0 t + \Theta)$, where f_0 is the center frequency, Θ is a random phase, and $A(t)$ is a low-pass process with bandwidth B equal to that of the rectifier input. $A(t)$ is also assumed to be non-negative, so its spectrum contains an impulse at $f = 0$ with area equal to the square of the average value of $A(t)$. Figure IV-8 shows the power spectral density of the rectifier output under these assumptions. The size of the sidebands go as $1/(4n^2 - 1)^2$, where n is the sideband number. The portion between $-f_0$ and $+f_0$ is just the spectrum of $A(t)$ multiplied by $4/\pi^2$. If $B/2 > f_0$, the picture is slightly changed due to pseudo-aliasing since, in fact, the rectified spectrum is an infinite weighted sum of the spectrum of $A(t)$ shifted by $2nf_0$.

The envelope $A(t)$ would be reproduced exactly, within a factor of $2/\pi$, by filtering the rectifier output with a perfect low-pass filter passing frequencies from $-f_0$ to $+f_0$. The mean square value of this, using Parseval's theorem, is $(a^2 + b^2B)4/\pi^2$ and the mean value is a. Thus, the stability as measured by the ratio of the square of the mean to the variance is $r^2 = a^2/b^2B$. But the envelope may be considered to be Rayleigh distributed, for which we have $r^2 = \pi/(4 - \pi)$. Thus, $a^2/b^2 = B\pi/(4 - \pi)$.

The actual filter used to obtain STA from the rectifier is not ideal from $-f_0$ to $+f_0$. It is not even perfect low pass, but assume for the moment that it is and has the passband shown in Fig. IV-8. Taking the product of the rectifier output spectrum and the square of the STA filter,

we again can find the mean square value of STA using Parseval's theorem – it is $[(a^2 + b^2)/T]4/\pi^2$. The stability measure is then $r_1^2 = a^2T/b^2$. Substituting for a^2/b^2 in terms of the bandwidth of the input to the rectifier gives

$$r_1^2 = \frac{\pi}{4 - \pi} BT \qquad \text{(IV-1)}$$

for this ideal case when the postrectification smoothing does not pick up any sideband energy which would reduce the stability. Note that, all other factors being equal, the sideband effect will be less severe for large f_0.

To complete our model, it is necessary to consider the effective bandwidth and center frequency at the rectifier input for typical seismic noise and prerectification filters used in NORSAR. Figure IV-9 shows three power spectral densities for noise at NORSAR. They correspond to noisy, typical, and quiet conditions. No correction has been made for instrument response. If F is the log of frequency and P is the number of decibels down from the most extreme case to some spectral peak, we see that (approximately) $P = -(F + 0.7)100$. On log paper, straight lines from this point to (−1.2, −65) and (1.0, −65) give reasonable approximations to the actual seismic spectrum. The prerectification filters in use are bandpass but, for present purposes, considering the ranges of all relevant variables we characterize them as high-pass filters with rolloff 60 dB per decade and corner frequency f_c. Figure IV-10 shows the idealized output spectra from these filters for different noise conditions.

The center frequency and bandpass of ideal filtered spectra can be obtained by simple geometry. Consider the 10-dB bandwidth and center frequency. In that case,

$$B = f_c C_B(P) \qquad \text{(IV-2)}$$

$$f_0 = f_c C_0(P) \qquad \text{(IV-3)}$$

where

$$C_B(P) = \log^{-1} 10C(P) - \log^{-1} \frac{10C(P)}{1 - 60C(P)} \qquad \text{(IV-4)}$$

$$C_0(P) = \left[\log^{-1} 10C(P) + \log^{-1} \frac{10C(P)}{1 - 60C(P)}\right]/2 \qquad \text{(IV-5)}$$

and

$$C(P) = \frac{(P + 170)}{(100P + 6500)} \quad . \qquad \text{(IV-6)}$$

Figure IV-11 is a plot of C_B and C_0 vs P. They are roughly the same shape, and $C_B = 1.32C_0$ is a least-square fit of XC_0 to C_B using samples of P at 0, −10, −20, and −30.

The false-alarm rate is determined by B and f_0 and is independent of the absolute power level. However, if $f_0 = f_c C_0(P)$ is constant on a line in the f_c, P plane, then so is B since $C_B = 1.32C_0$. Figure IV-12 is a contour plot of f_0. For example note that, if $f_c = 1.2$ and $P = -5$, we should have the same false-alarm rate as $f_c = 0.9$, $P = -30$. That is, the false-alarm rate under best noise conditions with a 0.9-Hz corner should be the same as for worst noise conditions and a 1.2-Hz filter. This seems to be corroborated by the data in Fig. IV-7. Also note that large f_0 implies smaller false-alarm rate since sideband leakage will be reduced and [see Eq. (IV-1)] bandwidth will be increased.

Suppose we consider $f_c = 1.2, 1.6$. Then the effective prerectification bandwidths, assuming $P = -20$, are 2.03 and 2.69 Hz according to Eqs. (IV-2), (IV-4), and (IV-6). The latter may be a few tenths high due to the high-frequency cutoff of the actual filter used, but that will be ignored. Now, with $T = 1.5$, Eq. (IV-1) gives $r_1^2 = 11.1$ and $r_1^2 = 14.7$ for the two filters, respectively. Observed values on a beam during a relatively quiet period on day 76 of 1972 were 10.7 and 14.7. Such good agreement is of course chance, since so many approximations have been made; but the point is that the idealized model, which does not consider sidebands, does predict the correct order for stability.

As mentioned earlier, it has not been possible to determine theoretically the probability distribution of STA values. Experimentally it is observed to be quite skew and clearly not Gaussian, and it also is clearly not Rayleigh. It can be quite well fit by a lognormal distribution. That is, ln(STA) is approximately normal with nonzero mean μ and standard deviation σ. Values of $\mu = 4.67$ and $\sigma = 0.3$ were estimated from STA values of a coherent beam at NORSAR. The sample distribution of the normalized variable

$$y = \frac{\ln(\mathrm{STA}) - \mu}{\sigma} \tag{IV-7}$$

is shown in Fig. IV-13. Also shown are a few selected points on the Gaussian distribution to indicate the good agreement.

If STA is lognormal, it is now simple to estimate expected numbers of false alarms per day on each beam. Suppose L is the decision threshold in decibels. That is, a detection is declared if twenty times the base ten log of the ratio of STA to its long-term average is greater than L. Let μ_s be the long-term average of STA. Then, a detection is declared if

$$y \geq \frac{0.1151\,L + \ln \mu_s - \mu}{\sigma} \triangleq \alpha \tag{IV-8}$$

where y is Gaussian with zero mean and unit standard deviation. Since α will be large, we can use the approximation

$$\Pr\{y \geq \alpha\} \approx \frac{1}{2} - \frac{1}{2}\sqrt{1 - \exp[-2\alpha^2/\pi]} \approx \frac{1}{4}\exp[-2\alpha^2/\pi] \quad . \tag{IV-9}$$

Using $L = 10.5$, μ and σ given above, and $\mu_s = 111.6$, estimated from data, we obtain the probability of false alarm for an observation as 1.1×10^{-5}. It has been verified from the sampled correlation function of STA values, which are calculated every 0.5 sec at NORSAR, that only every third value is approximately independent. Thus, there are about 0.57×10^5 independent STA observations on each beam every day and the expected number of false alarms per day, per beam is 0.65. This is, of course, for noise conditions on the particular day (day 76) 1972.

In fact, on day 76 we estimated 42 false alarms (see Fig. IV-7). There are about 300 beams used, and with 0.65 false alarm per beam this would be 185 false alarms if false alarms were independent on all beams. It would appear that we must assume only 65 independent beams to obtain agreement with observations for false alarms. A check of STAs during detections on day 76 should indicate how many beams, on average, exceeded the threshold for each false alarm, but it has not been possible to check this.

Assistance of many individuals at NORSAR and use of NORSAR facilities for this research is gratefully acknowledged.

R. T. Lacoss

D. COMPARISON OF SHORT-PERIOD MICROSEISMIC NOISE AT LASA AND NORSAR

We have found that the P-wave signals at NORSAR tend to have much of their energy concentrated in the relatively high-frequency range of 1.5 to 2.5 Hz. This situation is quite different from that at LASA where the P-wave signal energy is concentrated primarily in the 0.6- to 1.5-Hz range. The relatively high-frequency content, and thus shorter wavelengths, of the P-wave signal at NORSAR has led to some difficulties due to loss of signal coherence. In order to achieve the same short-period detection threshold level at NORSAR as at LASA, it might be possible to filter the NORSAR signals so that their dominant energy is in the 0.6- to 1.5-Hz range. To do this, it is necessary to know both about the signal and noise levels in this band for both LASA and NORSAR. The noise problem was considered first and the results of the analysis will not be presented.

The frequency-wavenumber spectra, as well as power spectra and coherence, were measured for the short-period microseismic noise, in the 0.1- to 5-Hz range, at the Over subarray at NORSAR, as well as at LASA. The Over subarray consists of 12 short-period vertical seismometers located within an aperture of about 18 km. The high-resolution method[3] was used in the measurement with a block length of 25 sec, leading to a frequency resolution of 0.04 Hz, and with 36 blocks which yields 90 percent confidence limits of about ±1.4 dB. In addition, the coherence measurement level for uncorrelated noise is about 0.2, using the coherence (as well as power spectra) estimation procedures described previously.[4]

Some typical power spectra for the noise at LASA and NORSAR are shown in Figs. IV-14(a) and (b), respectively. The result for NORSAR shown in Fig. IV-14(b) is typical of six measurements which were made every other month during a 1-year period. The frequency-wavenumber spectrum for the noise sample given in Fig. IV-14(b) was presented previously.[5] It was found that at 0.2 and 0.4 Hz the noise consisted primarily of surface waves propagating from the northeast direction, with a phase velocity of about 3.5 km/sec. The measurements at other frequencies in the 0.2- to 1.0-Hz band indicated that there were large amounts of nonpropagating noise, relative to the amount of propagating noise. The coherence of this short-period noise sample vs frequency is shown in Figs. IV-15(a) and (b) for spatial lags of about 1 and 3 km, respectively. The coherence data in Fig. IV-15(a) show that the 1- to 2-sec microseisms consist of a nonpropagating as well as a propagating component. This propagating component of the noise has a frequency-wavenumber spectrum whose structure has been found to be highly diffuse in wavenumber space, as indicated by the coherence data in Fig. IV-15(b). These results at NORSAR are also typical of those found at LASA for short-period noise.

The data in Fig. IV-15(a) show that the coherence, for a spatial lag of 1 km, increases from 1.5 to 4.0 Hz. In addition, the results of Fig. IV-15(b) also indicate that the coherence, for a spatial lag of 3 km, increases in this frequency range, but not to as large a value as that for 1 km. These data indicate that there is propagating noise in this frequency range and that the relative amount of such noise increases as the frequency increases. In addition, the data show that this moderate coherence at high frequencies is definitely due to ground motion and not to other effects such as system noise.

The power spectra in Figs. IV-14(a) and (b) show that the noise levels at LASA and NORSAR, at 1 Hz, are approximately 1 and 8 dB relative to 1 $m\mu^2$/Hz at 1 Hz, respectively. This implies that there is more noise energy at NORSAR at 1 Hz than at LASA. A probable cause for this is the closer proximity of NORSAR to a coastline than LASA. There is thus a loss of about 7 dB, relative to LASA, that would be incurred if the low-frequency signal components at NORSAR were to be used for the purposes of P-wave signal detection even if the signal spectra were identical.

However, the signal spectra at NORSAR often increase with frequency up to 1.5 Hz. In addition, it is shown by Frasier in Sec. IV-B that NORSAR signal magnitudes from Eurasia are smaller than those at LASA by an average of approximately 10 dB. It is thus clearly undesirable, both from signal and noise considerations, to use a band centered on 1 Hz for Eurasian events.

J. Capon

REFERENCES

1. "Amplitude Anomalies at LASA," Report No. LL-4, prepared for Lincoln Laboratory by Earth Sciences, A Teledyne Company (9 January 1967).
2. R.T. Lacoss, "A Large-Population LASA Discrimination Experiment," Technical Note 1969-24, Lincoln Laboratory, M.I.T. (8 April 1969), DDC AD-687478.
3. J. Capon, "High-Resolution Frequency-Wavenumber Spectrum Analysis," Proc. IEEE 57, 1408-1418 (1969), DDC AD-696880.
4. _____, "Investigation of Long-Period Noise at the Large Aperture Seismic Array," J. Geophys. Res. 74, 3182-3194 (1969).
5. Seismic Discrimination SATS, Lincoln Laboratory, M.I.T. (30 June 1970), p. 29, DDC AD-710613.

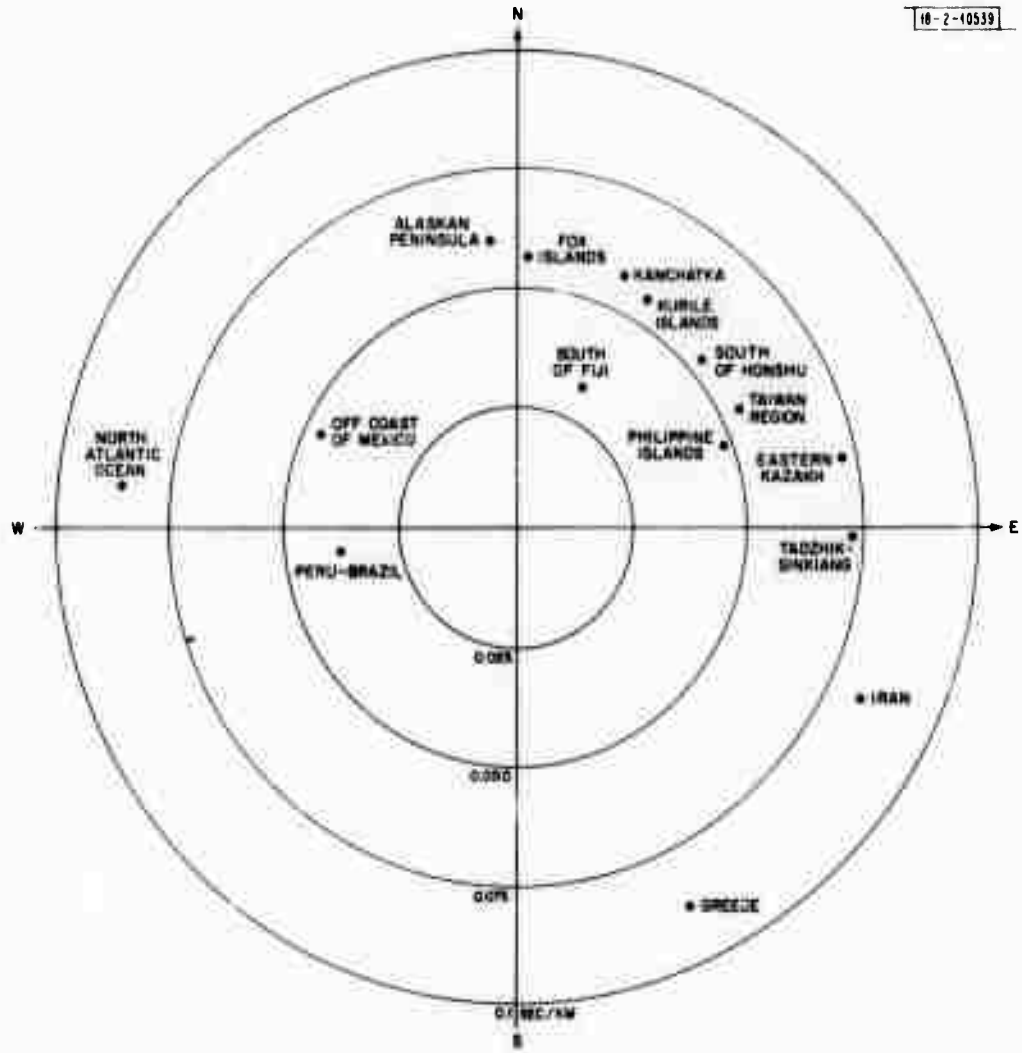

Fig. IV-1. Location in inverse velocity, relative to NORSAR, of 16 regions used in short-period amplitude study.

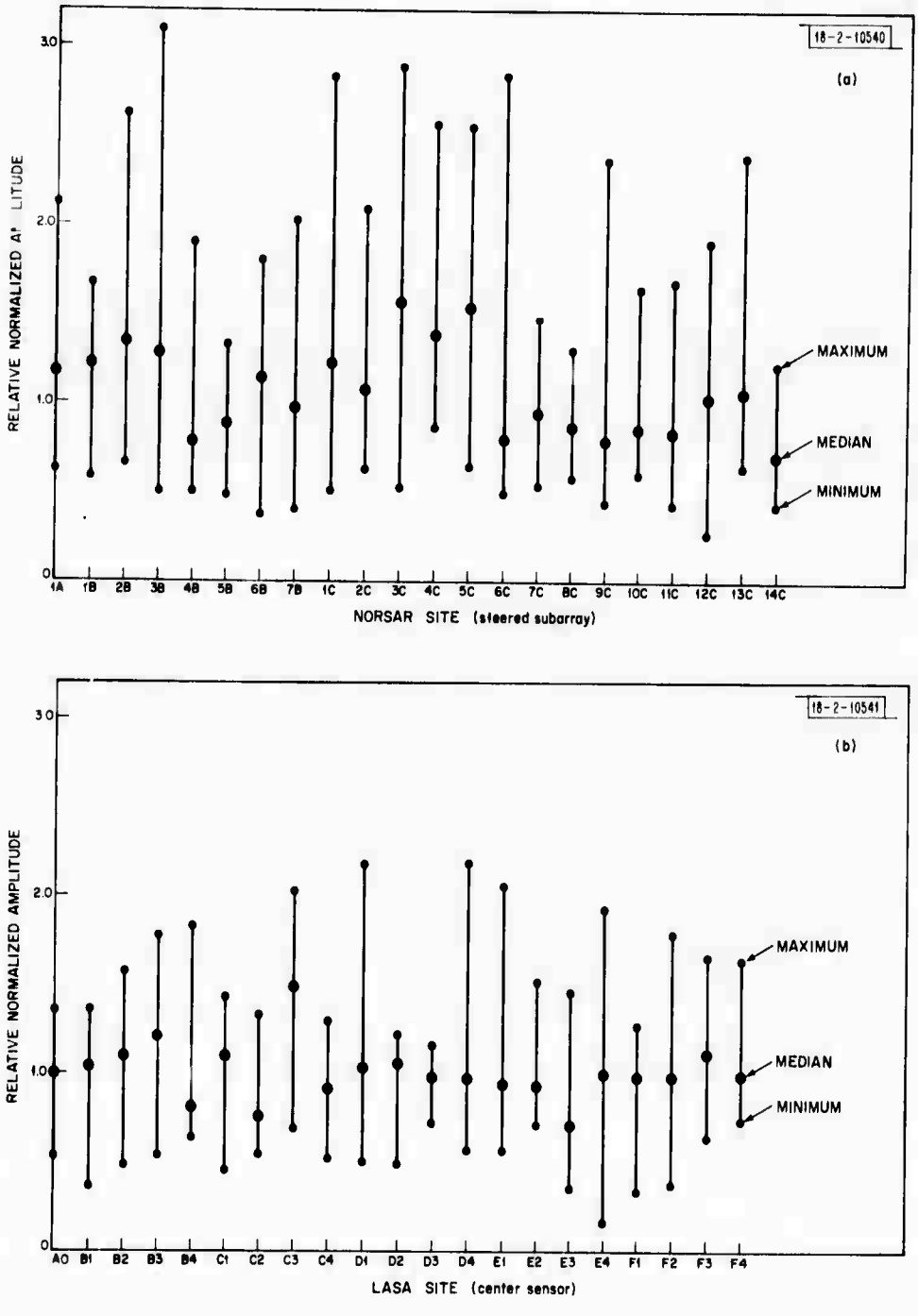

Fig. IV-2. Minimum, maximum, and median subarray relative amplitudes for (a) 16 regions measured at NORSAR, and (b) 13 of same regions measured at LASA.

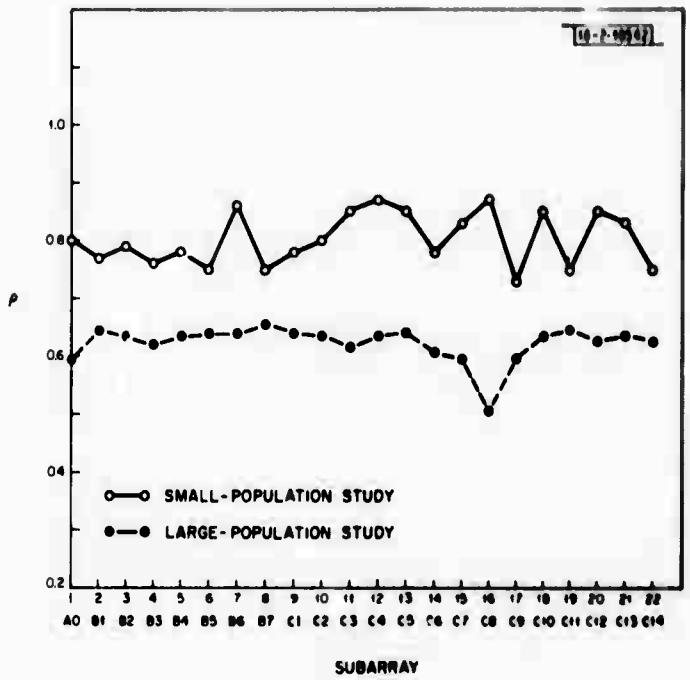

Fig. IV-3. Maximum coherencies of subarray beams with respect to full array beam. Solid line – small-population study; dashed line – large-population study.

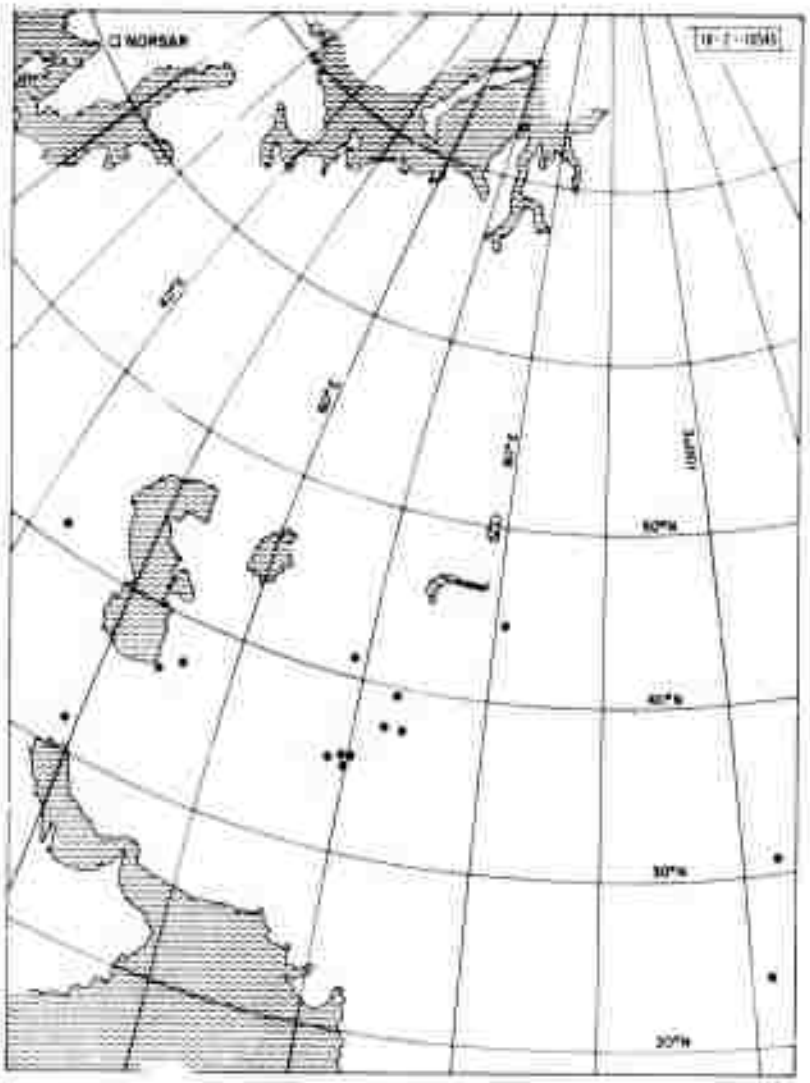

Fig. IV-4. Map showing location of NORSAR and events studied. Open circles are presumed explosions and filled circles are earthquakes.

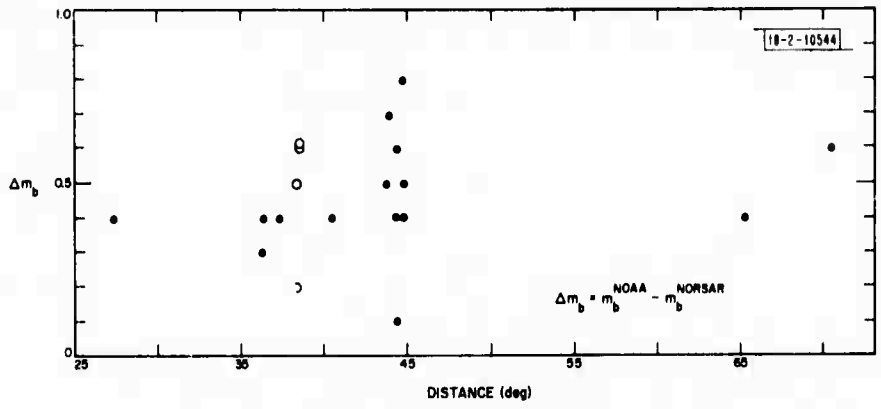

Fig. IV-5. Difference between NOAA and NORSAR m_b, platted vs epicentral distance.

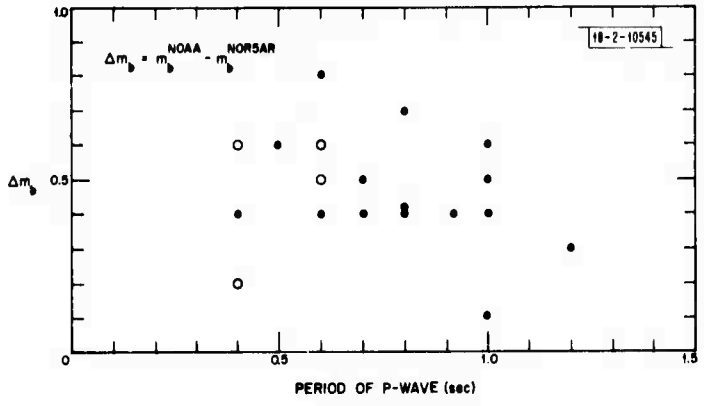

Fig. IV-6. Difference between NOAA and NORSAR m_b, plotted vs period of P-wave.

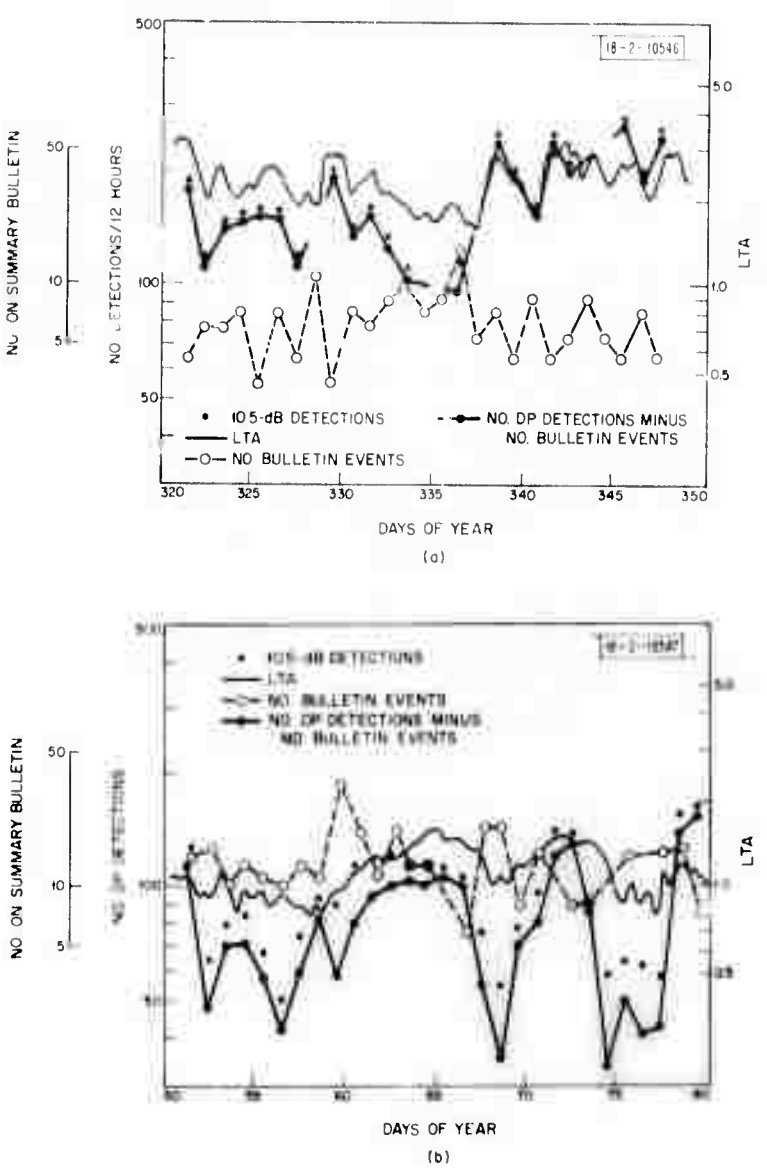

Fig. IV-7. Noise level from full wove rectifier (LTA), number of bulletin events, ond estimoted number of folse olorms ot NORSAR for (o) 17 November to 13 December 1971 with 0.9- to 3.5-Hz detection filter, ond (b) 20 Februory to 19 Morch 1972 with 1.2- to 3.2-Hz detection filter.

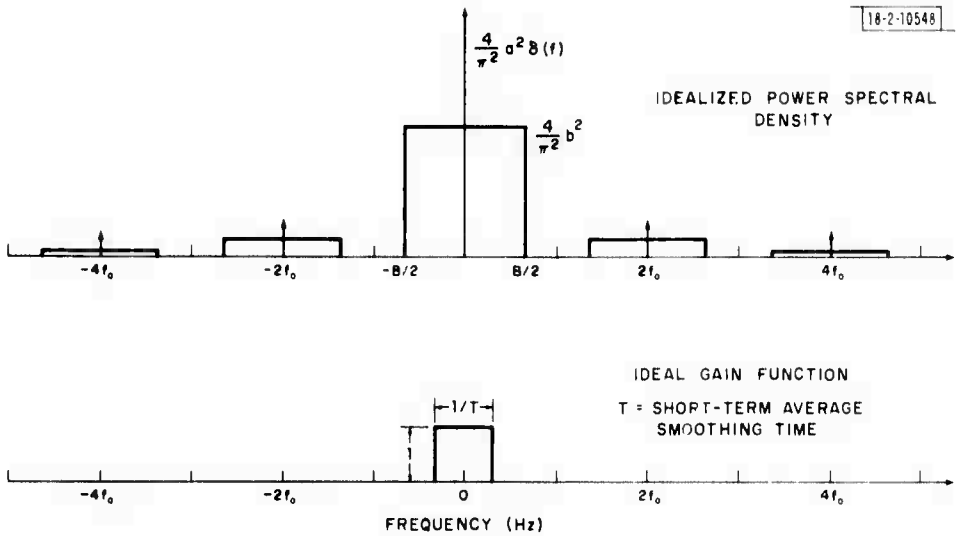

Fig. IV-8. Ideolized power spectrol density of filtered ond rectified band-limited noise, and ideal gain functian of pastrectificotion smoothing filter.

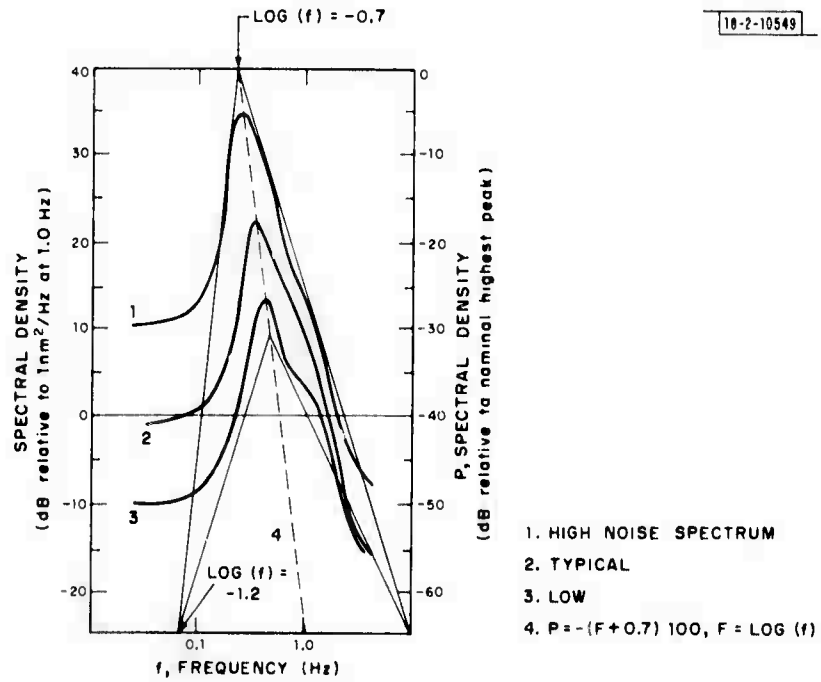

Fig. IV-9. Typical NORSAR short-period noise spectro and straight-line appraximotions to them.

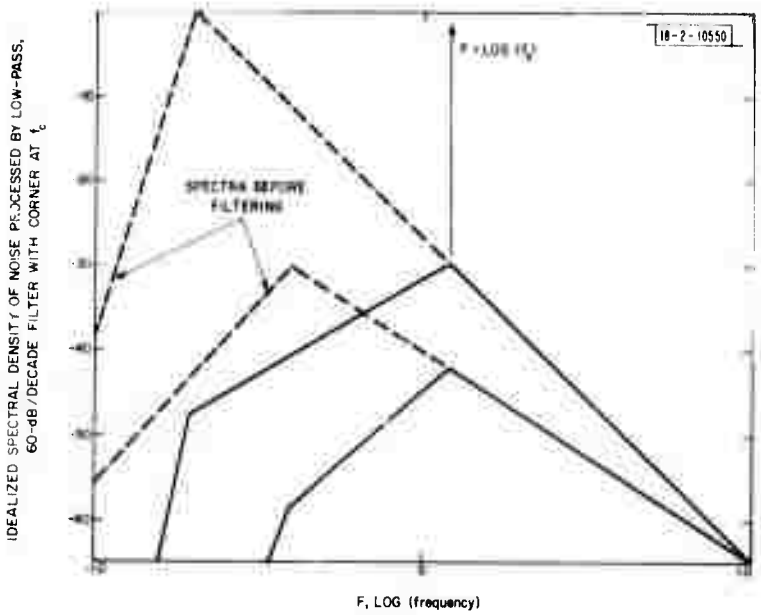

Fig. IV-10. Idealized NORSAR noise spectro before and after filtering with high-pass filter with corner frequency f_c and 60-dB/decade rolloff.

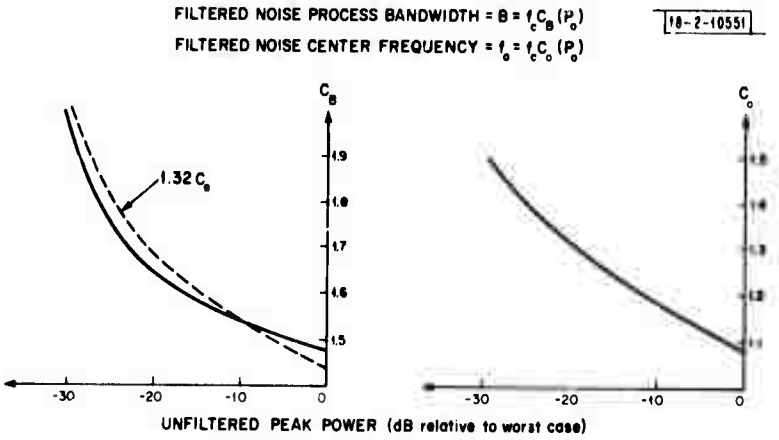

Fig. IV-11. Scale factors between bandwidth of rectifier input C_B times filter corner f_c, and between center frequency of rectifier input C_o times f_c as function of peak unfiltered noise power P_o.

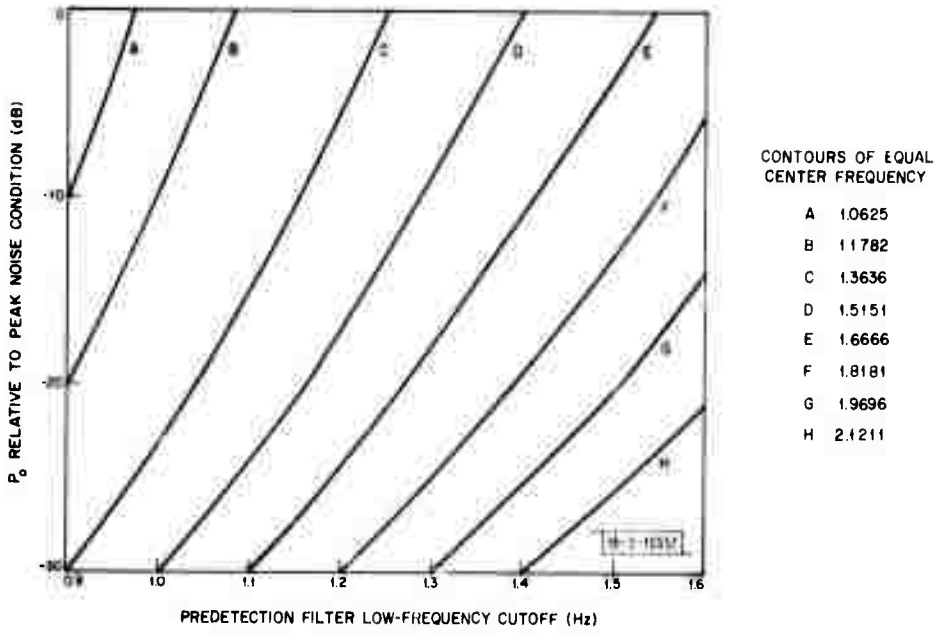

Fig. IV-12. Contour map of rectifier input center frequency as function of unfiltered peak noise power and prefilter low-frequency cutoff.

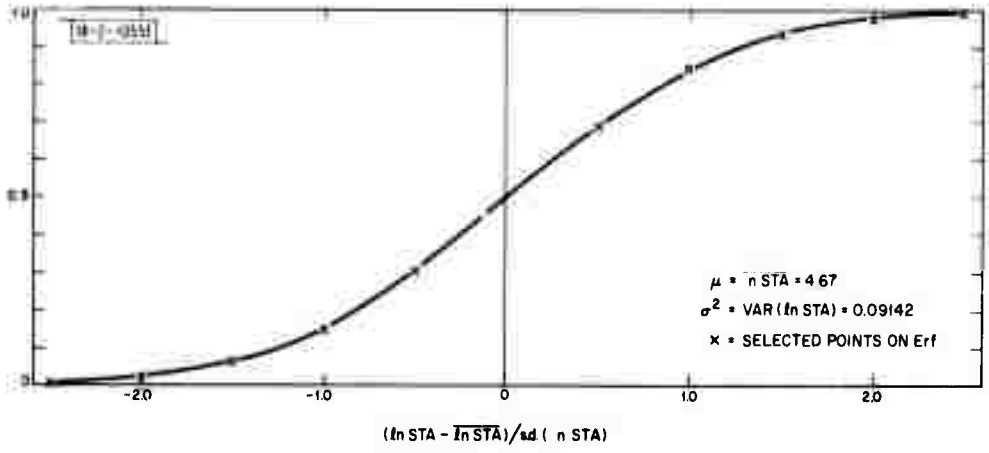

Fig. IV-13. Cumulative distribution of log of short-term average of NORSAR beam.

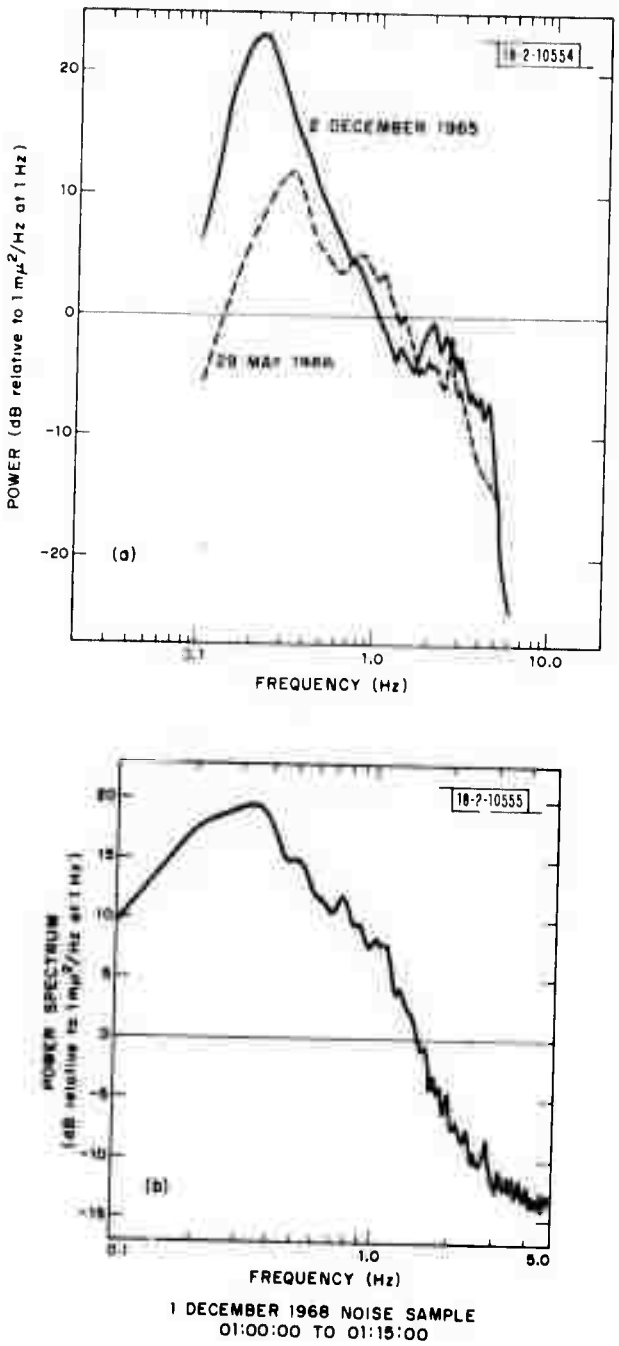

Fig. IV-14. Typical power spectra far short-periad micraseismic naise at (a) LASA and (b) NORSAR.

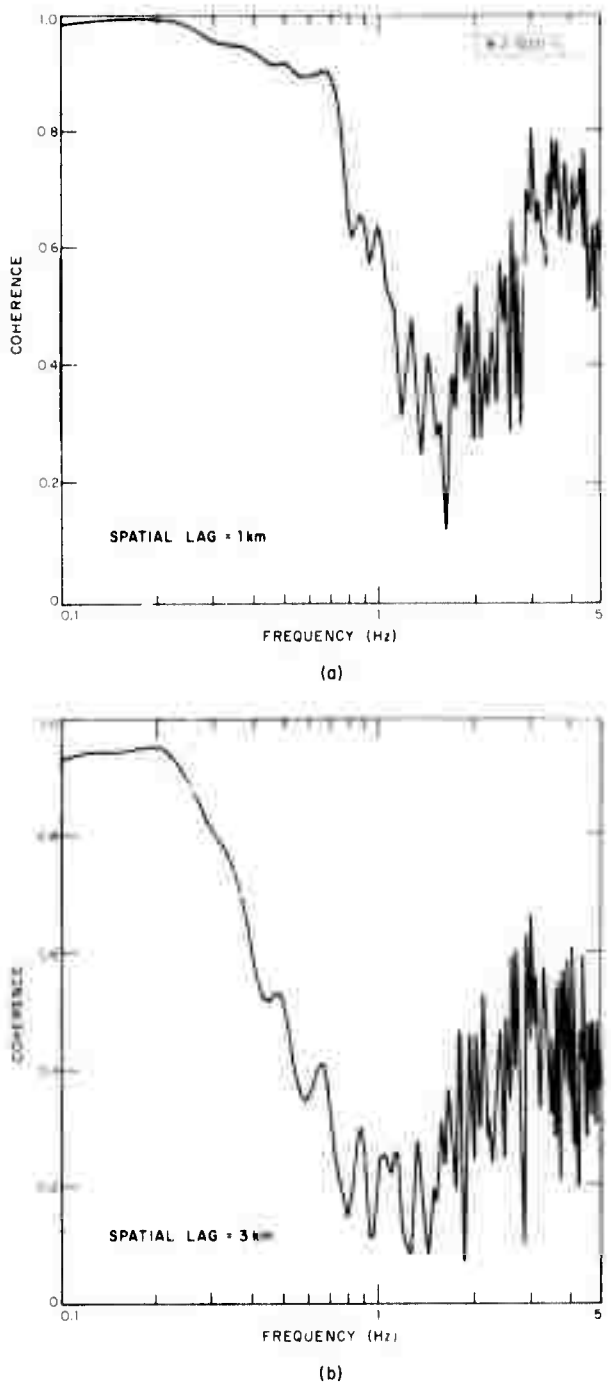

Fig. IV-15(a-b). Caherence vs spatial lag for short-periad microseismic naise at NORSAR.

V. SIGNALS AND NOISE

A. NONPROPAGATING NOISE AND ATMOSPHERIC LOADING

In the last SATS,[1] I investigated the possibility of predicting and removing some of the nonpropagating noise measured at LASA by long-period seismometers using the information provided by a nearby microbarograph. This seemed a reasonable thing to do as there is often a high coherence between the outputs of a microbarograph and a seismometer at the same site at times when the level of nonpropagating noise is high.[2] The process of measuring coherence is a linear one; it would therefore be expected that in the time-domain a transfer function could be computed which could be convolved with the microbarograph output to produce that component of the seismic noise which was coherent. Such a transfer function was computed for a particular noise sample and did, indeed, predict all the coherent noise when convolved with the microbarograph output. When this noise was subtracted from the observed noise, the noise level was substantially reduced. If the predictable component of the noise had been largely due to buoyancy effects in the seismometer, one would have expected the same transfer function convolved with the output from the same microbarograph to have predicted at least some of the noise in the same seismometer on another occasion when the coherence between this microbarograph-seismometer pair was again high. That this did not prove to be the case was taken as evidence that buoyancy effects were negligible and that most of the observed nonpropagating seismic noise was caused by atmospheric deformation of the ground.

Since nonpropagating noise is incoherent over distances greater than a few kilometers and does not correlate from seismometer to seismometer at LASA, and since so much of it can be removed by merely subtracting that component which is correlated with the microbarograph at the same site, it is clearly the result of ground deformation caused by atmospheric pressure changes in the near vicinity of the seismometer. Any far-field atmospheric loading effects must be quite insignificant. In describing the loading process, therefore, we would expect an elastic half-space to be an adequate model for the earth, and, since wind speeds are two or three orders of magnitude less than the speeds of seismic waves, negligible error would be incurred in considering the elastic deformation to be static.

If the surface of the half-space is taken to be the xy-plane and z is positive into the medium, the vertical displacement u_z at the point (0, 0, z) to a pressure load P(x, y) is given by[3]

$$u_z(0, 0, z) = \int_{-\infty}^{\infty} \int_{-\infty}^{\infty} \left(\frac{k_1}{r} + \frac{k_2 z^2}{r^3} \right) P(x, y)\, dxdy \qquad \text{(V-1)}$$

where

$$r = (x^2 + y^2 + z^2)^{1/2}$$

$$k_1 = \frac{1 - \nu^2}{\pi E}$$

$$k_2 = \frac{1 + \nu}{2\pi E}$$

ν = Poisson's ratio

E = Young's modulus

If the expectation of u_z^2 is calculated from Eq. (V-1) assuming P(x, y) to be white and random in two dimensions, we find

$$E[u_z^2] = \int_0^\infty 2\pi \left(\frac{k_1}{r} + \frac{k_2 z^2}{r} \right)^2 E[P^2]\, r\, dr \quad . \tag{V-2}$$

This integral diverges at the upper limit and at the lower limit when z = 0. In other words, we would expect to obtain infinite noise from such a model. Since this is not observed, there is something wrong with the model.

Haubrich[4] considered the same model but with discrete pressure cells, each of the same area and with the same average pressure load. The integral becomes a summation which, again, does not converge. This means, however, that many pressure cells are included; those which are not included always contribute infinitely more to the expected noise. The problem is clear once we go into the wavenumber domain.

If the applied pressure at the surface is

$$\sigma_z = P(\alpha, \beta) \cos(2\pi\alpha x + \varphi_\alpha) \cos(2\pi\beta y + \varphi_\beta) \tag{V-3}$$

then the resulting vertical displacement is[5]

$$u_z = \frac{\sigma_z}{2\mu \cdot 2\pi c} [2(1 - \nu) + 2\pi c z]\, e^{-2\pi c z} \tag{V-4}$$

where $c = (\alpha^2 + \beta^2)^{1/2}$, and μ is the shear modulus. It is clear that whenever c = 0, u_z is infinite. This corresponds to the divergence of the integral (V-2) at the upper limit and is just a function of choosing a half-space as the model. If we had chosen a spherical earth, this would not have happened. Since we are sure that the curvature of the earth is irrelevant to this problem, we can filter out this D.C. effect by multiplying the right-hand side of Eq. (V-4) by $[1 - e^{-\gamma c}]$. The divergence at the lower limit of the integral (V-2) is caused by including infinitely high wavenumbers. This is equivalent to modeling the pressure distribution P(x, y) with an infinite number of point forces which will always produce infinite displacement at the surface. Since point forces are not physical, we can filter out that effect by applying a factor $[e^{-\eta c}]$ to the right-hand side of Eq. (V-4). With these additional factors, the integral (V-2) can be made to converge.

Examination of Eq. (V-4) provides an explanation for the failure of the transfer function, described above, to remain stable from one noise sample to another. At any particular wavenumber, the displacement u_z is proportional to the wavelength 1/c. If we make the first-order assumption that, at a given frequency, the wavelength is proportional to the wind speed, we should be able to find a stable transfer function using the product of the atmospheric pressure and wind speed. Since the instrument responses of the microbarograph and anemometer are entirely different, these will have to be removed before the product of their outputs can be made.

I am currently testing this hypothesis.

A. Ziolkowski

B. RAYLEIGH-WAVE DETECTION CAPABILITIES OF LONG-PERIOD ALPA AND LAMONT SEISMOMETERS

A study of the surface wave detection capabilities of individual long-period seismometers of the ALPA and NORSAR arrays has been initiated. The purpose is to evaluate the detection

capabilities for sensors installed at various sites of the arrays, and to compare them with analog data obtained by the high-gain Lamont seismometers installed at the nearby stations in Fairbanks, Alaska (FBK) and at Kongsberg, Norway (KON). Preliminary results obtained at the ALPA and FBK sites for 31 August 1971 are summarized below. Twenty-four hour coverage of digital data from several sites of the ALPA array and analog film data for the FBK site were available for this day.

Figure V-1(a-b) illustrates the relative frequency responses of the ALPA components and the vertical components of the system at station FBK.[6,7] The relative response of the ALPA components peak at about 27 sec and the relative gains of the Lamont vertical components peak at a gain of 7.7 k at 25 sec for the low-gain (ZLO) component and at a gain of 106 k at 32 sec for the high-gain (ZHI) components. The ZHI response approximates that of Pomeroy, et al.[8]

As a guide to the probable origin of events detected on the ALPA and FBK records, bulletins issued by NOS and SAAC were consulted. Origin times, locations, and body-wave magnitudes are given by both bulletins. The NOS bulletin also reports focal depths. Distances from, and approximate surface wave arrival times at FBK were calculated for all events listed in the bulletins assuming a Rayleigh-wave velocity of 3.5 km/sec. Table V-1 lists arrivals for 12 NOS events, and Table V-2 lists arrivals for 32 SAAC events. Some events appear on both tables. Examination of the ALPA and FBK records showed indications of at least 11 surface wave arrivals (hereafter referred to as ALPA/FBK events), some of which were clearly discernible on both ZLO and ZHI traces at FBK as well as most channels of ALPA. The set of ALPA/FBK events includes some threshold events which were not detected on either of the FBK records, but for which there was some indication of their presence on one or more channels of the ALPA records; 10 of these 11 LP events could be associated with events on the NOS or SAAC bulletins. Table V-3 summarizes the approximate times of arrival for the ALPA/FBK events estimated from the data and probable identification with events listed in either the NOS or SAAC bulletins. It should be noted that the list of events selected for discussion in this report do not include a number of very marginal detections which a more careful examination of the records might confirm. In the case of ALPA, increased detection probability through beamforming can be expected, and for FBK some improvement might be effected through digital processing.

As an illustration of the relative detection capabilities of the ALPA and FBK systems, Figs. V-2(a) through (f) present a series of traces of data recorded by the two systems for 6 of the ALPA/FBK events. For each event, two traces are shown for the ZLO and ZHI analog FBK film data. The traces from selected vertical channels of the ALPA sites are also shown. It should be noted that these traces comprise short sections of the recording for the entire day and, as such, are not strictly representative of the general appearance of the data when examined over longer time periods. For example, the long-term fluctuations in background noise, particularly for the ZHI/FBK instrument, are not always fairly represented in the examples shown.

In Figs. V-2(a-f), traces from the FBK film records have the same relative magnification for all events. The amplitudes of the ALPA traces vary for different sites, and the gains have been adjusted for convenience in presentation.

A comparison of the detection capabilities of the ALPA and FBK systems on these data can be made by examination of the events shown in Figs. V-2(a-f). A brief discussion of the individual events is presented in the following paragraphs.

TABLE V-1

SURFACE WAVE ARRIVALS AT STATION FBI FOR NOS REPORTED EVENTS
31 AUGUST 1971

NOS Event	Origin Time	Arrival Time	Distance (deg)	Depth (km)	m_b	Latitude (deg)	Langitude (deg)	Region
1	00:06:15	00:49:29	81.7	60	4.5	4.87S	153.29E	New Ireland Region
2	01:52:17	02:31:40	74.4	87	4.3	36.52N	70.81E	Hindu Kush Region
3	06:03:24	06:30:14	50.7	62	4.1	35.64N	140.15E	Near East Coast of Honshu
4	07:39:37	08:07:02	51.8	83	4.0	34.29N	140.32E	Near East Coast of Honshu
5	10:21:49	11:18:44	107.6	198	4.5	23.71S	66.79W	Jujuy Province, Argentina
6	12:25:15	13:19:23	102.3	69	4.5	19.28S	69.98W	Near Coast of Northern Chile
7	16:02:09	16:35:22	62.8	33	4.6	42.48N	29.35W	Azores Islands Region
8	19:05:53	20:05:10	112.0	43	5.2	30.77S	71.42W	Near Coast of Central Chile
9	20:27:41	20:56:55	55.3	259	4.5	31.13N	138.65E	South of Honshu, Japan
10	21:13:23	21:59:47	87.7	33	4.6	20.82S	173.78W	Tonga Islands
11	22:57:25	23:27:36	57.0	75	5.0	17.30N	100.78W	Guerrera, Mexico
12	23:47:41	24:31:07	82.1	59	4.7	5.07S	152.74E	New Britain

TABLE V-2

SURFACE WAVE ARRIVALS AT STATION FBK FOR SAAC REPORTED EVENTS
31 AUGUST 1971

SAAC Event	Origin Time	Arrival Time	Distance (deg)	m_b	Latitude (deg)	Langitude (deg)	Region
1	23:44:42	23:59:07	27.3	3.9	50.0N	168.0E	Aleutian Islonds Regian
2	23:53:23	00:29:19	67.9	3.8	7.0N	161.0E	Caraline Islands Region
3	23:54:20	00:34:46	76.4	3.9	39.0N	33.0E	Turkey
4	01:52:02	02:32:17	76.1	4.0	35.0N	70.0E	Afghanistan
5	02:01:20	02:23:46	42.4	3.6	40.0N	151.0E	Narth Pacific Oceon
6	04:05:39	05:01:27	105.5	3.9	21.0S	66.0W	Sauthern Bolivia
7	05:46:16	06:20:01	63.8	3.7	39.0N	36.0W	Narth Atlontic Ocean
8	07:01:04	07:32:40	59.7	3.5	49.0N	19.0W	North Atlantic Ocean
9	07:05:02	07:32:52	52.6	3.8	53.0N	32.0W	Narth Atlantic Ocean
10	07:15:44	08:00:42	85.0	4.0	5.0N	81.0W	Neor Coast of Narthern Peru
11	07:39:30	08:06:40	51.3	4.1	35.0N	140.0E	Near East Coost af Honshu, Jopan
12	07:42:49	08:14:20	59.6	4.1	26.0N	139.0E	Volcana Islands Regian
13	07:53:10	08:18:05	47.1	3.7	57.0N	39.0W	North Atlantic Oceon
14	08:19:42	09:12:45	100.3	4.4	17.0S	70.0W	Peru-Bolivio Border Regian
15	10:21:22	11:19:05	109.1	5.1	25.0S	66.0W	Salta Pravince, Argentina
16	12:25:13	13:19:14	102.1	4.8	19.0S	70.0W	Northern Chile
17	13:34:26	14:39:11	122.4	4.1	41.0S	68.0W	Argentino
18	14:06:50	14:47:04	76.0	3.7	8.0N	74.0W	Northern Columbia
19	14:57:23	15:16:46	36.6	3.6	45.0N	155.0E	Kurile Islonds Region
20	15:06:05	15:25:04	35.9	3.5	46.0N	155.0E	Kurile Islonds Regian
21	15:19:38	15:38:27	35.6	3.2	48.0N	88.0W	Ontario
22	16:02:16	16:35:37	63.0	4.4	42.0N	30.0W	Azores Islonds Regian
23	16:29:50	17:16:44	88.6	4.2	9.0N	42.0W	Central Mid-Atlontic Ridge
24	16:32:50	17:11:27	73.0	3.9	10.0N	77.0W	North af Ponamo
25	18:19:08	19:11:39	99.2	4.7	33.0S	171.0W	South of Kermadec Islands
26	19:05:53	20:05:10	112.0	5.2	31.0S	72.0W	Near Coast af Central Chile
27	20:26:59	20:56:25	55.6	4.7	31.0N	138.0E	South of Honshu, Jopan
28	20:43:46	21:16:18	61.5	3.6	43.0N	32.0W	Azares Islands Region
29	21:13:35	21:58:23	84.7	4.6	18.0S	172.0W	Tango Islands Region
30	21:38:45	22:02:35	45.0	3.5	42.0N	141.0E	Hokkaido, Japan Regian
31	22:57:16	23:27:45	57.6	4.8	17.0N	100.0W	Guerrera, Mexico
32	23:44:47	24:00:49	30.3	3.7	54.0N	154.0E	Seo of Okhatsk

TABLE V-3
EVENT IDENTIFICATION FOR SURFACE WAVE DETECTIONS AT ALPA AND FBK
31 AUGUST 1971

ALPA/FBK Events	Arrivol Time (hours)	Identifications and Locations	
1	0043	NOS/1 – New Irelond	No I.D.
2	0235	NOS/2 – Hindu Kush Region	SAAC/4 – Afghanistan
3	0621	No I.D.	SAAC/7 – North Atlantic Oceon
4	0818	No I.D.	SAAC/13 – North Atlantic Oceon
5	1114	NOS/5 – Jujuy Province, Argentina	SAAC/15 – Solto Province, Argentina
6	1321	NOS/6 – Near Coast Northern Chile	SAAC/16 – Northern Chile
7	1526	No I.D.	SAAC/20 – Kurile Islands Region
8	1856	No I.D.	No I.D.
9	2009	NOS/8 – Near Coast Centrol Chile	SAAC/26 – Near Coost Central Chile
10	2157	NOS/10 – Tongo Islonds Region	SAAC/29 – Tonga Islands Region
11	2326	NOS/11 – Guerrero, Mexico	SAAC/31 – Guerrero, Mexico

The extended coda of a relatively large magnitude event (m_b = 5.2) from the Chile Rise which arrives at station FBK at 2335 on 30 August obscures several possible arrivals, from relatively close distances, of low magnitude events located by SAAC during the first hour of 31 August. Note SAAC/1 from the Aleutian Islands Region.

Event 1 [Fig. V-2(a)] appears as a pronounced increase in amplitude at about 0014 hours [about a factor of 2 for ZLO, and a factor of 4 for ZHI in the FBK records (a factor of 4 for the ALPA records)]. There is also an increase in the dominant period from about 25 to 35 sec at this time. Event 1 has been identified from the NOS bulletin as the arrival from an m_b 4.5 event at a distance of 81.7°. The SAAC bulletin did not list this event.

Event 2 [Fig. V-2(b)] has been identified from both the NOS and SAAC bulletins as a surface wave from the Hindu Kush/Afghanistan region of a magnitude 4.0 to 4.3 earthquake and has an estimated arrival time of 0232 hours. It is first visible on the FBK records at about 0235 and on the single ALPA record at about 0233. Maximum signal amplitude on either set of records occurs between 0237 and 0238. Large-scale fluctuations in the background, both in amplitude and period (of the order of 1 minute or more), make the ZHI records difficult to interpret for small-amplitude signals.

Event 3 [Fig. V-2(c)] has been identified from the SAAC bulletin as the arrival from a 3.7 magnitude event in the North Atlantic Ocean at a distance of 44°. The event is detectable on both the FBK and ALPA sensors. No identification is supplied by NOS.

Event 4 [Fig. V-2(d)] is also identified from SAAC bulletin as a magnitude 3.7 event from the North Atlantic Ocean at a distance of about 47°. NOS does not list this event. As was the case for Event 3, it is clearly detectable on all sensors. Since both events have been estimated to

have the same magnitude and similar locations, their records should be compared for similar characteristic features.

Event 6 [Fig. V-2(e)] has been identified from NOS and SAAC bulletins as a 4.5 to 4.8 magnitude event from Northern Chile.

Event 10 [Fig. V-2(f)] has been identified as arriving from a 4.6 magnitude earthquake originating in the Tonga Islands Region. Both NOS and SAAC bulletins list this event. The approximate arrival time was computed to be 2200 hours. This event occurred at a normal depth of 33 km.

As a result of this preliminary study of the ALPA and FBK systems, it can be tentatively concluded that the surface wave detection capability of a single ALPA sensor is comparable to that of the present FBK system. However, it should be noted that the date chosen for comparison of the two systems was not ideal in that neither of the systems was necessarily operating at its best. Further study is required before a firm statement can be made.

E. Ashley

REFERENCES

1. Seismic Discrimination SATS, Lincoln Laboratory, M.I.T. (31 December 1971), pp. 55-56, DDC AD-737092.
2. J. Capon, "Investigation of Long-Period Noise at the Large Aperture Seismic Array," J. Geophys. Res. 74, 3182-3194 (1969).
3. L.D. Landau and E.M. Lifshitz, Theory of Elasticity (Pergamon, New York, 1970).
4. R.A. Haubrich, "The origin and characteristics of microseisms at frequencies below 140 cycles 1 hour," Mono de l'UGGI (1970).
5. Y.C. Fung, Foundations of Solid Mechanics (Prentice-Hall, New York, 1965).
6. "High-Gain, Long-Period Seismograph Station Instrumentation," Vols. I and II, Lamont-Doherty Geological Observatory, Columbia University, New York (31 March 1971).
7. "Long Period Array Processing Development," Final Report to Air Force Technical Applications Center (AFTAC), Texas Instruments Incorporated, Dallas, Texas (15 May 1971).
8. P.W. Pomeroy, G. Hade, J. Savino and R. Chandler, "Preliminary Results from High Gain Wide-Band Long-Period Electromagnetic Seismograph Systems," J. Geophys. Res. 74, 3295-3298 (1967).

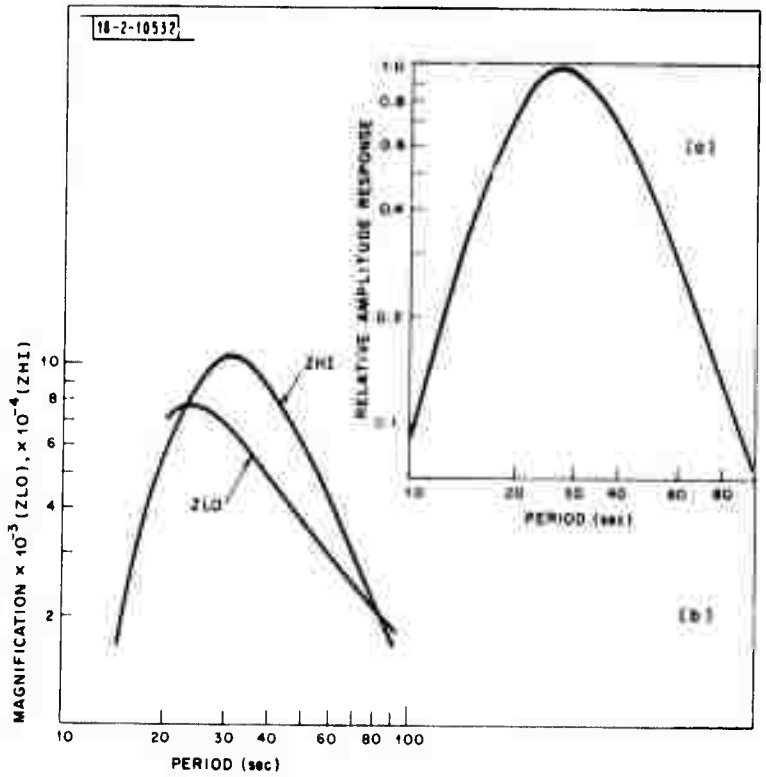

Fig. V-1. Frequency responses of long-period ALPA and FBK seismometers. (a) Relative amplitude response of single component of ALPA system vs period; (b) magnification as function of period of vertical low-gain (ZLO) and high-gain (ZHI) system at station FBK.

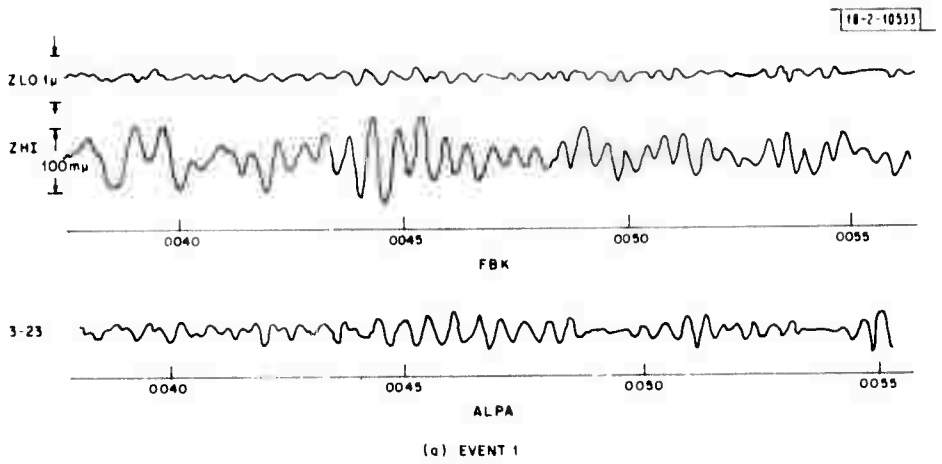

(a) EVENT 1

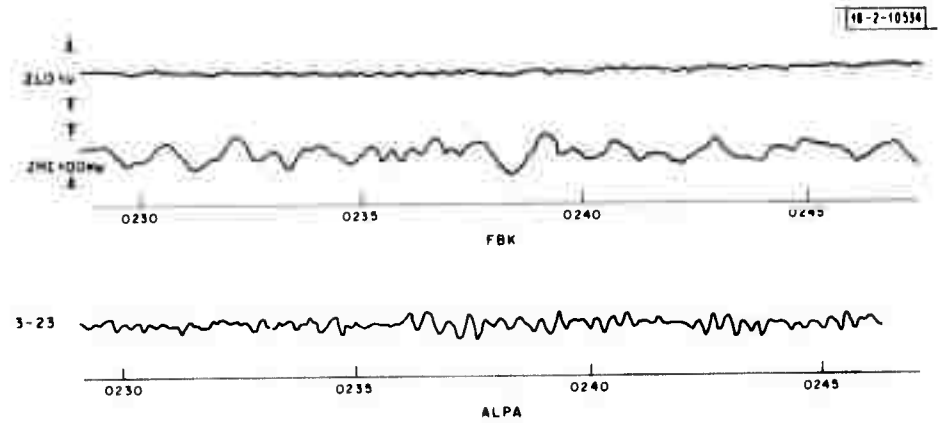

(b) EVENT 2

Fig. V-2(a-f). Long-period vertical motion records for six surface wave events detected at stations FBK and ALPA; in each figure, first two traces are ZLO and ZHI components at FBK. Lower traces are vertical component records for one or more LP ALPA sites.

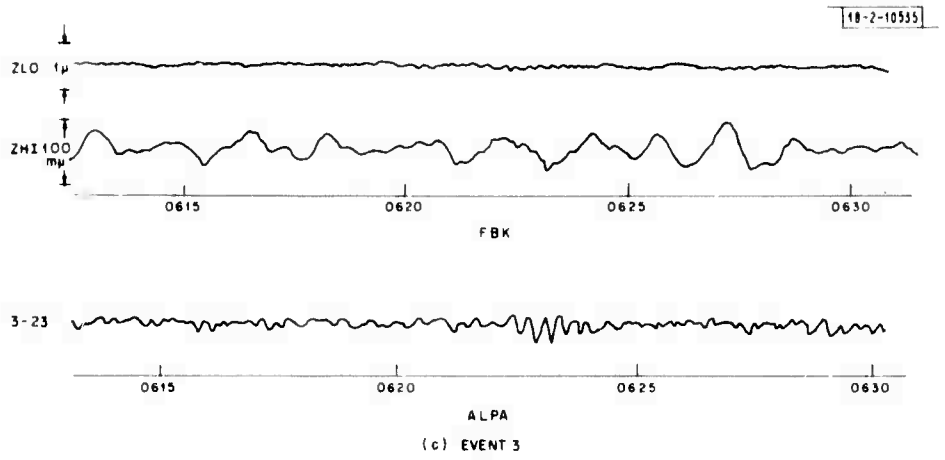

(c) EVENT 3

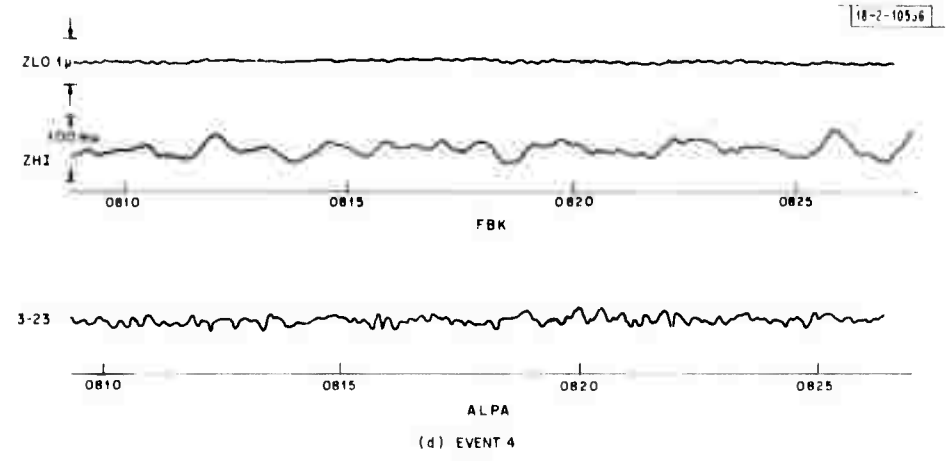

(d) EVENT 4

Fig. V-2(a-f). Continued.

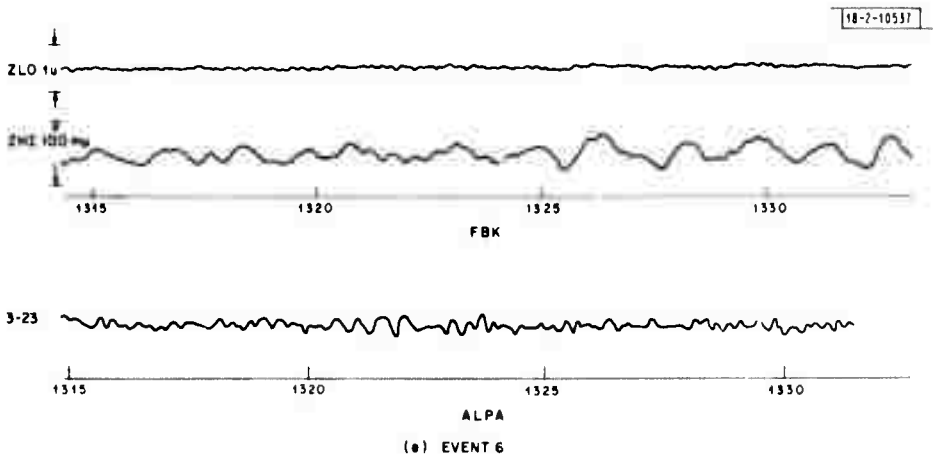

(e) EVENT 6

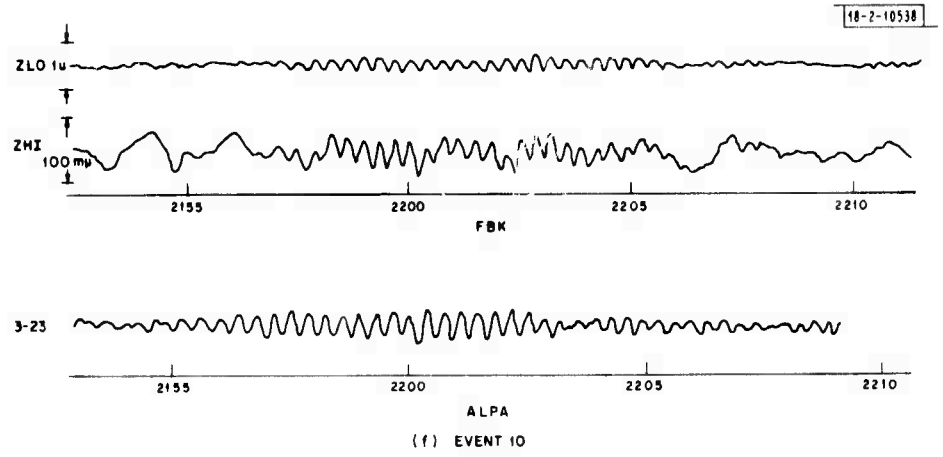

(f) EVENT 10

Fig. V-2(a-f). Continued.

VI. NETWORK CAPABILITY

A. SHORT-PERIOD NETWORK CAPABILITY

A preliminary investigation into producing a small-magnitude-event bulletin has been completed. The aim of the investigation was to produce a seismic events bulletin of low magnitude, $m_b \geq 3.5$, based on available data from NOS, the LASA-SAAC bulletin, and the LASA detection log. The time period from 1 to 9 January 1970 was chosen as the investigation interval since it would be so far removed from the present as not to cause a problem in obtaining NOS or WWSSN film chip data.

In compiling the event list, the epicenters reported by NOS were accepted as locations that needed no verification. However, locations obtained from NOS data that were not published on the PDE listings, due to large residuals or poor locations, were examined and verification of the event was required. Epicenters obtained from the LASA-SAAC bulletin that were not listed by NOS were also considered questionable and therefore in need of verification. The third and largest source of questionable events was the LASA detection log. The process of event verification meant that any questionable event must be seen by at least two of the stations in the selected list of WWSSN stations used for this study (see Table VI-1). Also, the relocation of the event must fall in near proximity to the location given by the bulletin or the detection log.

During this time period, NOS-PDE listings reported 140 events, of which 111 were listed by the LASA detection log. Examination of the NOS unreported events produced 85 verified epicenters, 40 of which were listed on the LASA detection log. Those NOS events not listed in the detection log occurred during LASA down time or were located in the core shadow to LASA. A few NOS events that were not in the detection log were very small and reported only by a few near-regional stations or local networks. The LASA-SAAC bulletin reported a total of 151 events, 66 of which were reported in the PDE listings.

During the 9-day period, the LASA detection log listed 1208 group detections, that is, a group of steered beams detecting a signal within a 10- to 15-sec period. In order to reduce the number of false alarms and noise detections, group detections of less than 5 beams were not evaluated. This left a population of 691 detections that were considered possible events, or phases in need of verification. The NOS data verified 151 of these; the remaining detections were considered to be actual events if the signal could be seen on two or more of the selected WWSSN stations. In this manner, the detection log added 209 events to the event list. The remaining 331 unverified detections were not necessarily false alarms since over 20 percent of them turned out to be phases such as PcP, PP, PKKP, etc. Several other detections were in fact real events and could be seen on stations not in the selected list of stations.

A swarm of events from Yunnan Province, China, occurred during the time period of the investigation. From viewing film chips of station CHG, Chiengmai, Thailand, an additional 34 events were detected based on signal character alone, i.e., separation of Pn, P^*, Pg, and Lg phases, and were added to the events list.

During the 9-day period of the investigation, a total of 475 events were verified, an average of 53 per day. Figure VI-1 shows the relative performance of each station used in the verification of the final event list.

R. E. Needham
R. M. Sheppard

TABLE VI-1

STATIONS USED FOR VERIFICATION PURPOSES IN THE NETWORK CAPABILITY STUDY

WWSSN Stations				
			Gain (in thousands)	
Code	Station	Region	SP	LP
AFI	Afiamalu	Samoa	12.5	0.750
ARE	Arequipa	Peru	50.0	1.500
ATU	Athens University	Greece	12.5	1.500
BUL	Bulawayo	So. Rhodesia	100.0	1.500
CHG	Chiengmai	Thailand	200.0	3.000
COL	College Outpost	Alaska	100.0	1.500
EIL	Eilat	Israel	200.0	3.000
KBL	Kabul	Afghanistan	400.0	6.000
MAT	Matsushiro	Honshu	100.0	3.000
PMG	Port Moresby	New Guinea	50.0	3.000
PRE	Pretoria	South Africa	50.0	1.500
QUE	Quetta	Pakistan	200.0	6.000
SJG	San Juan	Puerto Rico	50.0	0.750
SPA	South Pole	Antarctica	100.0	0.375
TAU	University of Tasmania	Tasmania	25.0	0.750
TRN	Trinidad	West Indies	25.0	1.500
TUC	Tucson	Arizona	200.0	1.500
Stations Other Than WWSSN Stations				
LAO	Lasa Array	Montana		
MBC	Mould Bay	NW Territory	100.0	5.000

B. INTERNATIONAL SEISMIC MONTH

An effort is under way to produce a very comprehensive seismic bulletin for the period of 20 February through 19 March 1972 for the purpose of evaluating some of the large-scale seismic systems that have recently become operational. The cooperation of several other agencies (see below) was enlisted in order to support the International Seismic Month (ISM) effort. Lincoln Laboratory is acting as host for the experiment. The first phase of the ISM effort is to produce as complete a list of epicenters as is possible using the detection logs from both LASA and NORSAR, and arrays at Hagfors, Gauribidanur, Warramunga and Yellowknife. These detection logs, coupled with analyst reports from the single station in the Canadian network and selected WWSSN sites, are providing the basic data for the ISM bulletin. Progress on the bulletin has been promising thus far, and full use has not yet been made of LASA and NORSAR detection logs. Even so, the number of events in the bulletin is well over a thousand. We expect that, upon completion of the bulletin, the total number of events will approach two thousand. At various stages during compilation of the bulletin, listings are being supplied to those cooperating in the study.

The preparation of the bulletin is only one phase of the ISM. Insofar as possible, detailed measurements of long- and short-period data and potential discriminants will be accumulated to form the complete data base. All participants will then have full access to these data to evaluate detection and discrimination capabilities of individual sites, subsystems, and the overall system, which can be conceived of as the current deployed capability. Presumably, some of the sites used (or similar ones) could be incorporated into a system, if that were required. The study should also indicate how current capability is deficient.

The following organizations are participating:

Department of Energy, Mines, and Resources, Canada
Lamont-Doherty Geological Observatory
National Earthquake Information Center, Boulder, Colorado
NORSAR, Norway
Research Institute of National Defense, Sweden
Texas Instruments, Alexandria, Virginia
United Kingdom Atomic Energy Authority, England
SAAC, Alexandria, Virginia
M.I.T. Lincoln Laboratory

R. M. Sheppard
R. E. Needham

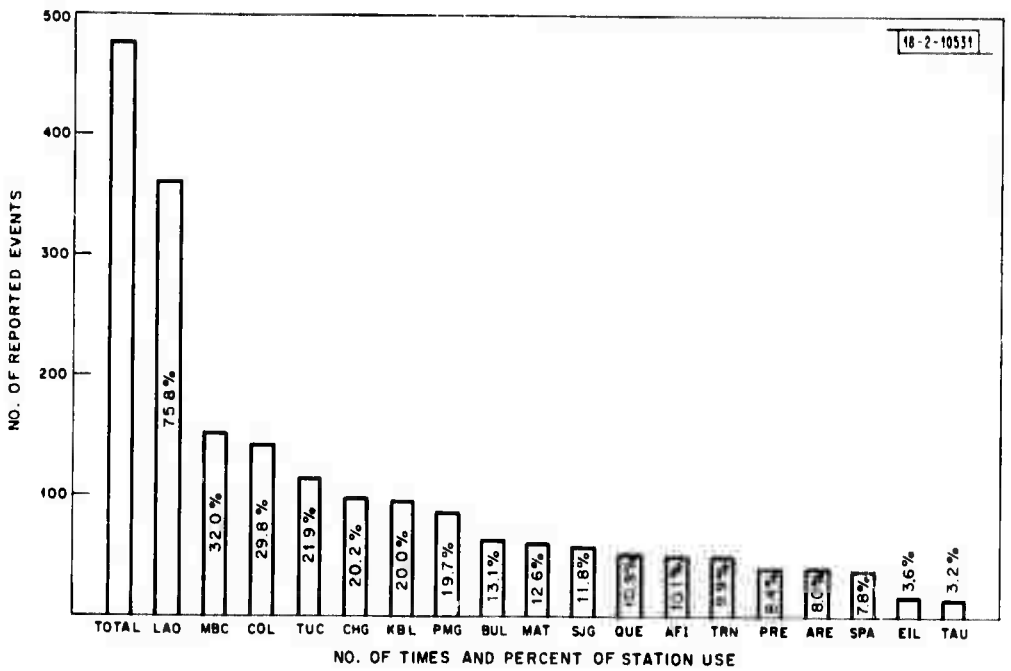

Fig. VI-1. Number of events reported by individual stations in network study.